Laser Phase noise in Rydberg Atom Arrays

Tomas Kozlej

A thesis submitted for the degree of
Doctor of Philosophy

Department of Physics
UNIVERSITY OF STRATHCLYDE

February 2026

This thesis is the result of the author's original research. It has been composed by the author and has not been previously submitted for examination which has led to the award of a degree.

Abstract

Laser noise is an unavoidable feature of modern quantum technologies, with lasers serving as a primary tool for manipulating and controlling quantum matter. Across all quantum architectures, fluctuations in the phase or amplitude of a laser drive can degrade performance: in digital platforms, they cause faulty quantum gates and qubit rotations, while in analogue platforms they disrupt coherent many-body dynamics. In this work, we use stochastic sampling to simulate laser phase noise based on experimentally relevant frequency power spectra. The main focus of the thesis will center around applying this realistic phase noise to simulations of analogue neutral-atom platforms based on Rydberg excitation. Despite such dephasing being a dominant source of decoherence in these systems, its effects in strongly interacting many-body regimes remain less well understood than in the single-qubit or few-qubit setting. In this context, we present a detailed theoretical study on the effects of experimentally realistic laser phase noise on adiabatic state preparation in a one-dimensional Rydberg spin chain.

The core results are presented in two parts. First, we investigate the impact of phase noise on the fidelity of adiabatically preparing an antiferromagnetic ground state in the transverse-field Ising model (TFIM) with long-range Rydberg interactions. Using exact diagonalization and matrix product state (MPS) simulations, we reveal a competition between diabatic and dephasing excitations, leading to an optimal ramp time that balances these effects. In addition, we find that both these excitations to respect reflection symmetry, which confines dynamics to a reduced sector of the Hilbert space. Furthermore, by analyzing matrix elements between instantaneous eigenstates and performing phase noise evolution under time-independent Hamiltonians from different stages of the adiabatic protocol, we show that susceptibility to phase noise is strongly influenced by the system's integrability. Second, we examine whether the states produced by noisy adiabatic preparation exhibit signatures of thermalization. Using the eigenstate thermalization hypothesis (ETH) as a framework, we compare long-time averages of observables to thermal predictions calculated using the Boltzmann distribution at the same energy. We choose to study system relevant observables in the interaction energy and long-range spin correlation; when phase noise is the dominant form of excitation we find that in the long-range TFIM both observables approach thermal values, whereas in a system with only nearest-neighbor interactions, deviations emerge in the case of interaction energy. We also test thermalization in the spin correlation observable as a function of system size, where we see consistent thermalization for small system sizes, but also observe a break down of this effect for the largest system sizes. Our analysis of these results highlights how interaction range, integrability breaking, and system size affect thermalization in noisy adiabatic quantum protocols.

Overall, we provide tools to study laser phase noise in spin systems, and a quantitative understanding of how such noise affects the performance of adiabatic protocols in Rydberg arrays, as well as the mechanisms behind dephasing excitation. The tools and insights developed here are broadly applicable to diagnosing and mitigating noise effects in current and near-term neutral-atom experiments, and can be readily adapted to study both phase and amplitude noise from any experimental laser. As such this work contributes to the theoretical foundation for robust analogue quantum simulation.

Acknowledgements

When I started this PhD I did not know if I was capable of finishing it. I recall the fear and uncertainty of a man looking up at a mountain, not trusting his own harness. Now, with the snow-capped peak in sight, I would like to take a few words to meditate on the people who helped me up along the way.

First of all, I would like to thank my supervisor, Andrew Daley, for taking the chance on me without hesitation and for his mentorship throughout the PhD. Thank you for your patience and the knowledge you shared so willingly, for challenging and motivating me when I needed to grow, and for giving me the support and time when I needed to heal. I will forever value being a part of QOQMS, and to have been given a platform to develop not only as a researcher, but also as a person. I also want to thank my second supervisor, Jonathan Pritchard, who has always been kind, but thorough when engaging with my work. Thank you for your valuable insight in discussions, and for dedicating your time and effort whenever I needed it most. I would also like to extend my gratitude to the team of postdocs who supported me throughout my time at Strathclyde. I begin by thanking Stuart Flannigan and Callum Duncan, who were my first point of contact in my initial years as a doctoral student and not only taught me the ropes, but also gave me the much needed self-belief that I could climb. I would like to thank Johannes Kombe, whose door and mind were always open when I needed help with my work, who showed me what it means to be an excellent researcher, and whom I consider a great friend. In the same breath I would also like to thank Natalie Pearson, on a professional level because her sharp questioning and discussion led to a great deal of progress and self-reflection in my work, and on a personal level because the office never quite popped the same without her. I would also like to mention Pablo Poggi, whom, despite only arriving late into my PhD, I thank for showing enthusiasm and interest in my work that made it a joy to discuss even after all those years. Lastly and mostly I would like to thank Gerard Pelegrí, who was a constant point of reference throughout my PhD, and whose input and guidance can be traced on almost every page of this thesis. Thank you for your immense patience with me, and the time and effort you put into supporting my work, thank you also for the sense companionship I needed to do my best Physics, and finally thank you for the delicious but conspicuously named Polish biscuit operation that you are most certainly running behind the scenes. Lastly, I would also like to thank the University of Strathclyde and in particular the department of physics for facilitating my doctoral program, and for giving me a great platform to succeed as a young researcher.

Next I would like to thank my fellow climbers, the PhD students that I shared my journey with. They say there is no such thing as an original story, and so (given I'm one of the last left climbing) I find myself reading all your Acknowledgments sections in search for inspiration. One thing I did spot (the functioning narcissist that I am) is my name appear time and time again! So, before I begin my cascade of 'thank yous', I wanted to express the sense of value, pride and fulfillment I have in the knowledge that over these five years I have touched your lives as you have touched mine. With that sap out of the way I would like to begin by thanking Ieva Cepaite and Bruno Gavranovic, for the endless hours spent on music, science, philosophy, emotions and everything else we will need to categorize when we meet again. I would also like to thank Kathryn McInroy, Ryan Connor, Simon Kothe, and Grant Henderson for being a constant fixture of office life, always open for a chat about physics or whatever else would break up the daily slog. Next I would like to thank Lorenzo Carfora and Alessandro Civolani, for taking advice from the ramblings of this old PhD sage that may have had a few screws loose. Continuing on I would also like to say a deep thank you to Ewen Laurence, who has become a dear friend over the course of my time at Strathclyde. I appreciate you for the empathy you showed me, and the openness I felt when we discussed anything from the most technical of physics problems to the most personal parts of life. Likewise, I would like to thank Sridevi Kuriyattil, who endured sitting next to me across all those years. I thank you for bringing joy, comradery, and excellent physics discussion to my daily routine, not to mention playing a large part in the unexpected Keralification of my life. Finally, I would like to thank Sebastian Schmidt, whose friendship and fearless imagination were a vehicle for exploring every oddity that makes thoughts worth thinking. Thank you for your selflessness and effort you showed when engaging with all my projects, be it thought, physics, or fantasy, I can only hope there's still many more chapters for us to write such that I can one day give you the same. The time spent climbing together embellished all that was good about my life in Scotland while providing much needed refuge from all that was bad, and I thank you all.

My final thank you goes out to my home base. To my mother Monika and my father Jozef, whose love and pride for me lives in everything I do (despite not

always being able to explain exactly what it is I have been doing here). You have given me nothing but unbridled support and empowerment to go and build my own path, and my gratitude for this freedom can hardly be summed up in a few sentences. Truly, thank you. I also want to extend a short but warm thank you to all the Lars Boys, whose continuing support fuels my drive to achieve great things. Finally I would like to thank my partner Arundhathi who has made the final three years of my PhD unforgettable. Thank you for being with me through thick and thin, for the loving support system I feel whenever I needed it, and the color you bring into my life.

Oh, almost forgot! I would also like to thank myself. Thanks Tomas, you did good.

Contents

Chapter 1

Introduction

1.1 Background and overview

From its first formulations in the twentieth century, quantum mechanics provided a gateway to new ways of understanding and manipulating the world around us from early experiments, which revealed non-classical quantum behaviors including quantization of energy [1], entanglement [2], and later the superposition of quantum states [3], to modern systems that can not only reproduce but also leverage such phenomena in semiconductor electronics [4] and emergent quantum technologies [5]. Today, commercial adoption of quantum technologies has already revolutionized fields such as secure communication and metrology, with recent progress in quantum control enabling a plethora of architectures for quantum information processing and simulation [6–13]. Remarkably, concurrent innovation in digital software and hardware made such progress possible, not only through experimental measurement and data processing, but also by direct classical simulations of quantum mechanics. Despite the inherent computational challenges posed by the exponential growth in the Hilbert space with system size, ever-growing computational power along with state-of-the-art simulation tools [14–19] provide a powerful way of approximating small many-body quantum systems, enabling model validation and the testing of new physics [20–25]. These simulation capabilities remain crucial at a time when quantum hardware is still susceptible to noise and imperfect control, and must therefore be benchmarked and supported by predictions from digital computers. This thesis is situated within that theory landscape. It presents a detailed study of the effects of laser phase noise in the context of coherent quantum evolution on neutral atom systems. In doing so, it contributes to the broader effort of developing robust simulation tools that can diagnose and predict the behavior of noisy intermediate-scale quantum systems.

Neutral atoms used for quantum information processing have been a topic of burgeoning interest since the turn of the century [26–28]. This architecture offers strong tuneable inter-atomic interactions via excitation to high-energy Rydberg states, which can be operated in either dipole-dipole or Van der Waals interaction regimes. This approach provides several advantages over other quantum platforms, including physically identical qubits that can be dynamically rearranged while preserving coherence [29], parallel gate implementations, and a comparatively straightforward way to scale to hundreds and even thousands of qubits in arbitrary geometries using optical tweezer arrays [30, 31]. This is in contrast to other prominent approaches such as superconducting and trapped-ion platforms, in which dense packing of qubits typically comes with issues with connectivity and thermal loss [32–35]. However, the challenge with neutral atoms is the precise control of individual qubits and their interactions, as well as the relatively slow speed of read-out protocols [28, 36]. Current work on these limitations includes maintaining high-fidelity gate operations in the presence of laser noise and atomic motion [37], mitigating atom loss and dephasing due to environmental factors [38], and implementing reliable, scalable read-out and error correction schemes [39] that can be adequately benchmarked [40].

In addition to digital gate-based computation, neutral atom platforms are particularly well-suited for analog quantum simulation, where many-body quantum systems are engineered to directly emulate the Hamiltonians of complex physical models and solve optimization problems [41]. Dynamics can be introduced into such systems through the careful tuning of an external excitation laser or magnetic field, allowing for adiabatic evolution protocols [42] and annealing processes relevant for optimization [43, 44]. In this paradigm, strong, controllable interactions between atoms serve as a natural proxy for spin-spin couplings or bosonic field interactions. Unlike gate-based approaches that realize quantum algorithms through the compilation of unitary gates, analog simulators allow the system to evolve naturally under a programmed interaction landscape that mimics a given Hamiltonian or a particular cost function. Such simulation requires precise control of laser intensity and phase stability across large arrays of atoms, since spatial and temporal fluctuations can lead to non-uniform Rabi frequencies and detuning, thereby disrupting the engineered Hamiltonian [38]. Additionally, large-scale analog simulations demand significant laser power to drive coherent Rydberg transitions uniformly across all atoms, which can be challenging in two-dimensional arrays, especially at the boundaries. The heating effects from high-power laser illumination that cause off-resonant scattering and imperfect polarization, further degrade coherence and fidelity [45]. Another issue arises from finite temperature and atomic motion, which can cause atoms to drift from their trapping sites, perturbing the interaction landscape and creating unwanted disorder in the system. Finally, unlike digital quantum computing, error mitigation and correction techniques are less developed in the analog setting, making the system more susceptible to decoherence and requiring meticulous calibration to ensure reliable dynamics. While analog approaches are inherently less error-correctable than digital ones, they remain a powerful tool for probing quantum many-body systems that are classically intractable. As such, while the path to large-scale neutral atom systems is physically accessible, ensuring robustness and coherence across large arrays remains a central obstacle.

Given that one of the main limitations of neutral-atom systems is related to error mitigation and coherent control, understanding how imperfections propagate through many-body dynamics is essential. This is where classical simulation becomes especially valuable, as it allows us to isolate and model specific noise sources and their effect on the fidelity of operations, the stability of entanglement, and the overall evolution of quantum states. By incorporating realistic noise into simulations, we can predict the operational boundaries of near-term devices, guide experimental calibration, and even suggest new control protocols that are more resilient to imperfections. The work in this thesis embraces this approach, using a combination of tensor network and exact diagonalization methods to simulate a many-body neutral atom spin system under the influence of phase noise. In doing so, it aims to clarify the role of decoherence in scalable quantum architectures and contribute to the design of more robust quantum technologies.

The following sections provide further background on the main topics discussed in this thesis. We begin with a brief discussion of Rydberg atom platforms, introducing the mechanisms that make quantum computation and simulation possible. Following this, we briefly discuss state-of-the-art many-body experiments in both analogue and digital Rydberg platforms, before expanding on adiabatic state preparation in particular, as it will be the main process studied in this thesis. Moreover, we discuss different sources of noise in Rydberg systems, including laser noise, which will be our main focus. The final section of this chapter provides an outline for the rest of the thesis.

1.2 Rydberg atoms as a platform for quantum simulation

When an ultra-cold neutral atom is excited into a high energy Rydberg state it develops exaggerated properties including long lifetimes of order 100μs and strong polarizability a that scales with the principal quantum number n as $a \propto n^7$ [46]. The strong polarizability in particular makes a Rydberg excited atom an exceptionally precise electromagnetic sensor [47], as well as imposing off-resonance shifts in the energy states of any nearby atoms, thus prohibiting their excitation. A schematic diagram of this interaction is shown in Figure 1.1(a). The strong and tunable long-range interaction between Rydberg atoms is called dipole blockade [48], and its propagation along atomic arrays allows the production of highly entangled many-body states. Every atom along a chain can thus act as an independent qubit, responsive to external electromagnetic signals in microwave and tera-hertz frequency ranges, and connected with other atomic qubits through the blockade interaction. By carefully selecting the species of atom, a specific Rydberg state, and spatial geometry, experiments can be operated in either the van der Waals regime, where the interaction strength C_6 decays rapidly with distance R between atoms as C_6/R^6 [49–51], or the dipole-dipole regime, where strong resonant interactions of strength C_3 scale with R as C_3/R^3 [50, 52, 53]. This duality offers exceptional flexibility for both digital quantum computation, where two-photon excitation schemes [54, 55] enable single qubit rotations and the blockade interactions are used as a proxy for multi-qubit gates, as well as analog simulation of complex many-body Hamiltonians. In the regime of digital quantum computing, the qubit states are often chosen to be hyperfine ground states which are not so sensitive to external fields but allow for precise gate operations [28, 56], while the Rydberg interaction is used to enforce multi-qubit operations [57, 58]. In the analog regime, we typically use the ground-Rydberg coupling, because excitation is fast and can be run in either the Van der Waals or the dipole-dipole regime for different interaction dynamics. Atomic arrays with these interactions map directly

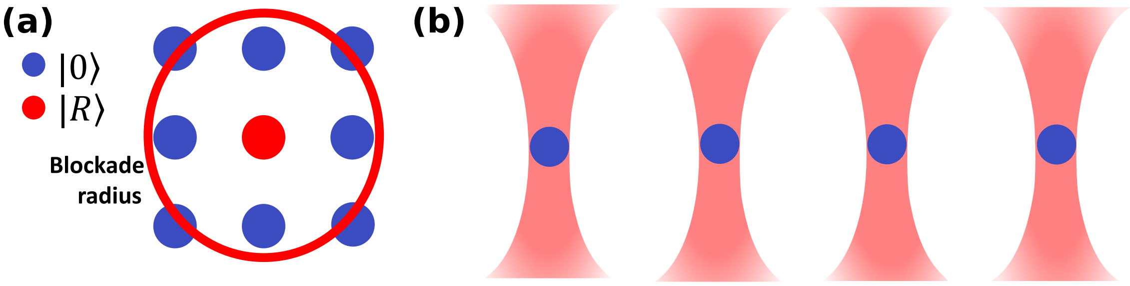

Figure 1.1: **Rydberg atom tweezer arrays. (a)** Diagrammatic representation of the Rydberg blockade in a two dimensional array of atoms. A single Rydberg excited atom (red) in the center imposes a Rydberg blockade on all nearby ground state atoms (blue) in the blockade radius, shifting the energy levels of any nearby atoms off-resonance, thus prohibiting their excitation. **(b)** Diagram of a one dimensional optical tweezer array of neutral atoms.

to spin systems in the Ising model as sites with a ground state atom representing 'spin down' and a Rydberg excited atom representing 'spin up' [41, 59], while spin-1/2 degree of freedom for more complicated models arises naturally in the dipole-dipole regime [60], or can be achieved by reintroducing hyperfine ground states [61] in the Van der Waals regime. A major advantage of Rydberg arrays is that every atom of a given species is physically identical to the next, which removes the potential for defects that, for example, could arise in superconducting qubits where each individual qubit must be independently engineered. Leveraging these properties of Rydberg atoms allows for the realization of single and multi-atom quantum gates [62, 63] enabling quantum algorithms and information processing, as well as precise preparations of many body Hamiltonians that open the door to simulation [64] and optimization of complex systems [36, 44].

Advances in modern laser technology have enabled the precise trapping and control of neutral atoms. After undergoing a series of cooling techniques [65] atoms are first trapped in a magneto-optical trap generated using counter-propagating laser beams with opposite circular polarization, after which the now ultra-cold atoms are typically trapped in 2D arrays using a spatial light modulator (SLM) that is capable of projecting holographic traps in arbitrary geometries [30]. These traps are loaded at random, but the atoms can be dynamically reconfigured in the SLM trap into two- or one-dimensional arrays using moving optical tweezer traps [66]. Figure 1.1(b) shows a schematic diagram of a one-dimensional Rydberg atom tweezer array. The traps discussed here are typically red-detuned, and have the main drawback of being repulsive to Rydberg-excited atoms, meaning that traps need to be momentarily switched off to perform Rydberg operations. It is also possible to devise magic wavelength trapping potentials that equalize the AC Stark shift between the ground and Rydberg levels that causes the repulsion [67, 68]. Alternatively, blue-detuned traps that hold atoms in intensity minima have also been developed [66], as well as circular geometry traps that use a circularly symmetric trapping well [69]. Further improvement can be achieved by integrating tweezer beams into the SLM that enable the dynamical movement of atoms between different sites and are typically used to realign atoms into a desired experimental array after the initial loading which is usually imperfect [29, 70, 71]. State-of-the-art tweezer arrays are now capable of dynamically transporting, improving inter-connectivity between sites and the general versatility of Rydberg experiments [39, 72, 73]. In addition, recent techniques such as Floquet frequency modulation have allowed interactions at ranges beyond the typical blockade radius [74], further boosting connectivity within large arrays. Finally, detection of Rydberg and ground states is done by illuminating atoms with resonant light which leads to fluorescence that can then be picked up in a high-sensitivity photon detector [58, 75, 76], as well as incorporating non-destructive readout methods where Rydberg atoms remain trapped even after measurement [77, 78]. A typical procedure of executing a quantum algorithm on a two-dimensional array and readout is shown in Figure 1.2, including an initial step for imperfect loading followed by subsequent rearrangement and initialization of a two-dimensional array in a square lattice to which an algorithm can then be applied. Algorithms are typically designed to be much shorter than trapping times such that the same atoms can be re-used for repeated realizations that allow for statistical evaluation of the prepared state.

Trap capacities of modern systems of alkali atoms reach over 6000 sites [45], with smaller demonstrations of arrays with molecules [79] and divalent atoms [80, 81] also achieved. As the control techniques for single- and multi-atom operations mature, the Rydberg platform continues to be promising for quantum computing and programmable quantum simulators, capable of probing strongly correlated physics and solving classically intractable problems. The following sections will discuss the current progress and limitations of the technology.

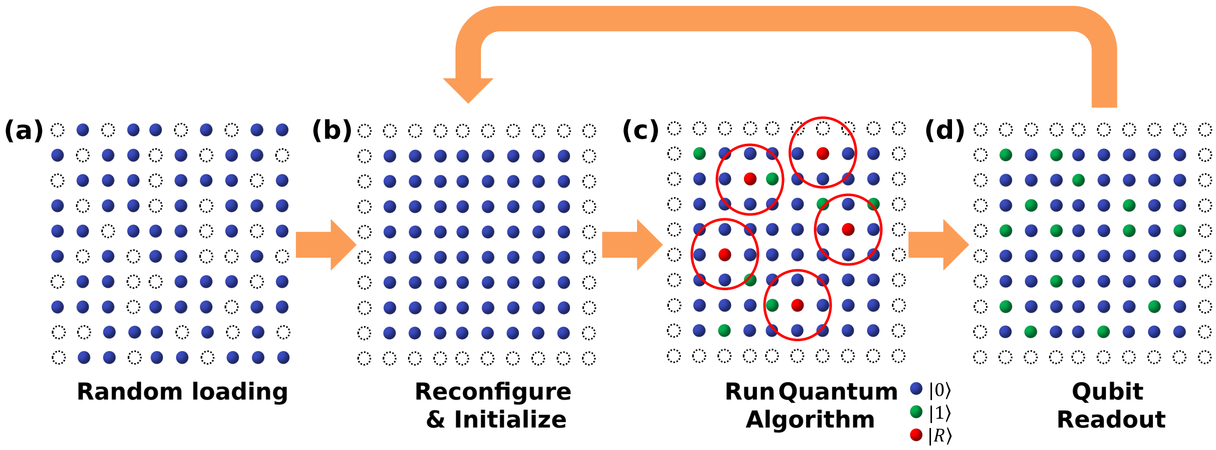

FIGURE 1.2: **Schematic workflow for running a quantum algorithm on a two dimensional Rydberg array. (a)** After cooling and trapping atoms get randomly loaded into a large two dimensional grid defined by the SLM. **(b)** Atoms get dynamically reorganized into a square lattice at the center of the two dimensional grid, and initialized in a hyperfine ground state.**(b)** A quantum algorithm is run, using two hyperfine ground states to represent $|0\rangle$ and $|1\rangle$, and a Rydberg state $|R\rangle$ to introduce interactions between individual atoms and realize multi-qubit gates. At this stage is also possible to dynamically reconfigure atoms to introduce increased connectivity. **(b)** Finally, qubit readout is performed across the grid at the end of the algorithm when all atoms are in either $|0\rangle$ and $|1\rangle$. After this, atoms are re-initialized into ground states through optical pumping and the algorithm is re-run for statistical significance.

1.2.1 Analogue and digital many-body experiments

Recent advances in coherent control [28, 62, 71] allowed for proof-of-concept demonstrations of devices that hold tens and even hundreds of qubits in arbitrary geometries and with dynamic operations [36, 82–84]. These systems are now large enough to perform not only proof of concept calculations, but can begin to explore useful algorithms and optimization and simulate interesting physical models.

Progress in quantum control and error mitigation has had a significant impact on quantum computation with Rydberg systems, enabling high-fidelity single- and multi-qubit gate operations in quantum algorithms [26, 85]. Substantial improvements in two-qubit [22, 86–91] and multi-qubit gate fidelities [92] have made it possible to execute small-scale algorithms on Rydberg atom arrays. A critical step toward fault tolerance involves error detection and correction, with recent advances including error mitigation protocols [93] and ancilla assisted error correction schemes [94], which detect and correct errors without collapsing quantum information. The large, programmable Rydberg arrays are well-suited for implementing such schemes, as their flexibility allows physical qubits to be efficiently arranged around ancilla qubits for measurement and correction cycles. These developments position Rydberg atom arrays as a strong competitor to trapped ions and superconducting qubits for scalable quantum computing. While trapped-ion systems still hold the edge in gate fidelities, Rydberg systems offer comparable gate speeds and superior native connectivity via strong long-range interactions, alongside highly reconfigurable qubit geometries. Although superconducting qubits currently benefit from mature fabrication and control infrastructures [95], Rydberg platforms are closing the gap in gate fidelity and scalability.

Along with digital quantum computation, the past decades have also seen extensive experimentation in analogue simulation with Rydberg platforms, focusing on the observation of many-body phenomena rather than the precise single- and multi-qubit gate operations required for quantum computation. A variety of Hamiltonian models have been explored, including the transverse-field Ising model [42, 59, 83, 96], as well as XY and XXZ spin models [55, 97, 98]. These platforms have been used to probe quantum phase transitions, critical phenomena, and dynamical processes such as thermalization and quantum scars, demonstrating their versatility in exploring complex quantum matter [41, 60, 99]. Beyond these, Rydberg-based simulators have enabled studies of topological models [100, 101], spin liquid phases [102–104], quantum many-body scars [62], and information scrambling [39, 105, 106]. These analogue approaches have also been extended toward solving combinatorial optimization problems, such as the maximum independent set (MIS) problem [36, 107], where atoms are arranged in programmable graphs with vertices representing qubits and edges corresponding to constraints enforced via Rydberg interactions. By tuning interaction ranges and laser detunings, these systems naturally evolve toward low-energy configurations that encode optimal or near-optimal solutions. Similar techniques have been applied to other classes of optimization problems as well [44].

1.2.1.1 Adiabatic state preparation

One experimental protocol which we discuss in further detail is adiabatic state preparation, as it will be used as a testbed for noise simulations presented in this thesis. Adiabatic state preparation is a widely used technique in many-body quantum physics, serving as a powerful method for initializing strongly correlated quantum states that are otherwise difficult to access. By slowly varying system parameters, this approach allows for the controlled transformation of an experimentally accessible initial state into a complex target state, provided that the evolution remains slow enough to satisfy the adiabatic condition and avoid unwanted excitations. This technique has been instrumental in quantum simulation, where it enables the study of exotic phases of matter [41, 42, 108], and quantum annealing, where it facilitates the search for ground state solutions to complex optimization problems [109–111]. Furthermore, recent proposals have even explored how it could be used to improve gate based computation [112]. In the case of Rydberg atom arrays, adiabatic state preparation provides a robust mechanism for generating highly ordered states, such as Rydberg crystals [59, 99] and spin liquid phases [102–104], that can be used for both quantum information processing and the study of nonequilibrium quantum dynamics.

The work done in this thesis simulates a Rydberg spin system in a transverse field Ising model (TFIM). The Ising interaction arises from the long-range Van der Waals or dipole-dipole interactions between individual Rydberg atoms, favoring specific spin configurations based on blockade effects [27, 113]. Meanwhile, the transverse-field term can be realized by a coherent Rabi laser drive, which couples ground and Rydberg states, inducing quantum fluctuations analogous to an external transverse magnetic field. For one-dimensional systems, crystalline ground states emerge through a competition between detuning in the laser drive and the blockade interaction forces ordered distribution of Rydberg excitations along the chain [42]. Such ground states are robust to small changes in detuning and the transverse-field, leading to small regions in the laser parameter space where the ground state is fully represented by a single configuration of excitations. The later chapters of this thesis will study this kind of adiabatic preparation of a ground state with antiferromagnetic excitation ordering [114].

1.2.2 Noise in Rydberg systems

Understanding sources of noise is a fundamental part of error mitigation in Rydberg platforms, especially in the context of analog quantum simulations and adiabatic protocols. In Rydberg systems, noise arises from both intrinsic and technical limitations, with significant consequences for coherence times and error rate, and ultimately the efficacy of computation and simulation experiments.

The primary source of intrinsic noise is spontaneous emission from Rydberg states, which decay on the order of 100μs due to blackbody radiation and spontaneous decay processes [27]. These events cause loss of coherence and population decay back to the ground state or even 'dark' states which lie outside of the computational basis, and in two-photon excitation schemes this can also happen in the intermediate state [115]. This spontaneous emission introduces errors during the evolution of quantum states, particularly in protocols that require long coherence times. Atomic motion inside optical traps is another source of error, as thermal movements lead to a Doppler shift with the incoming laser drive that effectively leads to random detuning proportional to the rms velocity of the particle [38]. This source of noise is especially pronounced in red-detuned optical lattices or tweezers (that are not adjusted to the magic wavelength), which repel Rydberg excitations and necessitate trap modulation during gate operations, temporarily releasing atoms and thus increasing position uncertainty. One method to suppress Doppler-induced detuning is to use counter-propagating excitation beams, where two lasers travel in opposite directions so that their wave vectors nearly cancel. This configuration largely removes the first-order Doppler shifts, reducing motional dephasing by up to an order of magnitude compared to single-beam setups [38]. Another significant limitation is imperfect atom loading and loss during operation, particularly when traps are turned off for Rydberg excitation. In analogue quantum simulations, where the goal is to accurately reproduce target Hamiltonians and observe collective many-body dynamics, such defects distort interactions and can drive the system away from the desired phase or critical point, reducing the reliability of state preparation and the fidelity of the simulated dynamics. Experimental efforts using rearrangement protocols, where optical tweezers dynamically move atoms to fill vacant sites, and real-time feedback, which monitors atom positions and reloads missing qubits during initialization, have mitigated some of these issues [39], but imperfections remain a non-negligible source of error in large-scale implementations.

Finally, Rydberg arrays also suffer from laser-induced noise mechanisms, which include amplitude and phase fluctuations in the driving fields, effectively modifying the intended unitary evolution and thus introducing off-resonant transitions [116]. Dephasing can originate from slow drifts in the laser detuning or environmental fluctuations (like mechanical vibrations or misalignment of optical equipment) that shift atomic energy levels unpredictably, including stray electric and magnetic fields. These shifts modify the effective detuning seen by the atom. Inhomogeneous broadening of global control pulses across the array can further compound this effect, making global control schemes less reliable. In the context of adiabatic state preparation, these noise sources collectively reduce the fidelity with which the final ground state is achieved. Dephasing, in particular, plays a critical role in adiabatic protocols, where the system relies on a coherent tuning of the laser drive to reach a desired state, and accumulated phase fluctuations lead to unwanted excitation. However, speeding up preparation to mitigate dephasing is also problematic as it leads to a loss of adiabaticity which in and of itself causes excitation. These effects become especially pronounced near critical points in the Hamiltonian parameter space where the energy gap closes and the adiabatic condition becomes hard to satisfy. In this thesis, we isolate the effects of laser phase noise in an adiabatic protocol for a one-dimensional transverse-field Ising model by introducing realistic phase noise profiles that modulate the Rabi frequency. This allows us to systematically study the resilience of a many-body Rydberg protocol under noisy conditions.

1.3 Outline of thesis

The main work done in this thesis is arranged into four chapters. Chapters 2 and 3 describe numerical tools used to generate the results in the thesis, including the stochastic simulation of realistic laser phase noise, and matrix product state techniques that are employed to scale simulations to larger system sizes. Chapters 4 and 5 contain the central results of the thesis, with Chapter 4 introducing the adiabatic state preparation experiment and the study of the effects of applying laser phase noise, while Chapter 5 takes a deeper dive with regards to the energy added into the system, in order to see if the state produced by the noisy experiment resembles a thermal state and the mechanisms behind such thermalization.

Chapter 2 serves as an introduction to the numerical simulation of stochastic systems and the generation of independent noise realizations with a target noise profile. After a brief discussion of the main sources of noise in modern Rydberg laser drives, we build a mathematical framework of stochastic simulation by defining two elementary stochastic processes in the Wiener process and the Ornstein-Uhlenbeck process. Through these probabilistic processes, we also introduce the analytical quantities of the power spectral density and the autocorrelation function that provide the link between the time and frequency content of a given signal and are therefore pivotal in stochastic numerical simulation. Despite several candidates, the algorithm we choose is based on the TK95 algorithm, which takes the power spectral density of a given signal and employs Gaussian sampling to create a unique frequency spectrum that can then be changed into an independent noise realization using the inverse Fourier transform. We also provide a detailed analysis of the validity of this approach, ensuring that averaged autocorrelation functions match the autocorrelation of the original power spectrum for a realistic noise source used in later Rydberg simulations.

Chapter 3 continues to build on the necessary numerical tools for the simulation of larger quantum system by introducing tensor network techniques and the corresponding matrix product state formalism used to simulate larger quantum mechanical systems. After showing how any arbitrary quantum state can be represented as a matrix product state and re-expressed in a canonical form that leverages orthonormality to improve performance, we also introduce matrix product operators that give us the ability to evaluate observables. Finally, we also incorporate time evolution using the time-dependent variational principle method, allowing us to do simulations of dynamical systems. Although these tensor network tools are all that is necessary to simulate the adiabatic state preparation experiment described in Chapter 4, for the thermalization discussion in Chapter 5 it is also necessary to introduce tools for finite-temperature calculations. The key idea is to express the density operator as a matrix product state by 'purifying' it, which means representing it as a pure quantum state in an enlarged Hilbert space that includes an auxiliary copy of the system. This approach makes it possible to apply standard real- and imaginary-time evolution algorithms that are designed for pure matrix product states. Starting from a maximally entangled state, which corresponds to infinite temperature, we evolve the system in imaginary time in small steps of inverse temperature. This procedure effectively cools the state to the target thermal energy. The resulting thermal state can then be compared with an adiabatically prepared state to determine how closely the system approaches true thermal equilibrium. All of the provided tensor network constructs described in Chapter 3 are also accompanied by a corresponding graph, which provides an easy to understand pictorial representation of the different elements used in tensor network calculations.

Chapter 4 marks the first result section but also formally introduces the physical experiment of adiabatic state preparation of an antiferromagnetic ground state along a one-dimensional Rydberg spin chain, using the noise generation algorithm from Chapter 2 to apply and study laser phase noise effects. The chapter begins by introducing the transverse field Ising Hamiltonian as realized on a spin chain of Rydberg atoms, and the emergent feature of stable ground states with crystalline ordering of excitations along the chain. We describe the specific adiabatic tuning of laser parameters to achieve a three-step protocol for the preparation of a ground state with antiferromagnetic ordering. Moreover, we provide an analysis of exact diagonalization simulations of the final step of the protocol on an 11 site system with no noise source and a variety of laser parameter variation rates, illustrating the link between variation rate and diabatic excitation. After this, we expose the protocol to an external noise source by introducing unique laser phase noise realizations as a modulation on the Rabi frequency of the transverse field, measuring its effects on the fidelity of the prepared ground state with the target anti-ferromagnetic ground state. These final fidelity evaluations are performed using matrix product state techniques introduced in Chapter 3. The effects of laser phase noise on adiabatic state preparation are explored further through excitation dynamics, as we look at matrix elements to identify the available transitions that facilitate phase noise excitation, as well as noisy evolution in time-independent Hamiltonians. Performing such an analysis for Hamiltonians that occur at different stages of the ramp provides insight into how the nature of phase noise excitation changes as the transverse field is reduced throughout the final stage of the protocol and the system becomes increasingly integrable.

Chapter 5 takes the analysis of phase noise excitation further by looking for potential signs of thermalization in the energy added to the system through phase noise excitation. We begin by introducing the eigenstate thermalization hypothesis, which is the prevailing approach for understanding thermalization in quantum systems. Given the relatively low-energy dynamics in adiabatic state preparation, we choose the canonical ensemble scaled by the Boltzmann distribution to generate thermal expectation values used to evaluate thermalization. Furthermore, we motivate the choice of two relevant observables in the interaction energy and long-range spin correlations for which thermalization is analyzed. We begin the analysis by evaluating thermalization after exact diagonalization simulations of the adiabatic state preparation in an 11-site spin chain, looking at how differences in the thermally predicted canonical ensemble and the diagonal ensemble of the final state combine with the energy distribution of a given observable to generate thermal and long-time expectation values. Analyzing expectation values for a variety of variation rates in the laser parameter provides a picture into how thermal and long-time expectation values converge. To further test the robustness of emergent thermalization of laser phase noise in this system, we also analyze simulations for a system with only nearest-neighbor interactions, as well as employing finite temperature calculations from Chapter 3 to evaluate thermalization in larger systems of up to 31 sites.

Finally, Chapter 6 concludes the thesis, reflecting on the results achieved and an outlook for future research.

1.4 Publications and presentations

The work in this thesis is largely based on the following publication:

- **Adiabatic state preparation and thermalization of simulated phase noise in a Rydberg spin Hamiltonian** *by Tomas Kozlej, Gerard Pelegri, Jonathan D. Pritchard, et al.* Eprint arXiv: 2505.04595 [117].

The manuscript represents the culmination of a four-year doctoral project focused on understanding the effects of laser phase noise in Rydberg atom systems. The research draws on extensive theoretical modeling and experimental validation, carried out in close collaboration with Gerard Pelegri and under the guidance and supervision of Jonathan D. Pritchard and Andrew J. Daley. Furthermore the work in this thesis has also been presented at two separate conferences:

- *Simulating Phase Noise in Rydberg Adiabatic State Preparation*, DESOEQ (2022)
- *Phase Noise Thermalization in Simulated Rydberg Adiabatic State Preparation*, IQTN (2024)

Chapter 2

Simulating laser phase noise

Lasers play a pivotal role in neutral-atom experiments, as the long coherence times and high fidelity needed for quantum computation and simulation with such atoms require lasers with exceptionally stable frequency and phase characteristics. Any error in the the output field of these lasers limits the efficiency with which atoms can be controlled. Reducing error caused by laser noise to levels close to or below that caused by the fundamental limit of spontaneous emission has therefore been a crucial goal in improving efficacy [118].

The focus of this work will be on optical control lasers, which have a narrow linewidth and operate at single frequencies to induce atomic excitations of the desired energy. Noise in the output of such lasers can come in many forms, such as power fluctuations in the supply, thermal variations, and misalignment of experimental apparatus [38, 116]. However, the most prominent sources of noise in the output of a laser can be defined in terms of amplitude noise, which affects the strength of the interaction between the atom and the optical field, as well as phase noise, which limits temporal coherence as well as the linewidth of the laser. Phase noise emerges as a dephasing error in Rabi oscillations, but can also be interpreted in terms of frequency where it causes jitter in the waveform of the output laser. The accumulation of such dephasing over the duration of an experiment leads to errors in single and many-body operations.

Understanding the effect of these errors on different experimental situations is critical to realizing the potential of Rydberg-based quantum technologies. Although such effects have been extensively studied for single atom excitation [38, 116, 118, 119], the effects of phase noise on many-body Rydberg experiments remain largely unexplored. Working towards this, the goal of this chapter is to document a method of simulating realistic laser phase noise stochastically from experimental laser data in Rydberg experiments.

Chapter 2 serves as introductory material to the analysis of stochastic systems as a tool for numerical simulation of realistic noise. Section 2.1 discusses potential sources of phase and amplitude noise in modern laser systems used in quantum experiments. Section 2.2 introduces methods for numerical simulation of stochastic processes, which provide a mathematical framework for random systems that proves integral when trying to simulate phase noise. We discuss the Wiener process in Section 2.2.1, which describes Brownian motion and is made up of independent Gaussian steps, called Wiener increments, that provide the building block for other more complex processes. Also, in Section 2.2.2 we introduce the Ornstein Uhlenbeck process which takes the Wiener increment and applies it to an exponential convergence to a predetermined equilibrium. In both cases we make use of several spectral analysis tools including the autocorrelation function which allow for the study of patterns, periodicity, or memory effects, as well as the power spectral density (PSD) which contains information on what frequencies dominate in a given process. Section 2.3 applies background knowledge from 2.2 to the realization of realistic phase noise signals. This is done by adapting the Timmer-Koenig (TK95 [120]) algorithm, described in 2.3.1, to the PSDs of phase noise spectra from experimental Rydberg lasers to simulate unique realizations that can then be used realistic noise in numerical models of Rydberg experiments.

2.1 The sources of laser phase noise

The two common types of laser sources commonly employed for the control of neutral atom qubits are diode lasers [121, 122], which use a semiconducting gain medium, and titanium sapphire (Ti:Sapph) lasers, which instead amplify light from a diode laser in solid-state cavities made out of titanium-doped sapphire crystals [123, 124].

In the case of diode lasers, amplitude noise can be caused by irregularities in the density of the carriers in the semiconducting gain medium, as well as electrical fluctuations of the power source [125]. In addition, thermal fluctuations in the gain medium may also contribute to this type of noise [126]. These types of noise are more prominent when the laser is operating at lower frequencies. On the other hand, phase noise in diode lasers arises primarily from quantum fluctuations in the gain medium, where spontaneous emission events introduce random phase perturbations [127]. These fluctuations contribute to the linewidth of the laser, often resulting in spectral broadening on the order of several MHz for standard diode lasers [116]. Additional phase noise sources include temperature-induced changes in the refractive index of the semiconductor gain medium and mechanical vibrations that perturb the optical path length. Electrical noise in the laser's driving current also modulates the refractive index of the gain medium, further contributing to phase instability. Although diode lasers are compact and efficient, achieving the narrow linewidths required for high-fidelity quantum control often necessitates stabilization techniques, such as feedback systems or external cavity designs. Such external cavity diode laser systems can exhibit enhanced phase noise, which can be effectively filtered using either a filter cavity [89] or by using feedforward techniques [128, 129].

Ti:Sapph lasers, which are optically pumped systems, exhibit distinct noise characteristics due to their solid-state gain medium and cavity configuration. Amplitude noise in these lasers can be significantly influenced by fluctuations in the pump laser intensity, as well as by thermal effects in the titanium-doped sapphire crystal. Absorption of pump light heats the crystal, leading to thermal lensing effects that modulate the gain profile and cavity stability [130]. Mechanical vibrations or misalignments in the optical cavity can further contribute to amplitude noise, which is more pronounced at lower frequencies [131, 132]. Phase noise in Ti:Sapph lasers often stems from mechanical and thermal instabilities in the cavity length, which directly alter the optical phase and lasing frequency [133]. Fluctuations in the wavelength or power of the pump laser can also indirectly induce phase noise in the output [134]. Although there is spontaneous emission noise in the gain medium, it is generally less significant than the noise introduced by environmental and mechanical factors. In continuous-wave operation, phase noise contributes to linewidths, ranging from tens of kHz to a few MHz, depending on the level of stabilization. In mode-locked Ti:Sapph lasers, phase noise manifests as timing jitter between successive pulses, requiring advanced stabilization techniques to minimize [60].

2.2 Stochastic methods

Since noise is stochastic by nature, simulating it requires an understanding of stochastic systems and their mathematical properties. We begin by simulating and studying the behavior of textbook example known as the Wiener process [135], a random walk with a step given by the sampling Gaussian distribution. Following this we take a look at the Ornstein-Uhlenbeck process [136], which can be described as Brownian motion with an underlying trajectory that converges to an equilibrium. Although simple, these two processes provide a solid foundation for building a stochastic algorithm that samples generic noise.

For the analysis of the stochastic systems it will also be necessary to evaluate their power spectral density (PSD), a power distribution in Fourier space across the frequencies that make up the signal. To derive a PSD $\tilde{A}$ for a particular function $f(t)$ we make use of the Wiener-Khinchin theorem [137, 138] which states that PSD of $f(t)$ in frequency space forms a Fourier pair with the auto-correlation function $A(t) = \big\langle f(t)f(t')\big\rangle$ in time space

$$\tilde{A}(\omega) = F[A(t)], \tag{2.1}$$

where F denotes the Fourier transform with a frequency step $d\omega$. In the case of numerical simulations where frequency and time are discrete, $d\omega \to \Delta\omega$ is equivalent to the inverse of the total number of data points in the original time signal $1/N$. For a given noise time series, the corresponding frequency spectrum $S(\omega) = F[f(t)]$ can be used to calculate a periodogram, which can be seen as a discrete-time approximation of the PSD for the continuous noise process being studied. To calculate a periodogram for a particular $S(\omega)$ simply perform

$$P(\omega) = d\omega \Bigg| S(\omega) \Bigg|^2. \tag{2.2}$$

Both the Wiener process and the Ornstein-Uhlenbeck process have a well-defined theoretical PSD, and we can compare this to the numerical evaluation.

2.2.1 The Wiener process

The Wiener process is the simplest stochastic system, describing the behavior of the position of a Brownian particle [139]. The process is formally defined as the contributions made by random white noise fluctuations ξ over a small period of continuous time t, or in the case of discrete time, the sum over all contributions of a random Gaussian step ΔW,

$$W(t) = \int_0^t \xi(n) dn \approx \sqrt{\Delta t} \sum_i^t \Delta W_i. \tag{2.3}$$

where Δt is the discreet time step. The Wiener process is a non-differentiable function and has the probability density from a initial position x_0 and time t_0 of

$$p(x,t|x_0,t_0) = \frac{1}{\sqrt{2\pi((t-t_0)}} \exp\left[-\frac{(x-x_0)^2}{2(t-t_0)}\right], \tag{2.4}$$

where x denotes the position of the process W at a time t. This process is thus governed completely by a Gaussian distribution with mean around the initial position and variance determined by size of the time difference being evaluated. Furthermore, the probability of finding the Wiener system at a given position $x(t)$ can be determined just by knowing x_0 and t_0. Such processes whose future evolution depends only on its present state and not on its past history are known as Markovian.

To understand the Wiener process, we can also study individual increments from one time to the next. Given that the probability distribution for this process is governed by the Gaussian distribution as seen in Eq. (2.4), it is not surprising that we can model each individual increment as an independent Gaussian impulse. We define such Wiener increments $\Delta W(t)$, where

$$\Delta W(t_i) = W(t_i) - W(t_{i-1}) \sim N(0, \sqrt{t_i - t_{i-1}}), \tag{2.5}$$

is just a Gaussian value taken from a normal distribution N centered around 0, and with a magnitude governed by $\sqrt{\Delta t}$. Hence every new ΔW_i is independently drawn out of the Gaussian distribution and is therefore statistically independent.

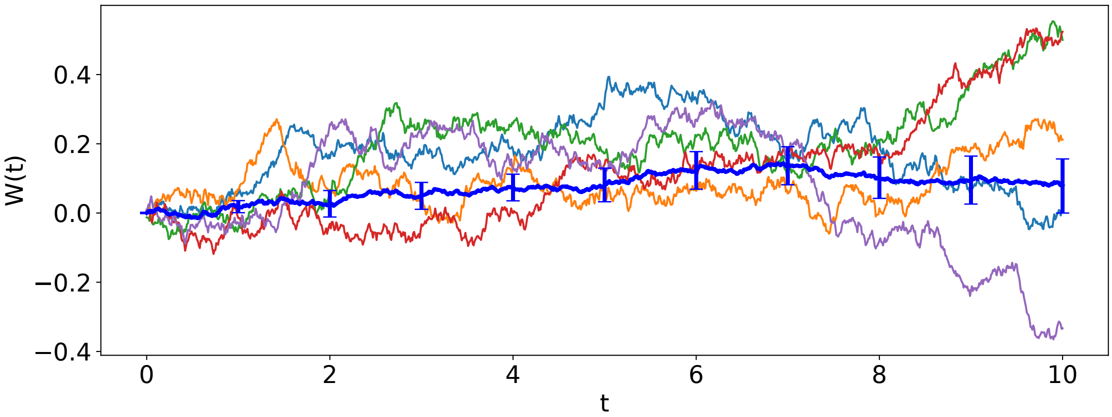

FIGURE 2.1: **Wiener process sample trajectories**. Five unique trajectories of the Wiener process $W(t_i) = W(t_{i-1}) + \Delta W$, with time step $dt = 0.01$ and Wiener increment ΔW given as a Gaussian variable centered around 0 and scaled by $\sqrt{\Delta t}$. The dark blue line shows averaged behavior over 20 unique trajectories, with error bars showing standard error increasing over time as average displacement stays close to 0, but individual trajectories diverge.

We can summarize the behavior of the expectation value and variance of the Wiener increment in the following two properties:

$$\langle \Delta W(t) \rangle = \int_{-\infty}^{\infty} x p(x,t|0,0) dx = 0, \tag{2.6}$$

$$\langle \Delta W(t)^2 \rangle = \Delta t. \tag{2.7}$$

Thus, the expectation value and variance of the Wiener process, which is just a finite sum of Wiener increments, satisfy the following two relations

$$\big\langle W(t) \big\rangle = x_0, \tag{2.8}$$

$$\big\langle [W(t) - x_0]^2 \big\rangle = t - t_0. \tag{2.9}$$

Both of these properties are evident in Figure 2.1, which depicts five sample trajectories of the Wiener process initialized at $x_0 = 0$. Even for a relatively small number of trajectories, we see that as time increases there is a large deviation of individual trajectories, with the average path oscillating around x as suggested by Eq. (2.8). This divergence explains the diffusive property of the Wiener process as standard error $\epsilon_S = \sqrt{(t - t_0)/n}$ (where n is the total number of steps), and therefore variance $t - t_0$, in the averaged behavior increases linearly with time, making this a non-stationary process.

In the case of numerical simulation, we work with discrete time ($\Delta t > 0$), with every time step used to evaluate a new increment. To begin with, we define a discrete time series of Gaussian variables W_t, starting at a given time t. Such a time series of increments starting from a time 0 is given by $W_0 = [\Delta W_0, \Delta W_1, \Delta W_3, ...]$ where $\Delta W_i \sim \mathcal{N}(0, \sqrt{dt})$ is an independent Gaussian variable.

Further insight into the Wiener process is given by calculating the autocorrelation function of different Wiener increment trajectories, revealing how a this process is correlated with itself over different time lags, revealing its temporal memory and characteristic timescales. The algorithm used to generate an autocorrelation $A(\tau)$ of a given time series $W_0 = [\Delta W_0, .., \Delta W_N]$ in terms of the lag τ is given as

$$A(\tau) = \langle W_0 W_\tau \rangle = \frac{\mathrm{cov}\big(W_0, W_\tau\big)}{\sigma(W_\tau)\sigma(W_0)}, \tag{2.10}$$

where $W_\tau = [\Delta W_{0+\tau}, .., \Delta W_{N+\tau}]$ is simply the same discrete array shifted ahead in time by τ, $\sigma(W_i)$ is the standard deviation of time series W_i, and the covariance of two functions $\mathrm{cov}(W_i, W_j)$ is given by

$$cov(W_i, W_j) = E[(W_i - E[W_i])(W_j - E[W_j])] = E[W_i W_j], \tag{2.11}$$

where we have used the fact that an array of Gaussian variables centered around $x_0 = 0$ will always have a mean of 0 and $E[W_i] = E[W_j] = 0$. At every individual lag τ the autocorrelation function takes a value $A(\tau) \in [-1, 1]$, where 1 signifies absolute correlation (A(0) is always equal to 1), and -1 signifies absolute anticorrelation. Also note that the initial time series W_0 is finite, and since we require ΔW_τ to be of equal size to evaluate $\langle W_0 W_\tau \rangle$, it is often convenient to generate a larger time series of $2N$ points, but only evaluate $A(\tau)$ for lags $\tau \leq N$.

To observe general autocorrelation properties of the Wiener process, a large number of independent trajectories must first be generated. After an autocorrelation has been calculated for every individual trajectory, we proceed to find an averaged autocorrelation across all trajectories $\bar{A}(\tau)$. Figure 2.2 a) shows that numerical

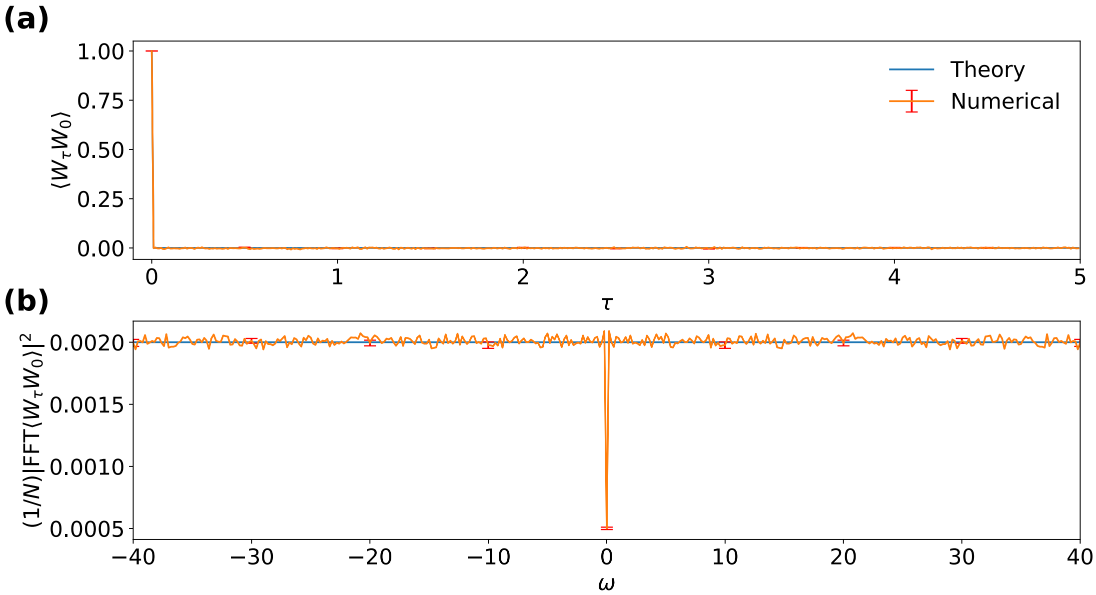

FIGURE 2.2: **Wiener process autocorrelation and power spectral density.** **(a)** The averaged autocorrelation function across 500 unique Wiener processes. Each Wiener process is of length $N = 1000$, with each Wiener increment ΔW an independent Gaussian variable scaled by $\sqrt{dt} = 0.1$. **(b)** The corresponding PSD, symmetric around 0 frequency and oscillating around a normalized value of $1/(N/2)$. Error bars shown in red provide standard error for every 100 data points.

calculations of $\bar{A}(\tau)$ averaged across 500 unique Wiener processes approaches the Dirac delta function. Hence, the Wiener process has no temporal autocorrelation, which is exactly what is expected for a time series with statistically independent values.

This type of analysis can be take one step further, as $\bar{A}(\tau)$ can be used to generate the PSD for the Wiener process using Eq. (2.1). To achieve this, we first perform a discrete Fourier transform

$$DFT[\bar{A}(\tau)] = F(\omega) = \sum_{\tau=0}^{N/2} \bar{A}(\tau) \exp\big[-2\pi i \frac{\omega\tau}{N/2}\big]. \tag{2.12}$$

This function takes a complex time series as input and generates a complex output in frequency space, corresponding to a spectrum of individual frequencies excited to create the input signal. The central frequency corresponding to $\omega_0 = 0$ is often referred to as the DC frequency and is just the sum across the entire time series. Since $\bar{A}(\tau)$ is a real-valued function, the values for positive frequencies $\omega > 0$ of the Fourier transform will always be the complex conjugate of the values of negative frequencies $\omega < 0$. The PSD for the auto-correlation is then given by

$$PSD[\bar{A}(\tau)] = \frac{1}{N}|F(\omega)|^2.$$

The resulting spectrum can be seen in Figure 2.2 (b), oscillating around a normalized value of $1/(N/2)$ where $N = 1000$ is the number of data points taken. Because we are considering a real signal, the PSD is symmetric around the DC frequency, and the DC frequency itself tends to 0 as it is just the sum across all points in the Wiener process which will always have an average displacement of 0 for long enough signals.

Although the Wiener process is used as a key building block for defining random fluctuations in stochastic systems, it is not often used alone. This is because with a stationary mean displacement as seen in Eq. (2.8), and a variance that diverges as $t \to \infty$, this process can only model unconstrained diffusion. More interesting are physical systems that exhibit random fluctuations but eventually evolve into a steady state; in such steady state cases the Wiener process commonly appears in stochastic differential equations as a scaled noise term introducing a level of random fluctuation to the system. Explicitly we define a general stochastic process with random fluctuations as

$$x(t + \Delta t) = x(t) + a[x(t), t]\Delta t + b[x(t), t]\Delta W(t), \tag{2.13}$$

where $x(t)$ describes the position at time t, a is the drift rate term that describes the deterministic change in the trajectory of $x(t)$ (for example, a constant force), and b is the diffusion term that scales the random fluctuations of the Wiener process.

2.2.2 The Ornstein-Uhlenbeck process

The Ornstein-Uhlenbeck (O-U) process [140] is one of the simplest stochastic processes that describes colored noise, meaning that the value of the process at one time is correlated with its value at a previous time. Unlike the Wiener process, which has no stationary point and diverging variance as $t \to \infty$, the O-U process is described as stationary and Markovian, meaning that it converges to an equilibrium about which it fluctuates randomly. This can be achieved by specifying an underlying trajectory to the Wiener process through inclusion of a drift term k, and an equilibrium position μ, to which the process converges. The simplest version of a one-dimensional O-U process, initialized at $t_0 = 0$ with unit drift rate and noise strength chosen so that the stationary variance equals 1, has the following conditional probability density function (PDF):

$$P_{O-U}(x_1, t|x_0, 0) = \frac{1}{\sqrt{2\pi(1-e^{-2t})}} \exp\left[-\frac{(x_1 - x_0 e^{-t})^2}{2(1-e^{-2t})}\right], \tag{2.14}$$

where $P_{O-U}(x_1, t|x_0, 0)$ provides the probability of evaluating the process at position x_1 after an evolution time t, given an initial position of x_0. The corresponding stochastic differential equation for this simplified O-U process is then given by

$$dx_t = -x_t\, dt + \sqrt{2}\, dW_t, \tag{2.15}$$

where both the drift rate at -1 and the diffusion term at $\sqrt{2}$ are constant. Note that Eq. 2.14 can always be derived from Eq. 2.15 by solving the Fokker-Planck equation [136]. In the long-time limit $t \to \infty$, the process converges to its stationary Gaussian distribution

$$p_{O-U}(x) = \frac{1}{\sqrt{2\pi}} e^{-\frac{x^2}{2}}. \tag{2.16}$$

This O-U process is Gaussian in nature, fluctuating around $x = 0$ with random Wiener increments, and converging to $x = 0$ as $t \to \infty$. The mean and variance of this process are then given by

$$\langle x \rangle_{O-U} = \int_{-\infty}^{\infty} x p_{O-U} dx = 0, \tag{2.17}$$

$$\langle x^2 \rangle_{O-U} = \int_{-\infty}^{\infty} x^2 p_{O-U} dx = 1. \tag{2.18}$$

A theoretical value for the PSD of this O-U process can be derived using the autocorrelation function. The autocorrelation function itself can be attained using the probability density functions in Eq. (2.14) and Eq. (2.16) for a simplified O-U process. Assuming a starting position of $x(0) = x_a$ at time $t = 0$, and some final position $x(\tau) = x_b$ after a correlation time τ, the autocorrelation function of the simplified O-U process is defined in terms of probability distributions P_{O-U} and p_{O-U} and its solution can be derived as follows

$$\big\langle x(\tau)x(0)\big\rangle_{O-U}$$

$$\begin{aligned}
&= \int_{-\infty}^{\infty}\int_{-\infty}^{\infty} x_a x_b P_{O-U}(x_a,\tau|x_b,0)p_{O-U}(x_b)dx_a dx_b && (2.19)\\
&= \int_{-\infty}^{\infty}\int_{-\infty}^{\infty} x_a x_b\Bigg[\frac{1}{\sqrt{2\pi(1-e^{-2\tau})}}\exp\bigg(-\frac{(x_a - x_b e^{-\tau})^2}{2(1-e^{-2\tau})}\bigg)\Bigg]\frac{1}{\sqrt{2\pi}}e^{-\frac{x_b^2}{2}}dx_a dx_b\\
&= \frac{1}{2\pi\sqrt{1-e^{-2\tau}}}\int_{-\infty}^{\infty} x_b\bigg(\int_{-\infty}^{\infty} x_a \exp\bigg[\bigg(\frac{(-x_a^b - x_a x_b e^{-\tau} - x_b^2)}{2(1-e^{-2\tau})}\bigg)\bigg]dx_a\bigg)dx_b\\
&= \frac{1}{2\pi\sqrt{1-e^{-2\tau}}}\int_{-\infty}^{\infty} \sqrt{\pi}e^{-\tau}x_b^2\sqrt{2(1-e^{-2\tau})}\exp\bigg[\bigg(\frac{-x_b^2(1-e^{-2\tau})}{2(1-e^{-2\tau})}\bigg)\bigg]dx_b\\
&= \frac{\sqrt{2\pi}}{\sqrt{2\pi}}e^{-\tau} = e^{-\tau}, && (2.20)
\end{aligned}$$

where standard integrals for a Gaussian distribution were used in the penultimate step, with the resulting autocorrelation behaving like exponential decay in evolution time. Hence, the value of an O-U process at a given time will influence the subsequent values of the process to an extent that will decay exponentially as time increases. This ability of a stochastic process to affect its future evolution is what we refer to as color in a noise signal, and it is absent only in an idealized Wiener process in which each increment is independent of all others. To get the corresponding PSD from this simplified O-U process, one only needs to find the magnitude squared of its Fourier transform

$$\begin{aligned}
PSD_{O-U} &= \big|F[e^{-\tau}](\omega)\big|^2, && (2.21)\\
&= \left|\frac{1}{\sqrt{2\pi}}\int_0^{\infty} e^{-(1+i\omega)\tau}d\tau\right|^2,\\
&= \left|\frac{1}{\sqrt{2\pi}}{}_0^{\infty}\left[\frac{1}{1+i\omega}e^{-(1+i\omega)\tau}\right]\right|^2\\
&= \frac{1}{2\pi}\frac{1}{1+\omega^2}. && (2.22)
\end{aligned}$$

The resulting power spectrum thus takes the shape of a Lorentzian distribution.

In Eq. 2.15 we defined the simple O-U process that evolves around a constant value. Building on this, we define a stochastic differential equation for an O-U process with a non-zero equilibrium position that the system will eventually evolve to. The resulting stochastic differential equation takes the form

$$dx(t) = k(\mu - x(t))dt + \sqrt{D}dW, \tag{2.23}$$

where k is a term that scales the rate of convergence towards the equilibrium position μ, and the diffusion term $\sqrt{D}$ which is typically much smaller than k scales the fluctuations around the mean path. Note that the Lorentzian shape of the PSD for the simplified O-U process in Eq. (2.22) is exhibited by all O-U processes; changing the scales of k and $\sqrt{D}$ in Eq. (2.23) will only have an effect on the width and magnitude of the peak of the distribution. The numerical evolution of this O-U process is performed by iterative updating of the position at every individual time step. The differential stochastic equation in Eq. (2.23) can be adapted into the following discretized update rule

$$x[n+1] = x[n] + k(\mu - x[n])\Delta t + \sqrt{D}\Delta W(dt). \tag{2.24}$$

Numerical simulations of this process are shown in Figure 2.3, with an initial position at 0, which eventually stabilizes at $\mu = 1$. It can be seen that x continues to increase at a rate governed by the product of k and the distance from the equilibrium $(\mu - x[n])$, but does so while being constantly nudged off course by the randomly generated fluctuations of the Wiener increment term at every time step. It can also be seen that such a numerical O-U process approaches the theoretical prediction as the number of averaged simulations increases and the effect of the fluctuations diminishes.

The theoretical solution to the stochastic differential equation in Eq. 2.23 can be acquired using the technique of variation of parameters by setting the initial ansatz

$$f(x(t), t) = x(t)e^{kt}, \tag{2.25}$$

$$df(x(t), t) = kxe^{kt}dt + e^{kt}dx. \tag{2.26}$$

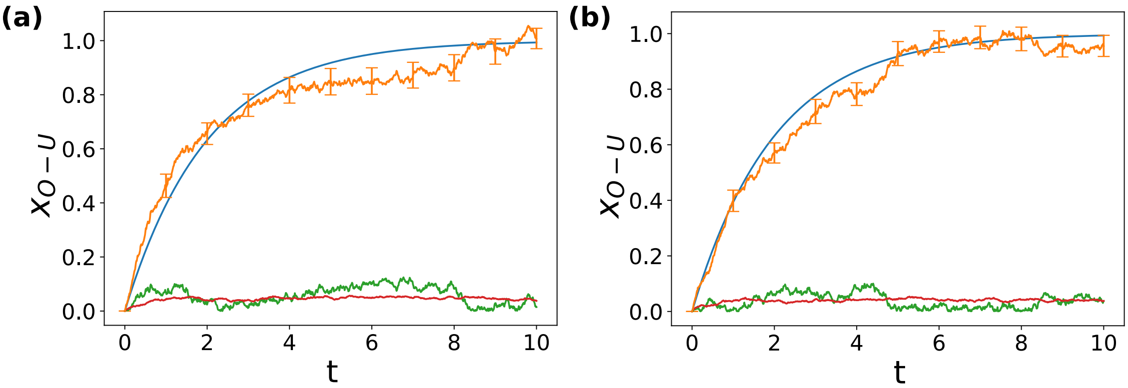

FIGURE 2.3: **The O-U process with equilibrium 1.** A simulation of the numerical O-U process with added Wiener increment stochastic noise as defined in Eq. (2.24) with parameters $k = 0.5$,$\mu = 1$, is shown in orange for **(a)** the averaged trajectory over 20 unique realizations and **(b)** over 100 unique realizations. The theoretical O-U process with no fluctuations given in Eq. (2.28) is shown using the blue line. Absolute error between theory and numerical evolution (green line), as well as standard error across averaged trajectories (yellow error bars and red line) are also provided.

Replacing dx in the differentiated ansatz in Eq. 2.26 with the stochastic differential equation in Eq. 2.23 leads to a cancellation of terms dependent on $x(t)$. We have effectively transformed to a 'co-moving' coordinate frame where the drift term is canceled out. Integrating both sides and replacing $f(x(t), t)$ for Eq. 2.25 yields the solution

$$x(t) = x(0)e^{-kt} + \mu(1 - e^{-kt}) + \sqrt{D}\int_0^t e^{-k(t-t')}dW(t'). \tag{2.27}$$

where the third term is a stochastic integral that acts as a summation of noise over a period of the time step. The full derivation of this result is provided in Appendix A. The theoretical solution for this process is given simply by $\langle x(t)\rangle$. Using the fact that $\langle \Delta W(t)\rangle = 0$ the theoretical expression, that also appears in Figure 2.3, is given by the average expected trajectory

$$\langle x(t)\rangle = \langle x(0)\rangle e^{-kt} + \mu(1 - e^{-kt}). \tag{2.28}$$

Deriving the autocorrelation function for this type of process is a little more involved than the simplified O-U process described in Eq. (2.19), but can be done directly from Eq. (2.27) as follows

$$\big\langle x(t)x(s)\big\rangle_{O-U} = \Bigg\langle\Bigg(x(0)e^{-kt} + \mu(1-e^{-kt}) + \sqrt{D}\int_0^t e^{-k(t-t')}dW(t')\Bigg) \tag{2.29}$$

$$\times\Bigg(x(0)e^{-ks} + \mu(1-e^{-ks}) + \sqrt{D}\int_0^s e^{-k(t-t'')}dW(t'')\Bigg)\Bigg\rangle,$$

$$= \langle x(0)^2\rangle e^{-k(t+s)} + \langle x(0)\rangle\mu(e^{-ks} + e^{-kt} - e^{-k(s+t)})$$

$$+\,\mu^2(1-e^{-kt})(1-e^{-ks}) + \frac{D}{2k}\big[e^{-k|t-s|} - e^{-k(t+s)}\big]. \tag{2.30}$$

This simplifies considerably for the case in which initial time $t = 0$, and $x(0) = 0$. The final form of the autocorrelation function is thus independent of μ, and is written as

$$\big\langle x(0)x(s)\big\rangle_{O-U} = \frac{D}{k}e^{-ks}. \tag{2.31}$$

The corresponding PSD is then derived using Eq. 2.1 by first taking the Fourier transform of this function

$$F\left[\frac{D}{k}e^{-ks}\right](\omega) = \frac{D}{2\pi k}\int_0^\infty e^{-(k+i\omega)s}ds \tag{2.32}$$

$$= \frac{D}{2\pi k}\left[\frac{1}{k+i\omega}\right], \tag{2.33}$$

and finally

$$PSD_{O-U} = \left|\frac{D}{2\pi k}\left[\frac{1}{k+i\omega}\right]\right|^2 = \left(\frac{D}{2\pi k^2}\right)^2\frac{1}{1+\left(\frac{\omega}{k}\right)^2}. \tag{2.34}$$

Thus, we retain the Lorentzian shape with half width at half maximum k. As shown in Eq. (2.31), the autocorrelation function of the O-U process has an exponentially decaying profile. Figure 2.4 shows the autocorrelation function for the more complicated stochastic process evaluated in Eq. (2.23). The autocorrelation function depends on both the rate of convergence k and the noise scale $\sqrt{D}$, as was derived in Eq. (2.31). The noise level also distorts the individual trajectories of the simulation and increases standard error, moving the autocorrelation closer to a Dirac delta function as the Wiener process becomes more dominant. Finally, Figure 2.4 also shows the numerically evaluated PSD for this O-U process plotted against the theoretical prediction of the Lorentzian function in Eq. (2.34). We can see that the width and peak of the Lorentzian shape is scaled by convergence rate

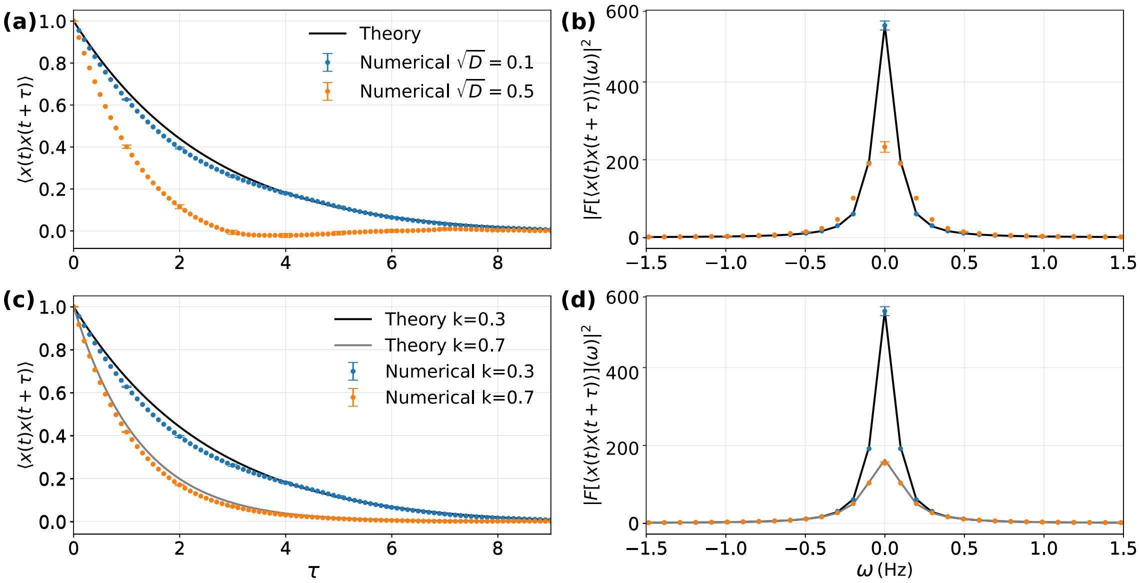

FIGURE 2.4: **Autocorrelation and power spectral density of the O-U process.** Plots show the averaged autocorrelation functions and PSD over 1000 unique realizations of the O-U process as derived in Eq. (2.31) with parameters equilibrium set to $\mu = 1$ and different parameters. **(a)** The autocorrelation function for the process with $k = 0.5$ and two noise strengths $\sqrt{D} \in [0.1, 0.5]$ in blue and orange along with the theoretical noiseless process shown in black, with the corresponding PSDs given in **(b)**. **(c)** The autocorrelation function for the process with $\sqrt{D} = 0.1$ and two convergence rates $k \in [0.3, 0.7]$ along with the noiseless processes shown in black and gray, while **(d)** shows the corresponding PSDs. Error bars in noisy process show standard error.

k, while the presence of Wiener noise distorts the process leading to a drop in the peak and a broadening of the full width half maximum as power shifts away from the central frequency.

2.3 Noise simulation

Sections 2.2.1 and 2.2.2 provided a look at two of the simplest stochastic processes, their features, and the numerical methods with which they can be modeled. Although basic, these models provide all the necessary tools needed to generate unique noise signals that can then be applied to quantum simulations. In the Wiener increment, we have a straightforward way of applying randomness (governed by the Gaussian distribution) to any given process. In the case of the O-U process, we apply the $\sqrt{D}$ of the Wiener increment to a function that convergences to a given equilibrium, which leads to increasing deviation from the underlying path as the randomness is scaled up. The characteristic correlation time of the

O-U process is well suited for modeling colored noise with an inherent relaxation mechanism.

Other approaches to simulating special kinds of noise include telegraph noise [141] in which signals may only occupy two or more discrete values often seen in quantum systems, as well as a class of autoregressive models which aim to generate noise signals recursively [142–144]. While these methods can effectively model certain types of stochastic processes, they are not always well suited for general noise signals encountered in experimental settings, particularly in the case of laser phase noise. Telegraph noise is inherently discrete and best suited for systems where noise switching occurs between well-defined states, such as charge fluctuations in solid-state qubits. However, laser phase noise is a continuous process with a broadband PSD, and it often follows a power-law spectrum, characteristics that telegraph noise fails to capture. Autoregressive models perform better in this case but, while capable of generating long-range correlated noise, require careful parameter tuning for different regions of frequency and may not naturally reproduce the precise spectral properties needed to match experimentally observed laser noise. In particular, standard autoregressive models are often limited in their ability to generate noise with an exact frequency ν dependence of $1/\nu^{\beta}$, where β is some fixed constant enforcing a power law. Such a spectral dependence of colored noise imposes artificial exponential correlations that need to be tweaked at different frequency ranges to mimic a smooth frequency-dependent structure seen in the spectral profile of laser phase noise.

The Timmer-Koenig (TK95) algorithm [120] presents a more flexible and physically motivated approach for generating laser phase noise. Unlike purely stochastic methods that rely on differential equations or recursive updates, the TK95 method directly constructs noise in the frequency domain by shaping a predefined PSD according to random Gaussian fluctuations of the Wiener increment. As opposed to the O-U method where we apply the Wiener increment to exponential decay in the time domain, the TK95 method proposes applying the increment to a given PSD in the frequency domain. This ensures that the generated noise accurately reproduces the experimental spectral characteristics of a PSD, including both low-frequency drift and high-frequency fluctuations. Additionally, because the method operates in Fourier space, it naturally captures correlations over long timescales without the need for an explicitly defined relaxation mechanism, making it particularly well suited for simulating phase noise in quantum control applications where spectral accuracy is critical.

2.3.1 The TK95 algorithm

The method that will be implemented for noise generation is based on the TK95 algorithm for the generation of unique time signals [120]. This is achieved by sampling a PSD using a complex Gaussian filter followed by the inverse Fourier transform. Although originally designed to generate power-law noise, it can be applied to any well-defined PSD. The algorithm can be distilled into the following steps:

1. **Choose a power spectral density**
   All that is necessary to begin the procedure is a single-sided PSD $S_P(\nu)$ of the desired noise signal. $S_P(\nu)$ can be any well-defined function on an evenly spaced frequency grid $\nu \in [0, \nu_{Nyq}]$, where ν_{Nyq} is the Nyquist frequency of the original signal.

2. **Generate a unique frequency spectrum**
   A unique single-sided frequency spectrum S_ν can be generated by using the Wiener increment ΔW to build real and imaginary components at a given frequency. To achieve this, draw two separate Wiener increments ΔW_1 and ΔW_2, and multiply by $\sqrt{S_P(\nu)/2}$ for the real, and $i\sqrt{S_P(-\nu)/2}$ for the imaginary frequencies as

   $$S_\nu(\nu) = \Delta W_1 \sqrt{\frac{S_P(\nu)}{2}} + i\Delta W_2 \sqrt{\frac{S_P(-\nu)}{2}}. \tag{2.35}$$

   Note that in the case of an even number of data points $S_\nu(\nu_{Nyq})$ is fully real (as it must be equal to its complex conjugate at $-\nu_{Nyq}$ since a real valued noise signal corresponds to a hermitian symmetric frequency spectrum) and thus only needs a single Wiener increment.

3. **Ensure real valued signal**
   To ensure that the generated noise signal is real-valued, S_ν is extended to a double sided spectrum with frequency grid $\nu \in [-\nu_{Nyq}, \nu_{Nygjq}]$, simply by taking the complex conjugate of all values generated in step 2.

   $$S_\nu(\nu) = S_\nu^*(-\nu). \tag{2.36}$$

4. **Get unique time signal**

   Finally, to get a unique discrete noise signal $\phi(t)$ we simply apply the inverse discrete fast Fourier transform to S_ν

$$\phi(t) = N\frac{\sqrt{2\Delta\nu}}{2\pi}\sum_{\nu=0}^{N-1} S_\nu(\nu)e^{2\pi i\nu t/N}, \tag{2.37}$$

   where N is the number of frequency bins, and $\Delta\nu$ is the frequency step in the frequency grid for on which S_ν is defined.

Initially, the TK95 algorithm was created to generate colored noise, in which a given PSD behaves as a function of frequency ν as $S_\nu = 1/\nu^\alpha$, and the value of α dictates the characteristic behavior of the noise. Figure 2.5 provides a demonstration of this algorithm, generating white noise with the characteristic parameter $\alpha = 0$ and brown noise with the parameter set to $\alpha = 2$. The two noise models are generated independently using their respective functions over a frequency grid of $\nu \in [0, 1]$Hz. After this, we generate one hundred unique frequency spectra for each PSD using the Wiener increment sampling described in Eq. (2.35), and turn them into unique time signals using the Fourier transform shown in Eq. (2.37) that we can then analyze. In the case of white noise we see a highly variable noise signal with a flat PSD, meaning that power is equally distributed along the entire frequency spectrum. Brown noise, on the other hand, presents itself with a $1/\nu^2$ drop off in power, meaning that it is dominated by long time-scale noise and individual trajectories resemble a random walk. The standard error is fixed as the TK95 process is sampling a stationary power spectral density, and for 100 trajectories the error bars are approximately 10 times smaller than the maximum displacement from the mean. Figure 2.5 also provides averaged periodograms, calculated as seen in Eq. (2.2). In this way, we can check that, on average, the noise signals generated by the TK95 algorithm are representative of the desired spectrum.

However, the TK95 algorithm also has several shortcomings that need to be addressed where possible. The first of these is the fact that the sampled power spectral densities are defined on a discrete frequency grid, with frequency resolution limited by total duration of the generated signal that can lead to artifacts, especially in the low frequency spectrum. To mitigate this, we work with very small frequency steps, generating time signals that are much longer than typical

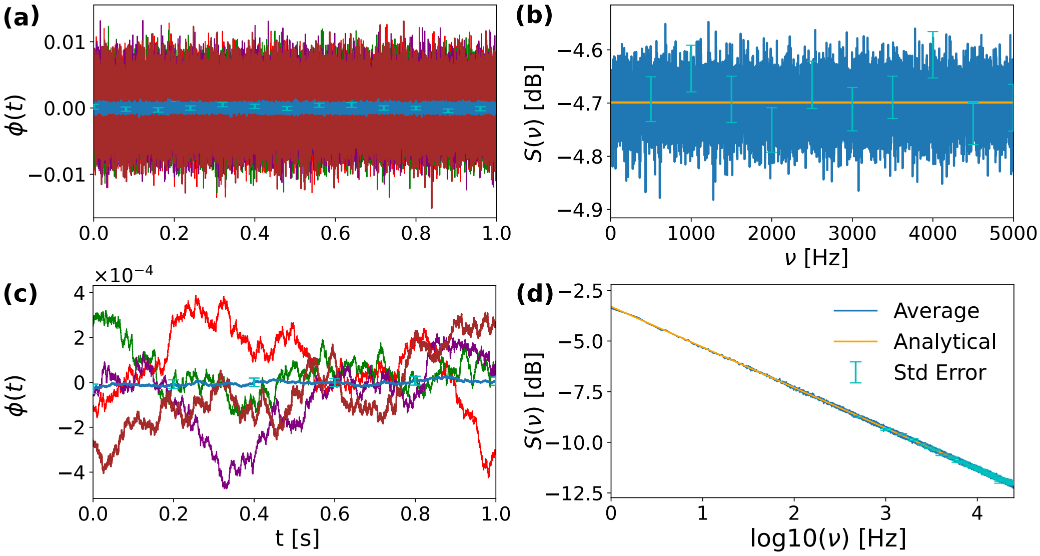

FIGURE 2.5: **Colored noise generated using the TK95 algorithm.** The TK95 algorithm is used (as shown in Eq. (2.35) and Eq. (2.37)) to generate 100 unique trajectories from a theoretical PSD of white noise **(a)** with a frequency profile of $S_\nu = 1/\nu^0$, as well as brown noise **(c)** with a frequency profile of $S_\nu = 1/\nu^2$, defined over a frequency range of $0 - 1$kHz. Averaged behavior is shown in blue, with four sample noise signals provided in different colors. The corresponding periodiograms in linear scale for white noise **(b)** and logarithmic scale for brown noise **(d)** averaged over 100 realizations are calculated using Eq. (2.2) are also shown in blue with theoretical PSDs shown in yellow. Cyan error bars shows standard error.

simulation times, but that can be reused for different trajectories. Additionally, the method operates purely in Fourier space, meaning it does not account for physical filtering effects, such as those arising from the response function of a laser or quantum system. Generally, the TK95 algorithm expects a stationary PSD, leading to noise signals with constant variance. Rectifying this by introducing time-dependent modulation of the PSD to capture non-stationary processes is beyond the scope of this thesis. Furthermore, while it can approximate power-law noise, this algorithm does not always generate long-range memory effects accurately, and these need to be tested by checking that generated noise has the same averaged autocorrelation as that of the original spectrum. Finally, because the sampling is inherently Gaussian and done on a constant spectrum, the TK95 algorithm is not able to reproduce noise with non-Gaussian statistics or time dependence. Nevertheless, this type of spectral method allows for the generation of uniquely varying signals that have a consistent and predictable overarching behavior.

2.3.2 Generating simulated laser phase noise

Having introduced stochastic processes as well as the TK95 algorithm we can now focus on generating phase noise signals. In the TK95 algorithm we have a spectral method for noise simulation that can be applied to general spectra, and adapting this method to experimental laser noise is mainly an exercise in units and scaling to ensure that the generated noise signal represents the physics correctly.

To begin with, a sample PSD of laser phase noise S_ϕ must be chosen. The PSD used for all noise generated in this thesis is taken from an experimental diode laser shown in Figure 2.6(a) with a similar behavior profile to the one described in [38], originally provided in units of frequency noise S_ν. S_ν has a broad peak power centered around 490kHz, with a linear drop-off for lower frequencies and residual power in higher frequencies. The frequency spectral density S_ν can be transformed into a phase spectral density S_ϕ using the relation $S_\nu = \nu^2 S_\phi$ [145]. To improve the performance of the TK95 algorithm, we define a frequency grid with discrete frequency step of $\Delta\nu = 1$kHz, which is small enough to ensure that the PSD is well represented, while leading to a longer time signal that can be spliced and reused to save computation time. Furthermore, to ensure that the time step of the generated noise signal is small enough to capture the effect of noise on dynamical simulations, we extend the frequency window of S_ν from 2MHz to 20MHz. Given that our data is only defined until 2MHz, we first take the naive approach of extending the final value of S_ν to the rest of the frequencies, which has a limited effect on generated noise given the $1/\nu^2$ drop off on high frequency power when converting S_ν to S_ϕ. Finally, given that S_ν has a low power below 100 kHz, we mitigate low-frequency artifacts that often affect the performance of the TK95 algorithm for shorter noise signals by setting all power below 33kHz to 0. Moreover, in the case that the laser PSD is initially provided is terms of voltage S_V, we refer the reader to [146] where the conversion to S_ϕ is discussed in detail. Viable spectral densities of experimental lasers can also be found in literature [38, 118].

Once an appropriate S_ϕ has been established, steps 2,3, and 4 of the TK95 algorithm can be applied to generate unique phase noise signals $\phi(t)$ that can be readily implemented into time evolutions of a many-body Hamiltonian. Figure 2.6(b) shows three samples $\phi(t)$ generated from S_ν, where the peak power of 490 kHz shown in Figure 2.6(a) makes the signals appear dominated by low frequencies when presented on a μs time scale. The averaged behavior of the generated

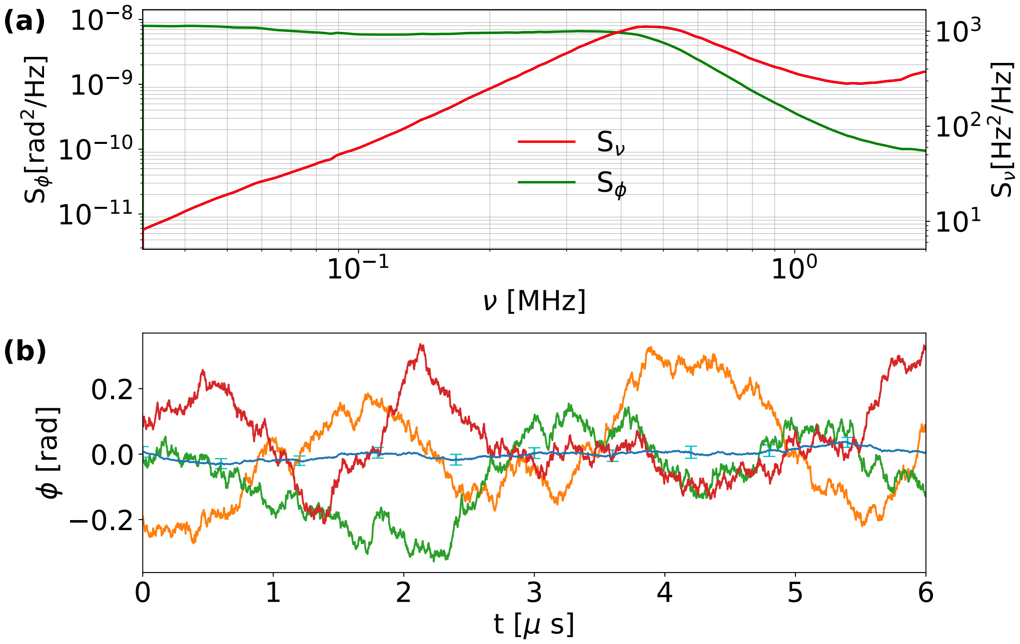

Figure 2.6: **PSD of laser noise, and corresponding TK95 noise signals.** **(a)** The phase noise spectrum S_ϕ (green) has been converted converted from a frequency spectrum S_ν (red) that has been taken from experimental diode laser witha a similar noise profile to one seen in [38]. The relevant conversion equation is $S_\phi = \nu^2 S_\nu$. **(b)** Three unique noise signals generated using the TK95 algorithm. Averaged noise behavior for 100 uniquely generated noise signals shown in blue.

noise across 100 trajectories shows much less oscillation, with variance that is fixed over time owing the fact that S_ν is constant. Figure 2.7(a) also provides some insight into the general shape of the generated noise in frequency space, with periodograms of phase an frequency noise maintaining the general shape and power of the original PSD in Figure 2.6(a) despite wild oscillations caused by the Wiener increment sampling.

To test the validity of the generated noise signals, we compare the autocorrelation function taken directly from the sampled spectrum $A_{S_\phi}(\tau)$ with the averaged autocorrelation across 100 generated noise signals A_ϕ. For this we once again make use of the Wiener-Kinchin theorem in Eq. (2.1), this time in reverse to generate an autocorrelation fuction for S_ϕ. Given that S_ϕ is provided as a discrete series in frequency space, approximating the inverse Fourier transform to a Riemann sum gives

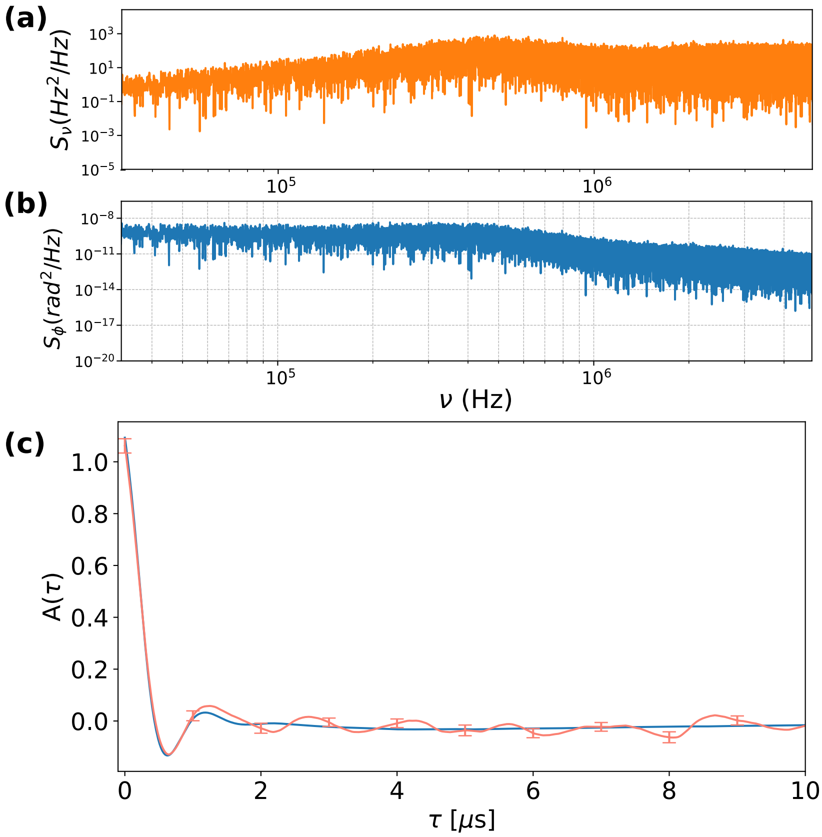

FIGURE 2.7: **Periodograms of autocorrelation of generated noise.** The frequency **(a)** and phase **(b)** periodogram of a single unique noise signal generated from the PSD in Figure 2.6(a) using the TK95 algorithm as described in steps 1-4. **(c)** Comparison of the autocorrelation function of the original power density spectrum (blue line) and an average of 100 autocorrelations corresponding to uniquely generated noise signals. Error bars represent standard error and show good agreement in average noise behavior.

$$A_{S_\phi}(\tau) = \frac{N\Delta\nu}{2\pi} \sum_\nu S_\phi(\nu) e^{2\pi i \nu\tau/N}, \tag{2.38}$$

where $A_{S_\phi}(\tau)$ is the autocorrelation function of the noise at a given time lag τ. In the case of atocorrelations for the generated phase noise, the autocorrelation of a given time series can be calculated as was done previously in Eq. (2.10) using

$$A_\phi(\tau) = \langle\phi_0\phi_\tau\rangle = \frac{\mathrm{cov}(\phi_0, \phi_\tau)}{\sigma(\phi_\tau)\sigma(\phi_0)}, \tag{2.39}$$

where ϕ_0 and ϕ_τ are the same noise signal starting from $t = 0$ and a lag of $t = \tau$ respectively. Figure 2.7(c) shows the agreement of autocorrelation functions of the original power spectrum S_ϕ and an average of 100 uniquely generated noise signals, providing evidence that the long time autocorelation decay is captured correctly for the specific PSD used. The validation confirms that the method described in this chapter successfully generates statistically unique noise signals whose ensemble-averaged behavior faithfully represents the original spectrum. By implementing these noise signals into the Hamiltonian evolution of many-body quantum systems, we can systematically explore the effects of phase noise on quantum dynamics and test the robustness of such systems against realistic noise fluctuations. This approach provides a powerful tool for investigating noise-induced decoherence and errors in quantum simulations and quantum information processing.

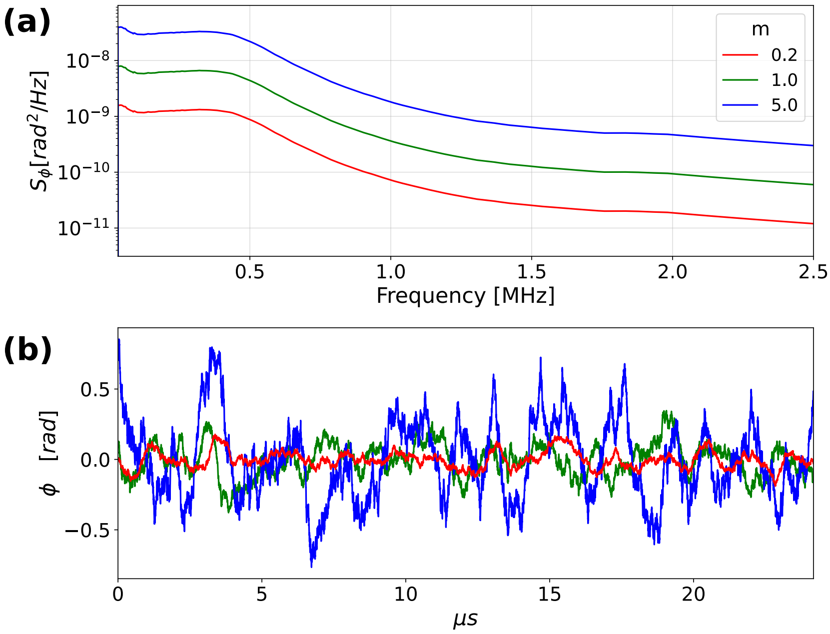

FIGURE 2.8: **Noise power scaling parameter.** **(a)** Phase noise power spectra of original laser phase noise seen in Figure 2.6 (green), along with two identical spectra (red,blue) that have their power scaled by a factor $m = 0.2, 5.0$ respectively. This factor is thus applied to the power spectrum S_ϕ before the Gaussian sampling step in the TK95 algorithm shown in equation (2.35).**(b)** The corresponding three unique laser phase noise time signals generated using the TK95 sampling algorithm are provided with matching colors.

2.3.3 Noise scaling

The method for noise generation detailed in the previous subsections can, in principle, be applied to any continuous power spectrum, assuming that the units are correctly scaled for the given purpose. This also means that we can generate noise with different frequency profiles simply by modifying our original spectrum. A relevant example which will also be used for analysis in the subsequent chapters is power scaling, which is done by introducing a simple scale factor m to a given power spectrum before performing the Gaussian sampling in the TK95 algorithm. Figure shows the phase spectra and corresponding noise signals of the original laser phase noise from Figure 2.6 and two different power scalings. The change in power directly translates to the magnitude of fluctuation seen in the generated noise signals, which are either amplified or suppressed by a factor of $\sqrt{m/2}$ via Eq. (2.35).

It is also possible to shift the peak of the noise to higher or lower frequencies, but since our noise data is defined only for a narrow bandwidth, we choose in our many body simulations to keep the noise fixed and instead tune the dynamical frequencies of the system that we study (in our case we will tune interaction strength between sites). This allows us to effectively study the same behavior without inadvertently introducing spectral artifacts that would need to be suppressed.

2.4 Summary

The main goal of Chapter 2 was to provide an adaptable algorithm for stochastic noise simulation that can be used to generate realistic phase noise signals with frequency profiles that resemble those of experimental Rydberg lasers. We began by providing a foundational understanding of numerical stochastic methods through the introduction of two textbook examples in the Wiener process [139] and the Ornstein-Uhlenbeck [140] process, which describe Brownian motion and noisy convergence to a predetermined equilibrium, respectively. Both of these processes introduce stochastic fluctuation using the Wiener increment, a Gaussian random variable with zero mean and variance proportional to the time step Δt. This term captures the inherent randomness of the noise and ensures that the fluctuations scale as $\sqrt{\Delta t}$, consistent with diffusive behavior. The Wiener increment also plays a role in the Timmer-Koenig (TK95 [120]) algorithm described in Section 2.3.1, chosen for the simulation of laser phase noise for the work in this thesis. The algorithm takes the Wiener increment and uses it as a Gaussian filter, sampling a target PSD in frequency space to create unique frequency spectra that can then be Fourier transformed into independent noise signals that retain the averaged behavior of the original sampled PSD.

The TK95 algorithm is detailed through its four-step process which involves defining a target PSD, generating a frequency-domain noise signal using Gaussian random fluctuations, symmetrizing the spectrum for real-valued output, and performing an inverse Fourier transform to produce time-domain noise. Initially used to create colored noise with varying spectral slopes as shown in Figure 1.2, Section 2.3.2 shows how the TK95 algorithm can be adapted to replicate experimental laser phase noise by appropriately scaling and converting experimental frequency noise PSDs into phase noise PSDs. The algorithm generates long-duration noise signals that match desired spectral profiles, and their validity is verified through autocorrelation comparisons against the original PSD using the Wiener-Khinchin theorem as shown in Figure 2.7. Although the method has limitations, such as its discrete frequency resolution and assumption of Gaussianity, it proves to be an effective and efficient way to simulate realistic phase noise in many-body quantum simulations, offering a statistically faithful representation of experimental noise for studying decoherence and robustness in quantum systems. Noise realizations such as those shown in Figure 2.6, along with the noise power scale factor shown in Figure 2.8, are used in Chapter 4 to study the effects of realistic laser phase noise in simulations of adiabatic state preparation in one-dimensional Rydberg spin chains, and later in Chapter 5 to study if and how the energy added into the system by such noise can lead to thermalization.

Chapter 3

Numerical methods

3.1 Tensor network techniques

The main problem of numerical simulations of many-body quantum systems is that the number of state coefficients required to express the entire Hilbert space grows exponentially with system size. While traditional mean-field approximations can provide useful insights and even become exact in certain limits, such as in high-dimensional systems or weakly interacting regimes, they generally fail to capture quantum entanglement and non-local correlations, limiting their accuracy in strongly correlated or low-dimensional settings. Hence, despite the growing importance of quantum mechanics and the growing complexity of quantum experiments, even small-scale numerical simulation often remained out of reach for general systems. By the end of the last century it became clear that a new approach was needed, one that could optimize memory usage while accurately preserving the essential properties of highly entangled quantum systems. This led to the formalization of Matrix Product States (MPS), a framework that describes quantum states through a chain of local tensors. While this structure is mathematically equivalent to the tensor-train decomposition later popularized in numerical analysis, its origins lie in the 1990s physics breakthroughs in finitely correlated states and the Density Matrix Renormalization Group (DMRG) [147–150]. Tensors are generalized arrays of numbers extending the concepts of scalars (rank-0), vectors (rank-1), and matrices (rank-2) to higher dimensions (rank-3 and beyond). In the context of quantum mechanics, where a state of a many-body system is defined by a complex-valued wavefunction with exponentially many coefficients, tensors offer a structured way to group and manipulate these coefficients. Each rank of a tensor can represent degrees of freedom associated with a physical site, entanglement bonds to neighboring sites, or time and measurement outcomes.

Importantly, efficient numerical algorithms have been developed to manipulate tensors in ways that retain only the most significant correlations, thereby greatly reducing memory demands for certain physically relevant states without sacrificing accuracy. These insights laid the foundation for tensor network representations of quantum mechanics that lend themselves to controlled and highly optimized truncation, pushing the boundaries of what can be achieved by numerical simulation. In fact, since its formalized implementation in 1992 [149], the tensor network approach of DMRG [151] and its more modern formalism of MPS calculations [152] have become the *de facto* numerical method for dealing with one-dimensional many-body quantum systems. Over the past decades, research and development of such MPS techniques, coupled with a rapidly increasing computational power, have led to the application of this numerical technique in a wide range of many-body models [153–158].

In principle, any quantum state can be expressed as an MPS, though, for highly entangled states, this representation may become numerically inefficient. The key advantage of MPS methods lies in its ability to encode and preserve the entanglement structure of a system, while identifying and removing the least necessary information with efficient truncation. This property makes MPS particularly well-suited for studying low-energy physics, as ground states of local Hamiltonians typically exhibit an area-law entanglement structure [159], allowing for efficient simulation. Ultra-cold atom gases in optical lattices are a pertinent example of quantum systems where these techniques have been shown to be useful [160]. Beyond representing quantum states, the tensor network formalism can be efficiently extended to represent other necessary components in quantum mechanics including Hamiltonians and time evolution operators. In particular, the density matrix renormalization group (DMRG) method exploits the MPS structure to efficiently find ground states of complex many-body Hamiltonians, while techniques like the time-evolving block decimation (TEBD) [161] and time-dependent variational principle (TDVP) [162, 163] enable real-time and imaginary-time evolution. Additionally, MPS allow for efficient computation of expectation values, overlaps, and correlation functions, further enhancing their utility in quantum simulations. However, it is important to note that a given quantum state does not have one unique MPS representation; different decompositions of the same state are related through gauge transformations, which can in some cases be leveraged to optimize numerical stability and algorithmic efficiency [152]. Extensions of MPS to higher dimensions are realized through projected entangled pair states (PEPS) [164], providing powerful methods for exploring correlated quantum systems, particularly in two-dimensional lattices. These properties collectively establish MPS as an indispensable tool in modern computational quantum physics, enabling simulations of strongly correlated systems that would otherwise be intractable.

The following sections provide introductory material to the MPS formalism, presenting tools that will become necessary to reproduce the adiabatic state preparation with laser phase noise in terms of tensor networks, as is done in the later chapters of this thesis. To begin with, we discuss the MPS representation for a generalized quantum state, followed by an equivalent representation for a quantum operator, and the overlap needed to reproduce expectation values. Next, we introduce time evolution of an MPS, which is done using the TDVP method that, unlike the TEBD method for time evolution, also represents long-range interactions needed for simulating Rydberg systems. Finally, we provide all the tools necessary for finite-temperature calculations using tensor networks, allowing for the evaluation of thermal states. For a more exhaustive review of DMRG techniques we refer the reader to the excellent review written by U. Schollwöck [152].

3.2 MPS representation of quantum many body states

For a system of N spin 1/2 particles, the wavefunction resides in a space of dimension 2^N, making direct computation infeasible for large N. The MPS formalism tries to tackle this issue by representing the coefficients as product of tensors, which then be decomposed and truncated precisely to retain only the information necessary to achieve an adequate approximation. For systems with small entanglement, where only a few coefficients dominate dynamics, such truncation can substantially reduce the data that must be saved while still ensuring that the approximation remains faithful to the exact state (e.g. in terms of state fidelity).

Without truncation, MPS is an exact representation of a quantum many-body wave function, and for a one dimensional lattice system of N sites it takes the

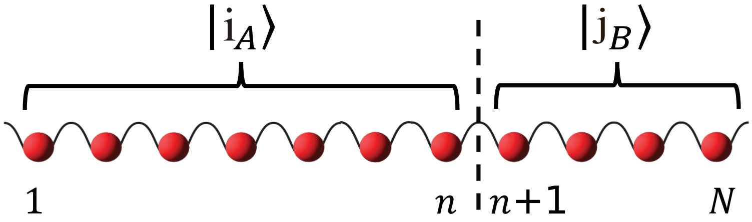

FIGURE 3.1: **Bi-partition of a one dimensional quantum system**. A one dimensional system of spin 1/2 particles partitioned into two blocks A and B with corresponding block-local orthogonal bases $|i_A\rangle, |j_B\rangle$. Note that i denotes a list of spins along the chain with $i_A = \sigma_1 ... \sigma_n$ and $j_B = \sigma_{n+1} ... \sigma_n$ given that $\sigma \in \left[| \uparrow\rangle, | \downarrow\rangle \right]$.

form of a product of tensors that hold information on their respective sites and their entanglement to other sites. To begin with we consider an N dimensional many-body quantum state $|\psi\rangle$ and its decomposition into state coefficients c,

$$|\psi\rangle = \sum_{\sigma_1 ... \sigma_N} c^{\sigma_1 ... \sigma_N} |\sigma_1 ... \sigma_N\rangle \qquad \sigma \in \{| \uparrow\rangle, | \downarrow\rangle\}, \tag{3.1}$$

where σ_i denotes possible states of individual sites with dimension d (in the case of spin states $\{| \uparrow\rangle, | \downarrow\rangle\}$ dimension is $d = 2$). The first step in a matrix representation of a quantum many-body state $|\psi\rangle$ is the rearrangement of the state coefficients $c^{\sigma_1 \cdots \sigma_N}$ into entries of a rectangular matrix Ψ with coefficients ψ_{ij} where i, j represent coefficient elements of two independent partitions that split the initial many-body state into two blocks A and B as seen in Figure 3.1. The second step is applying a singular value decomposition (SVD) [165, 166] to Ψ, meaning that our original state is transformed into

$$|\psi\rangle = \sum_{i,j} \psi_{ij} |i\rangle_A \otimes |j\rangle_B \overset{SVD}{\Rightarrow} \sum_{i,j,a_n} U_{ia_n} S_{a_n} V^{\dagger}_{a_n j} |i\rangle_A \otimes |j\rangle_B, \tag{3.2}$$

where the notation a_n represents entanglement between sites along the lattice, and we refer to these as ‘bonds’. The states $|i_A\rangle$ and $|j_B\rangle$ represent basis states in individual subsystems A and B, while the matrices U, S, and V arise from the singular value decomposition (SVD) of the coefficient matrix Ψ. Assuming that Ψ is an $m \times n$ dimensional matrix, the SVD yields three matrices: U, which has dimensions $m \times k$, S, a diagonal matrix of size $k \times k$, and $V^{\dagger}$, an orthonormal matrix with dimensions $k \times n$, where $k = \min(m, n)$.

The matrix U has orthonormal columns, satisfying the condition $U^\dagger U = \boldsymbol{I}$. The matrix S is a diagonal matrix containing the singular values $s_i \geq 0$ along its diagonal. These singular values are necessarily real and non-negative, and their total number defines the Schmidt rank r of Ψ, which satisfies $r \leq k$. Conventionally, singular values are arranged in descending order: $s_1 \geq s_2 \geq s_3 \geq \cdots \geq s_r$, all the way up to the maximal Schmidt rank of $r = \text{rank}(\Psi) \leq \min(d^m, d^n)$. Lastly, the matrix $V^\dagger$ consists of orthonormal rows, satisfying $V^\dagger V = \boldsymbol{I}$.

There is a direct link between the entanglement entropy and singular values found in the diagonal matrix S. This is derived by rewriting $|\psi\rangle$ after SVD decomposition in Eq. (3.2) in the Schmidt decomposed form

$$|\psi\rangle = \sum_a^r s_a |a\rangle_A |a\rangle_B, \tag{3.3}$$

where s_a are the singular values of S and r is the rank, while

$$|a\rangle_A = \sum_{i=1} U_{ia} |i\rangle_A \quad \text{and} \quad |a\rangle_B = \sum_{j=1} V^*_{ja} |j\rangle_B \tag{3.4}$$

represent the states on either side of S that represent the subsystem blocks A and B, and form two independent orthonormal sets. Using this, we can independently represent subsystems A and B separately in the form of traced density operators

$$\hat{\rho}_A = \text{Tr}_B \left[|\psi\rangle\langle\psi| \right] = \sum_a^r s_a^2 |a\rangle_A \langle a|_A, \tag{3.5}$$

$$\hat{\rho}_B = \text{Tr}_A \left[|\psi\rangle\langle\psi| \right] = \sum_a^r s_a^2 |a\rangle_B \langle a|_B, \tag{3.6}$$

The Von Neumann entropy of the joint system system is then given by

$$S_{A|B}(|\psi\rangle) = -\text{Tr}_A \left[\hat{\rho}_A \text{ln}(\hat{\rho}_A) \right] = -\text{Tr}_B \left[\hat{\rho}_B \text{ln}(\hat{\rho}_B) \right] = -\sum_{a_n} s_{a_n}^2 \ln(s_{a_n}^2), \tag{3.7}$$

and measures the entanglement information between a given bond. This link gives direct physical meaning to the singular values that are accessible after the SVD decomposition, but given that they are arranged in descending order these values provide an avenue for controlled truncation of the system.

However, before discussing truncation, it is important to show how the SVD can be used to represent a general quantum state $|\psi\rangle$ in matrix product form. After the SVD has been applied in Eq. (3.2), the joining of matrices U and S by matrix multiplication produces a matrix $A^{\sigma_n}_{a_n a_{n+1}}$, which consists of all the information on a given site including the physical index σ_n and the two bond indices of connecting sites a_n, a_{n+1}. Recursively performing SVD on $V^\dagger$ over all bonds and the subsequent reshaping of tensors U and S into tensor A provides an algorithm for turning an arbitrary quantum state into into a product of single site tensors that we refer to as an MPS

$$|\psi\rangle_{MPS} = \sum_{\sigma_1,\ldots,\sigma_n} \sum_{a_1,..,a_{N-1}} A^{\sigma_1}_{1a_1} A^{\sigma_2}_{a_1a_2} \ldots A^{\sigma_N}_{a_{N-1}1} |\sigma_1\sigma_2\ldots\sigma_N\rangle, \tag{3.8}$$

$A$where σ_i represents local basis states on a given site with a total dimension d (in the case of spins we have $\sigma_i \in \{|\uparrow\rangle, |\downarrow\rangle\}$ and $d = 2$). From this point onward we consider only matrix product states, such that $|\psi\rangle \equiv |\psi\rangle_{MPS}$. Note that up until the middle of the of the chain of matrices in Eq. (3.8) the matrix dimensions grow as $(d^i \times d^{i+1})$ where i is the index of the matrix, after which the dimensions shrink again as $(d^{N-i} \times d^{N-i+1})$. The representation in Eq. (3.8) is still exact, with an exponential growth in dimension up until $d^{N/2}$ saving no computational time.

If the entanglement is small, the elements on the diagonal of the matrix S which corresponds to the squared singular values $s^2_{a_n}$ decay rapidly and can thus be truncated without considerable loss of information. We refer to the maximum number of singular values retained after a decomposing of a quantum state as the maximum bond dimension D. If $D = 1$, the MPS is a classical product state with no entanglement, but as entanglement increases, the value of D necessary to represent the system faithfully grows too. In one dimensional and low-entanglement systems this growth in D is polynomial rather than exponential, with precision governed by the total sum of squared singular values discarded called the truncation weight

$$\epsilon = \sum_{a_n > D} s^2_{a_n}.$$

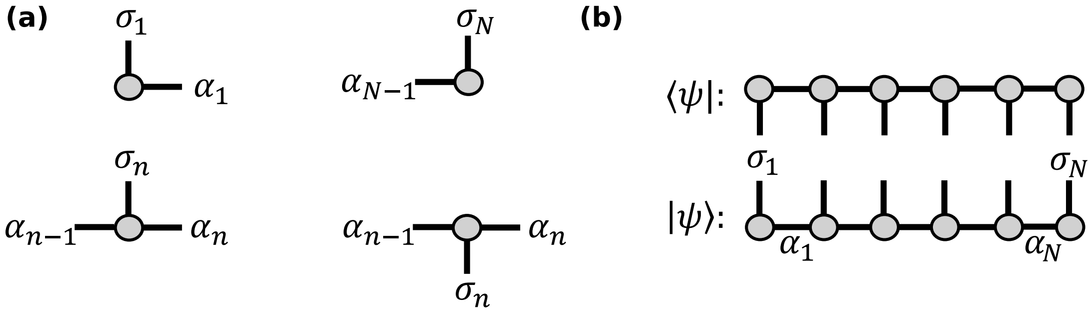

FIGURE 3.2: **Building block elements for diagrammatic representation of a MPS**. **(a)** Top row showing sites on the left and right edge of the chain for a ket MPS, while bottom row shows bulk sites for a ket (left) and bra (right) MPS. Vertical indices σ represent physical states, while horizontal indices α represent positions along the chain. **(b)** Diagram of bra and ket states of a one dimensional chain of sites. Joining all physical indices of bra and ket corresponds to a contraction of MPS resulting in a scalar value. The diagrams shown in this figure have been adapted from previous MPS literature in the review *DMRG: Ground States, Time Evolution, and Spectral Functions* written by U. Schollwöck [152].

Thus, a desired error tolerance for ϵ will set D to some maximum value, truncating the system and providing an efficient way of compressing information.

3.2.1 Graphical representation of an MPS

The MPS formalism can be expressed with greater readability in a diagrammatic representation. Figure 3.2 shows the basic representation of the matrix product state defined in Eq. (3.8), where each circle represents a tensor, $A^{\sigma_i}_{a_{i-1}a_i}$. In Figure 3.2(a) we see the diagrammatic elements that make up the building blocks of an arbitrary MPS, with edge sites represented by a single bond to the left or right, while bulk sites have connections on either side. Indices describing the physical state of a given site (spin in our case) are represented by a vertical lines pointing up in the case of a ket state, or down in the case of a bra state. Hence, a full MPS state resembles a comb, and the inner product of two states (also known as a contraction of tensors) has a bra and ket MPS joining at each site as seen in Figure 3.2(b). The following sections will build on this graphical representation, providing diagrams for all the different MPS elements that will be used throughout the thesis.

3.2.2 Canonical forms of an MPS

The MPS representation described in Eq. (3.8) is not unique, and other decompositions of the same physical state can be attained using a gauge transformation. While most such decompositions are not useful, specific representations can play a crucial role in optimizing numerical performance. One such useful representation is the so called canonical form of the MPS. In this form we transform bond indices along a given direction of the tensor product in a given MPS in a way that enforces orthonormality that can then be exploited by algorithms to improve efficiency. Redefining a given MPS in this canonical form plays a crucial role in DMRG and time evolution algorithms [154, 167].

In the left-canonical form, we enforce orthonormality for the left bonds. Referring back to Eq. (3.8), the condition for such left normalized tensors is that the left indices satisfy the equation

$$\sum_{\sigma,i} A^{\sigma}_{a_{i-1}a_i} A^{\sigma *}_{a_{i-1}a'_i} = \delta_{a_i a'_i}. \tag{3.9}$$

To transform a standard MPS into left-canonical form, we perform a QR decomposition [165, 166] iteratively to tensors across each site of an MPS starting from the left most site and working to the right. The decomposition of a given tensor $A^{\sigma}_{a_{i-1}a_i}$ results in an orthonormal matrix Q and an upper triangular matrix R with indices

$$A^{\sigma}_{a_{i-1}a_i} \overset{QR}{\Rightarrow} Q^{\sigma}_{a_{i-1}b} R_{ba_i}. \tag{3.10}$$

Next, we replace $A^{\sigma}_{a_{i-1}a_i}$ with $Q^{\sigma}_{a_{i-1}b}$ in the original MPS so that the left orthogonality condition is satisfied, and absorb the R matrix into the next site tensor, repeating until the last site is reached. After performing this procedure for all sites, the MPS is fully left-canonical.

Similarly, a right-canonical MPS is attained by performing a LQ decomposition across all tensors in a given MPS. This procedure is identical to its QR counterpart, this time ensuring right normalized tensors that satisfy the equation

$$\sum_{\sigma,i} A^{\sigma}_{a_{i-1}a_i} A^{\sigma *}_{a'_{i-1}a_i} = \delta_{a_{i-1} a'_{i-1}}. \tag{3.11}$$

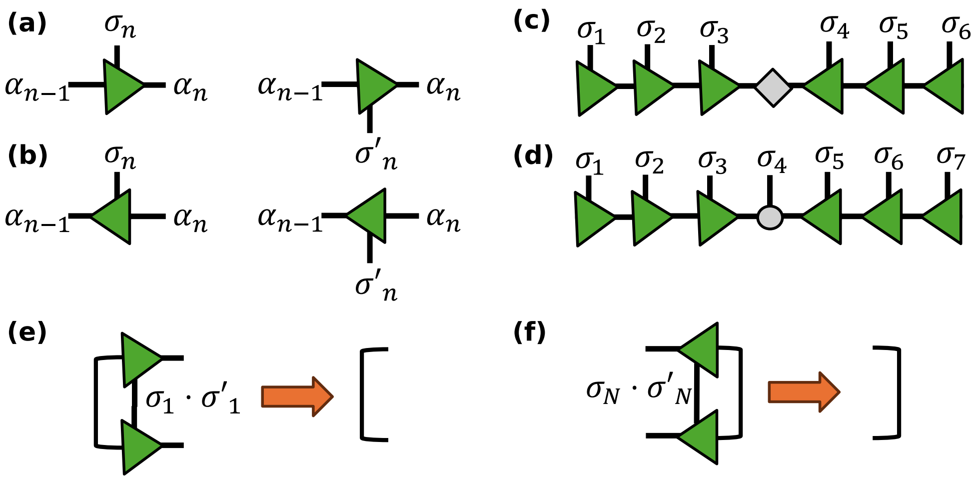

FIGURE 3.3: **Building block elements for diagrammatic representation of the canonical form of an MPS**. We include bulk sites of a ket and bra MPS in a left **(a)** and right **(b)** canonical form. Also provided is a six-site MPS in the mixed canonical form with a zero-site center **(c)**, as well as a seven-site MPS centered around an SVD representation on site four **(d)**. Finally, a contraction of a left **(e)** and right **(f)** edge site in the canonical form, resulting in an empty line that represents the identity matrix. The diagrams shown in this figure have been adapted from the review *Time-evolution methods for matrix-product states* by S. Paeckel [154].

Applying this decomposition starting from the right most site and working to the left results in the indices

$$A^{\sigma}_{a_{i-1}a_i} \overset{LQ}{\Rightarrow} L_{a_{i-1}b} Q^{\sigma}_{ba_i}. \tag{3.12}$$

After performing this procedure for all sites, the MPS is fully right-canonical. Individual right and left canonical sites are represented diagrammatically by arrow heads pointing in the direction of the canonicalization as can be seen in Figure 3.3. Importantly, right and left canonicalization can also be achieved using the aforementioned SVD by applying this decomposition from right to left for the right-canonical MPS and left to right for a left-canonical MPS. This approach is useful when you want to maintain access to singular values and thus the entanglement structure and controlled truncation, but is usually more computationally intensive.

However, it is the mixed canonical representation that is particularly useful for numerical algorithms. A mixed-canonical form MPS is one where tensors are left-canonical up to a certain site n, while tensors after n are right-canonical. A standard SVD is applied to the tensor a site n itself such that the MPS on this site takes the form

$$A^{\sigma}_{a_{n-1}a_n} = U_{a_{n-1}s} S_s V^{\dagger}_{sa_n}. \tag{3.13}$$

Here, U and $V^{\dagger}$ are unitary matrices, and S is a diagonal matrix containing the singular values obtained via SVD. The singular values in S correspond to the Schmidt coefficients of the bi-partition at site n.

To construct a mixed-canonical form we convert all tensors before site n into the left-canonical form using QR decomposition, and convert all tensors after site n into right-canonical form using LQ decomposition. Finally, at site n we apply SVD directly. We write such a mixed canonical matrix with a one-site center around site n as

$$|\psi\rangle_{1n} = \sum_{\alpha,\beta} Q^{[1:n-1]}_{\alpha,\alpha+1} \big|\phi^{[1:n-1]}_{L,\alpha}\big\rangle A^{\sigma_n}_{a_{n-1},a_n} |\sigma_n\rangle Q^{[n+1:N]}_{\beta-1,\beta} \big|\phi^{[n+1:N]}_{R,\beta}\big\rangle, \tag{3.14}$$

where the orthonormal basis states of the right and left canonical state are given by $\big|\phi^{[1:n-1]}_{L,\alpha}\big\rangle$ and $\big|\phi^{[n+1:N]}_{R,\beta}\big\rangle$ [152, 154]. Similarly, we can also define a mixed canonical $|\psi\rangle$ with no central site as

$$|\psi\rangle_{0n} = \sum_{\alpha,\beta} Q^{[1:n-1]}_{\alpha,\alpha+1} \big|\phi^{[1:n-1]}_{L,\alpha}\big\rangle C^{n}_{n-1,n} Q^{[n:N]}_{\beta-1,\beta} \big|\phi^{[n:N]}_{R,\beta}\big\rangle, \tag{3.15}$$

where $C^{n}_{n-1,n}$ is only a virtual index reference to the center of $|\psi\rangle$ where the orthonormality changes direction, and has no physical impact. Figure 3.3 provides the diagrammatic representation of right and left canonical site matrices, represented by right and left arrows along the chain. A mixed canonical MPS can be represented with a single non-canonical circle bipartitioning two opposite canonical states at a given site, while a zero-site mixed canonical MPS has no non-canonical site and is defined by a diamond. Due to their orthonormality, contracting in the canonical form is very simple as every site contraction results in the identity.

Just like any other MPS, a mixed canonical form of the MPS can be truncated in numerical simulations by retaining only bond indices that correspond to the D (desired bond dimension) largest singular values in S. Furthermore, the mixed-canonical form allows for easy access to the eigenvalues of the reduced matrices that describe the bipartitions, as they are just the squares of the singular values in S. This is particularly useful for operations involving entanglement entropy measurement. Finally, the orthonormality of the canonical form helps preserve normalization during time evolution algorithms such as TDVP. Such numerical optimization will prove critical to the work done in the following chapters, in which we will use mixed-canonical MPS to simulate adiabatic state preparation and perform finite-temperature analysis.

3.2.3 Matrix product operators

In quantum mechanics, the dynamics of a system are governed by unitary operators generated by Hermitian Hamiltonian operators, while measurements are described by other Hermitian operators (observables) whose eigenvalues correspond to possible outcomes and whose eigenstates determine the post-measurement state. For the MPS formalism to be useful, it must therefore be extended to include operators as well. Any given operator $\hat{O}$ consists of two sets of MPS indices σ' and σ and takes the form

$$\hat{O} = \sum_{\sigma}\sum_{\sigma'} c^{\sigma_1\cdots\sigma_N,\sigma'_1\cdots\sigma'_N} |\sigma_1,\cdots,\sigma_N\rangle\langle\sigma'_1,\cdots,\sigma'_N|, \tag{3.16}$$

where σ_n, σ'_n correspond to the physical basis indices of site n that act on ket and bra states respectively. The coefficient tensor $c^{\sigma_1\cdots\sigma_L,\sigma'_1\cdots\sigma'_n}$ holds the full information of the operator in a completely general form. However, similar to the case of quantum states, storing this tensor explicitly grows exponentially with the system size L, making it computationally infeasible. The Matrix Product Operator (MPO) formalism provides an efficient way to represent such operators in a form that can be stably truncated.

Just as an MPS represents a quantum state in a factorized tensor product form, an MPO expresses an operator in a structured manner using local tensor contractions. We perform the decomposition by rewriting the operator coefficients $c^{\sigma_1\cdots\sigma_L,\sigma'_1\cdots\sigma'_n}$ in terms of a product of local tensors $W^{\sigma_i,\sigma'_i}_{a_{i-1},a_i}$ defined at each site

$$\hat{O} = \sum_{\sigma_1,\dots,\sigma_N}\sum_{\sigma'_1,\dots,\sigma'_N}\sum_{a_1,\dots,a_{n-1}} W^{\sigma_1,\sigma'_1}_{1,a_1} W^{\sigma_2,\sigma'_2}_{a_1,a_2}\dots W^{\sigma_N,\sigma'_N}_{a_{N-1},N}|\sigma_1,\dots,\sigma_N\rangle\langle\sigma'_1,\dots,\sigma'_N|. \tag{3.17}$$

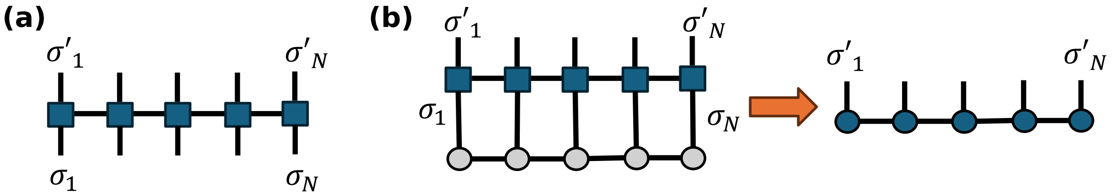

FIGURE 3.4: **Building block elements for diagrammatic representation of a MPO**. **(a)** Horizontal sites of an MPO are identical to MPS (see Figure 3.2), but two separate vertical indices need to be tracked; σ_i for the incoming site of a ket MPS, and σ_i' for the outgoing site of a bra MPS. **(b)** Diagram of a contraction of an MPO $|\phi'\rangle\langle\phi|$ and a MPS $|\psi\rangle$ to form a new MPS $|\psi'\rangle = |\phi'\rangle\langle\phi|\psi\rangle$ with physical indices σ_i'. The diagrams shown in this figure have been adapted from previous MPS literature in the review *DMRG: Ground States, Time Evolution, and Spectral Functions* written by U. Schollwöck [152].

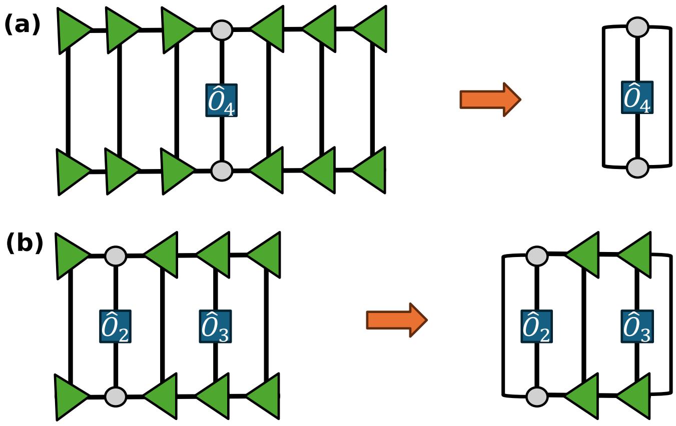

FIGURE 3.5: **Diagrammatic representation of single- and two-body operators for mixed canonical MPS**. **(a)** Expectation value of a generic single site observable $\langle\hat{O}\rangle$ acting on fourth site of a mixed canonical MPS of a seven site chain, and the corresponding reduced form after all right and left orthonormal sites are contracted to the identity matrix (see Figure 3.3(e,f)).**(b)** Two site correlation of a generic single site observable $\langle\hat{O}_i\hat{O}_j\rangle$ acting on second and third site of a mixed canonical MPS with a single site center on site two, along with the reduced form. The diagrams shown in this figure have been adapted from previous MPS literature in the review *DMRG: Ground States, Time Evolution, and Spectral Functions* written by U. Schollwöck [152].

Each tensor carries two physical indices σ_i, σ_i' representing the input and output states of the operator, along with two bond indices a_{i-1}, a_i that connect neighboring sites. The leftmost tensor has a single bond index a_1, while the rightmost tensor contracts with a_{n-1}, ensuring that the overall structure forms a one-dimensional chain.

To apply such an MPO to a given MPS we need only to perform a matrix multiplication of every MPS site with its MPO counterpart, ensuring that the correct indices are contracted. For each site i, we contract the local MPS tensor A^{σ_i} with the MPO tensor $W^{\sigma_i,\sigma_i'}$ to create a new contracted MPS

$$A'^{\sigma_i'}_{c_{i-1},c_i} = \sum_{\sigma_i} W^{\sigma_i,\sigma_i'}_{b_{i-1},b_i} A^{\sigma_i}_{a_{i-1},a_i}, \tag{3.18}$$

with new joined indices $c_{i-1} = (a_{i-1}, b_{i-1})$ and $c_i = (a_i, b_i)$, and the uncontracted σ_i' physical index replacing σ_i. Note that the bond dimension of the newly created MPS increases as $D' = D_{MPS} \times D_{MPO}$, and this growth can lead to computational challenges if left unchecked. Figure 3.4 provides the diagrammatic representation of an MPO, which takes the form of a chain of squares with identical horizontal indexing to an MPS, but with two vertical indices above and below to represent incoming and outgoing physical sites σ' and σ. A diagram of a generic MPO-MPS contraction is also provided. Finally, Figure 3.5 provides a diagrammatic demonstration of how the mixed canonical form simplifies calculations of single- and two-body observables, as all orthonormal sites to the left and right simply contract to the identity operator which makes operations much more efficient.

3.2.4 Time evolution

Unitary time evolution as represented by the operator $e^{-i\hat{H}t}$ is one of the most fundamental operations in quantum mechanics, enabling the study of dynamical systems. Standard numerical methods of time evolution can prove to be very resource-intensive, as they require either diagonalizing large Hamiltonian matrices or directly simulating the full wavefunction, both of which scale exponentially with the system size. For example, exact diagonalization is a widely used method [168], but it becomes computationally infeasible for systems with more than a few dozen particles, as the Hilbert space grows exponentially. Krylov subspace methods [169], which provide a more efficient means of approximating matrix exponentials, but they still face challenges when dealing with large or dense matrices. Moreover, these methods can be difficult to apply in systems exhibiting strong correlations or long-range interactions. Tensor network methods for time evolution developed over the past two decades have managed to leverage the compact memory-optimized form of the truncated matrix product state, making them the gold standard for most time evolution applications in one-dimensional systems [154].

The first tensor network time evolution schemes to be widely adopted made use of a time Trotterization approach, which decomposed the exponential of a total Hamiltonian into a repeating sequence of simpler short-time evolutions of its individual non-commuting terms. The earliest of these was the so called Time-Evolving Block Decimation (TEBD) [161, 170], which implemented a Suzuki-Trotter time step decomposition $e^{-i\hat{H}\Delta t/\hbar}$ [171, 172], providing a simple and scalable MPS time evolution method for low entanglement states. This family was later expanded by the tDMRG method [173, 174], which extended the DMRG algorithm, typically used to calculate ground state energy, to time evolution. However, these methods have the drawback of Trotterization error as well as a fixed bond dimension, which can lead to truncation errors as entanglement increases during an evolution. One way this can be mitigated is using a two-site update scheme to adaptively change the bond dimension the MPS and thus evolve for longer.

Another limitation to TEBD and tDMRG is that they are applied as local operators, meaning that they are not built to properly capture long range interactions in a system. The Time-Dependent Variational Principle (TDVP) [162, 163, 175] has emerged as a powerful alternative for time evolution, and in particular for systems with long-range interactions. The method projects the Schrödinger equation onto the MPS manifold, ensuring an optimal variational evolution of the state while dynamically adapting the bond dimension. This enables TDVP to efficiently handle non-local interactions by evolving the MPS within its natural variational subspace. Furthermore, like TEBD the TDVP method can be readily applied to imaginary time evolution [176], opening the doors for finite temperature analysis. All this makes TDVP particularly well-suited for studying the a system such as the transverse-field Ising Hamiltonian with long-range interactions discussed in the later chapters of this thesis (see Eq. (4.1)), where power-law decaying couplings can introduce significant entanglement growth over time. By allowing for an adaptive bond dimension and avoiding Trotterization errors, TDVP provides a accurate and adaptable method for capturing the complex quantum dynamics of such systems.

3.2.5 Time evolution with TDVP

The TDVP algorithm [162, 163] is a fundamentally different approach to time evolution than other TEBD based MPS time evolution schemes. Such schemes adapt the Lie-Trotter-Suzuki approximation for Hamiltonian exponentiation [171] to the MPS formalism, forming Trotter gates that can be applied to a given MPS to mimic the unitary evolution operator. Instead, the TDVP approach considers the variational manifold $\mathcal{M}$ of a given MPS, or in other words, the set that makes up the state-space of all possible states that can be occupied by an MPS $|\psi_D\rangle$ with a given bond dimension D. We also define A as the set of all the site dependent tensors $A^{\sigma_i}_{a_{i-1}a_i}$ that multiply to make the state $|\psi_D(A)\rangle$, that exists in the manifold $\mathcal{M}_A$. Applying time evolution to $|\psi_D(A)\rangle$ amounts to applying the Schrödinger equation

$$\frac{\partial|\psi_D(A)\rangle}{\partial t} = -i\hat{H}|\psi_D(A)\rangle. \tag{3.19}$$

However, because the Hamiltonian $\hat{H}$ naturally includes all states of the Hilbert space, applying such a unitary time evolution results in a state that has, at least partially, left $\mathcal{M}_A$. As opposed to applying a truncated local approximation to $-i\hat{H}$ as done in TEBD, TDVP implements a projector operator $P_{T_{\mathcal{M}_A}}$ that projects the Schrödinger equation onto the tangent space $T_{\mathcal{M}_A}$ of $\mathcal{M}_A$

$$\frac{\partial|\psi_D(A)\rangle}{\partial t} = -i\hat{P}_{T_{\mathcal{M}_A}}\hat{H}|\psi_D(A)\rangle, \tag{3.20}$$

thus forcing the evolved state to remain within $\mathcal{M}_A$ at all points of the evolution. At face value, this approach leads to a complicated set of non-linear equations that must be solved for all the degrees of freedom represented in $|\psi_D\rangle$, limiting the system sizes for which this approach was practical [162]. However, a breakthrough came in the realization that for an MPS in the mixed canonical form the projection operator can take the form

$$P_{T_{\mathcal{M}_A}} = \sum_{n}^{N} \hat{P}_L^{[1:n-1]} \otimes \hat{I}_n \otimes \hat{P}_R^{[n+1:N]} - \sum_{n}^{N-1} \hat{P}_L^{[1:n]} \otimes \hat{P}_R^{[n+1:N]}, \tag{3.21}$$

where $\hat{P}_L$ and $\hat{P}_R$ are site dependent projectors for the left and right canonical tensors of an N site system

$$\hat{P}_L^{[1:n]} = \sum_{\alpha=1}^{D} \big|\phi_{L,\alpha}^{[1:n]}\big\rangle\big\langle\phi_{L,\alpha}^{[1:n]}\big|, \tag{3.22}$$

$$\hat{P}_R^{[n:N]} = \sum_{\beta=1}^{D} \big|\phi_{R,\beta}^{[n:N]}\big\rangle\big\langle\phi_{R,\beta}^{[n:N]}\big|. \tag{3.23}$$

Here the canonical states $\big|\phi_{L,\alpha}^{[1:n-1]}\big\rangle$ and $\big|\phi_{R,\beta}^{[n:N]}\big\rangle$ are truncated to the bond dimension D, and so the application of this operator corresponds to an orthogonal projection on the reduced density matrix ρ_A of $|\psi_D(A)\rangle$ ensuring the evolved state remains in $\mathcal{M}_A$. The key advantage of writing the projection operator in this form is that it is possible to perform an exact integral of both terms in Eq. (3.21). The first term in Eq. (3.21) can be independently applied to a given $|\psi_D(A)\rangle$ arranged in a one-site mixed canonical form $|\psi_D(A)\rangle_{1n}$ from Eq. (3.14), while the second term is applied to the same state in the zero canonical form $|\psi_D(A)\rangle_{0n}$ from Eq. (3.15). It is then also necessary to redefine the Hamiltonian MPO appropriately: centered around n with a one-site center $\hat{H}_{1n}$, and a zero site center $\hat{H}_{0n}$ such that the right hand side of Eq. (3.21) becomes

$$\begin{aligned} -i\hat{P}_{T_{\mathcal{M}_A}}\hat{H}|\psi_D(A)\rangle = & -i\sum_{n}^{N} \hat{P}_L^{[1:n-1]} \otimes \hat{I}_n \otimes \hat{P}_R^{[n+1:N]}\hat{H}_{1n}|\psi_D(A)\rangle_{1n} \\ & + i\sum_{n}^{N-1} \hat{P}_L^{[1:n]} \otimes \hat{P}_R^{[n+1:N]}\hat{H}_{0n}|\psi_D(A)\rangle_{0n}. \end{aligned} \tag{3.24}$$

A diagrammatic representation of this equation is provided in Figure 3.6. If we collect all the tensors that multiply to make up $|\psi_D(A)\rangle_{1n}$ and $|\psi_D(A)\rangle_{0n}$ into the vectors $\mathbf{A}_{1n}$ and $\mathbf{A}_{0n}$, and make these tensor sets time dependent, the application of the full operator reduces to the solving of two independent differential equations

$$\dot{\mathbf{A}}_{0n}(t) = i\hat{H}_{0n}\mathbf{A}_{0n}(t), \tag{3.25}$$

$$\dot{\mathbf{A}}_{1n}(t) = -i\hat{H}_{1n}\mathbf{A}_{1n}(t). \tag{3.26}$$

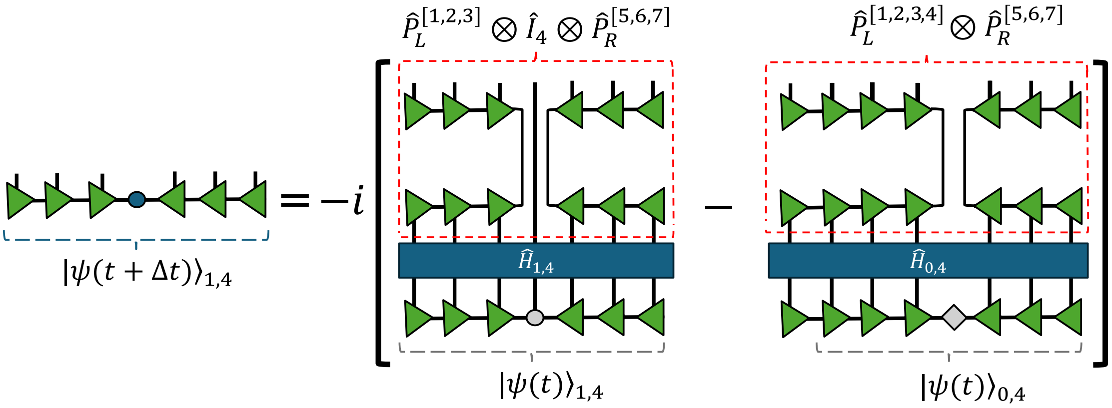

FIGURE 3.6: **Diagrammatic representation of a single TDVP operation**. The diagram above illustrates Eq. (3.21) [154] for a chain of seven sites using a variety of MPS elements introduced in Figures 3.2,3.3,3.4, 3.5 . On the left hand side of the equation we have a mixed canonical MPS of the evolved state. On the right hand side we see the two terms of the projector operator $\hat{P}_{T_\mathcal{M}}$ highlighted in red, and the corresponding single- and zero-site Hamiltonian applied to the correct form of the initial state. Subscripts $\{0,4\}$ and $\{1,4\}$ denote single- and zero-site tensor elements centered around the fourth site. The TDVP is applied with respects to the fourth site only, and the direction of time is from down to up.

This is effectively a system of N site dependent Schrödinger equations, with the corresponding solution

$$\dot{\mathbf{A}}_{0n}(t) = \exp\big[i\hat{H}_{0n}t\big]\mathbf{A}_{0n}(0), \tag{3.27}$$

$$\dot{\mathbf{A}}_{1n}(t) = \exp\big[-i\hat{H}_{1n}\big]\mathbf{A}_{1n}(0). \tag{3.28}$$

Thus, we have turned our projected time evolution problem into an exponentiation problem, for which we can implement the standard Suzuki-Trotter decomposition and Krylov subspace method [171, 177] used in TEBD and its variants of time evolution. Note here that the positive exponential in Eq. (3.27) can be interpreted as an evolution back in time.

The TDVP procedure then begins by a right to left sweep for all the sites along the chain. For a given site n, we first rewrite the MPS into a mixed canonical form with a one-site center around n to get a tensor vector $\mathbf{A}_{1n}(0)$ at time $t = 0$, computing also the corresponding Hamiltonian operator $\hat{H}_{1n}$. We then evolve forward in time according to Eq. (3.28) by a time step $\Delta t/2$, resulting in a new set of evolved tensors $\mathbf{A}_{1n}(\Delta t/2)$. Next, we perform an orthogonal decomposition of the evolved central tensor $A_n(\Delta t/2)$, resulting in the the left orthonormal tensor $A_{Ln}(\Delta t/2)$ and a tensor $C_n(\Delta t/2)$. The tensor $A_L(\Delta t/2)$ is now evolved and can be saved. Following this, we use the evolved tensors $\mathbf{A}_{1n}(\Delta t/2)$ construct a zero-site Hamiltonian operator $\hat{H}_{1n}$ (omitting the central site tensor), and use it to evolve the tensor $C_n(\Delta t/2)$ back in time by a time step $\Delta t/2$ according to Eq. (3.27). Finally, we absorb the de-evolved $C_n(0)$ into the right orthonormal tensor A_{Rn+1} on the next site, and rewrite the MPS in terms of a one site center at $n+1$ and redo the same steps to proceed with the algorithm. When the final site is reached, we do not need to perform orthogonal decomposition or backwards time evolution. To continue evolving we perform the same sweep but starting from right to left, performing the steps of the procedure in reverse such that they yield another evolution of $\Delta t/2$, leading to a total evolved time of Δt after two sweeps.

These steps constitute the TDVP algorithm for a single- site update, but simultaneous two-site updating is also possible, and is typically preferred in modern applications as it is more efficient [175]. Work is also being done to extend this algorithm to multiple dimensions [178]. For a mathematically rigorous derivation of $P_{T_{\mathcal{M}}}$, as well as the derivations and solutions of the differential equations that arise from applying it to an MPS, the reader is referred to [179], with the corresponding TDVP single- and double-site algorithms outlined in [175]. Given that $\hat{P}_{T_{\mathcal{M}}}$ can be constructed for arbitrary Hamiltonians, the TDVP method can be applied to systems with long range interactions for real and imaginary time, making it perfect for the Rydberg spin chain simulations performed in this thesis. From this point onwards, any tensor network time evolution discussed in this thesis can be assumed to have used the two-site TDVP algorithm implemented in the Julia ITensor TDVP package [17].

3.3 Finite temperature calculations

Another important capability of the MPS formalism is to perform finite-temperature calculations [152, 156, 180, 181], studying the thermodynamic properties of quantum many-body systems that are often too large to be represented by exact diagonalization. To achieve this, MPS-based methods represent the entanglement structure of one-dimensional thermal states efficiently as matrix product density operators (MPDO), which can then be used to represent thermal states of arbitrary energy. The standard strategy described in the following chapters involves

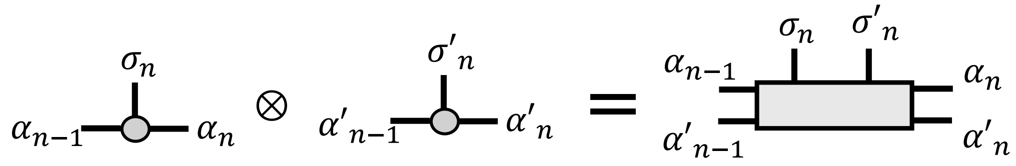

FIGURE 3.7: **Diagrammatic representation of a single site in a matrix product density operator (MPDO)**. Diagram representation of the contraction of same site tensors of two copies of an arbitrary MPS $|\psi\rangle = |\psi'\rangle$, written as a single rank six tensor element of the corresponding MPDO $\hat{\rho} = |\psi\rangle\langle\psi|$ [156].

representing the thermal density matrix $\rho = e^{-\beta H}$ as a purified state by evolving an initial infinite-temperature state in imaginary time using the TDVP algorithm discussed in Section 3.2.5. This approach allows for efficient computation of thermal expectation values and correlation functions, providing deep insights into quantum phase transitions, transport properties, and thermalization dynamics in strongly correlated systems.

3.3.1 Matrix product density operators

While time evolution for MPS is typically defined in terms of pure states, the algorithm can be extended to mixed states. The way this is done is by introducing the MPDO [180], which, unlike a pure state density matrix $\hat{\rho} = |\psi\rangle\langle\psi|$, can represent a general statistical ensemble. We define the MPDO as a set of tensors where each site carries two physical indices (bra and ket). The full MPDO can be written as

$$\hat{\rho} = \sum_{\sigma,\sigma'} \sum_{\substack{a_1 \cdots a_N \\ a'_1 \cdots a'_N}} M^{\sigma_1 \sigma'_1}_{1,1',a_1,a'_1} \cdots M^{\sigma_N \sigma'_N}_{a_{N-1},a'_{N-1},N,N'} |\sigma_1, \cdots, \sigma_N\rangle\langle\sigma'_1, \cdots, \sigma'_N|. \tag{3.29}$$

Here, for every individual site k, a given MPDO matrix coefficient $M^{\sigma_k \sigma'_k}_{a_{k-1},a'_{k-1},a_k,a'_k}$ has a dimension $d_k \times d_k$ and, to ensure the state is mixed and positive semi-definite, can be decomposed into

$$M^{\sigma_k \sigma'_k}_{a_{k-1},a'_{k-1},a_k,a'_k} = \sum_{w_k} A^{\sigma_k,w_k}_{a_{k-1},a_k} \times (A^{\sigma'_k,w_k}_{a'_{k-1},a'_k})^*, \tag{3.30}$$

where w_k is the ‘purification index’ (or Kraus index). The presence of this index allows the MPDO to represent a state with a rank higher than 1; specifically, the state is pure only if the dimension of w_k is 1 for all sites. Here, the matrices $A^{\sigma_n}_{a_n a_{n+1}}$ are also seen in Eq. (3.8) as the building blocks of the original MPS. The maximum dimension of the Hilbert space at a given site d_n is $D_n \times D_{n+1}$, the product of the maximum bond dimensions of the site and its adjacent site. The larger the bond dimension D for these tensors the larger the entanglement that can be represented within the given Hilbert space. This method can be used to represent both mixed and pure states, and expectation values can be determined simply by

$$\langle O\rangle_\rho = \mathrm{Tr}\big(\hat{O}\sum_{\sigma\sigma'}\sum_{\substack{a_1\cdots a_N\\ a'_1\cdots a'_{N-1}}} M^{\sigma_n\sigma'_n}_{a_{n-1},a_n,a'_{n-1},a'_n}|\sigma_1,\cdots,\sigma_N\rangle\langle\sigma'_1,\cdots,\sigma'_N|\big). \tag{3.31}$$

There are also different ways in measuring error between two MPDOs. For example one can observe fidelity using $F(\rho,\rho') = \mathrm{Tr}(\rho\rho')$, as well as the maximal overlap between all possible purifications of ρ and ρ', given by $P(\rho,\rho') = \mathrm{Tr}(\sqrt{\sqrt{\rho}\rho'\sqrt{\rho}})$. Figure 3.7 provides a diagrammatic representation of the single site tensor of an arbitrary MPDO.

3.3.2 Density matrix purification

Having defined MPDO that can represent both mixed and pure states, the next step is to be able to ‘purify’ the MPDO such that we end up with a pure state on which standard time evolution methods can be applied. The way to achieve this is to express the MPDO in terms of a pure MPS defined over a larger Hilbert space. It suffices to double the physical Hilbert space $\mathsf{H}_{\mathsf{phys}} \to \mathsf{H}_{\mathsf{phys}} \otimes \mathsf{H}_{\mathsf{phys}} = \mathsf{P}$. Thus, the MPDO acting on the physical space becomes a pure state in the doubled space of physical and virtual ancilla sites, giving the procedure the name purification. In order to obtain single-site tensors for the new purified state the six bond indices depicted in figure 3.7 will have to be combined into three bond indices by renaming

$(a_{n-1}, a'_{n-1}) \rightarrow b_{n-1}$ and $(a_n, a'_n) \rightarrow b_n$. Hence,

$$\hat{\rho} = \sum_{\sigma\sigma'} \sum_{\substack{a1 \ldots a_N \\ a'_1 \ldots a'_{N-1}}} M^{\sigma_1\sigma'_1}_{1,1',a_1,a'_1} \cdots M^{\sigma_N\sigma'_N}_{a_N a'_N 11'} |\sigma_1 \cdots \sigma_N\rangle\langle\sigma'_1 \cdots \sigma'_N| \rightarrow$$

$$|\hat{\rho}\rangle\rangle = \sum_{\substack{\sigma_1 \cdots \sigma_N \\ \sigma'_1 \cdots \sigma'_N}} \sum_{\substack{b_1 \ldots b_N \\ b'_1 \ldots b'_{N-1}}} M^{\sigma_1}_{1,b_1} M^{\sigma'_1}_{b_1,b'_1} \cdots M^{\sigma_N}_{b'_{N-1},b_N} M^{\sigma'_N}_{b_N,1} |\sigma_1\sigma'_1\sigma_2\sigma'_2 \cdots \sigma_N\sigma'_N\rangle\rangle_P. \quad (3.32)$$

The result is a purified state defined on a doubled state space $|\hat{\rho}\rangle\rangle$ made up of physical sites σ_k and ancilla sites σ'_k. Note that the original density matrix can always be recovered by tracing out the auxiliary space $\hat{\rho} = Tr|\hat{\rho}\rangle\rangle\langle\langle\hat{\rho}|$. Diagrammatically we can describe the purification as

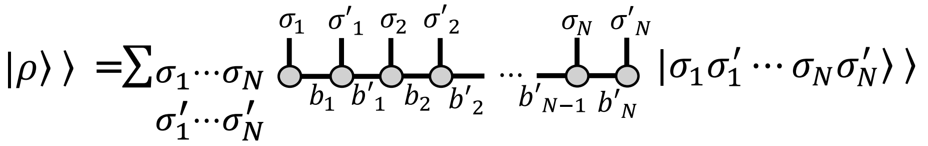

FIGURE 3.8: **Diagrammatic representation of a purified MPDO, defined on a doubled state space MPS of physical and ancilla sites** [156]

.

The bond dimension is heavily affected by state purification, with the doubling of the Hilbert space leading to exponential growth in bond dimension $D \rightarrow D^2$ for the index set $\{b'_n\}$ and the SVD without compression causes further increase dD^2. In order to keep the original specified bond dimension D, the purification needs to be truncated and the spectrum of SVD in the second step needs to be truncated after the D largest singular values. This resulting trade-off makes strongly entangled states difficult to purify. Either the need for computational resources increases quadratically or the accuracy, measured by the truncation weight, becomes significantly worse.

3.3.3 Thermal state calculation

The main goal of finite temperature calculations is to numerically evaluate thermodynamic properties of a quantum system at a given energy. In practice this amounts to accurate approximation of a thermal state at a given energy, comparing it to a system at the same energy in order to gauge the level of thermalization for various observables. For a system with a Hamiltonian H, the thermal state must be approximated as an MPDO $\hat{\rho}_\beta \propto e^{-\beta H}$, where $\beta = 1/T$ is the thermodynamic temperature of the system. To achieve this, we will first define an infinite-temperature maximally mixed MPDO $\hat{\rho}_0$, which is simply the identity operator $\hat{I}_{ph}$ in the physical Hilbert space $\mathsf{H}_{\mathsf{phys}}$. The MPDO $\hat{\rho}_\beta$ representing a thermal equilibrium state at arbitrary temperature β can be expressed as

$$\hat{\rho}_\beta = Z(\beta)^{-1} e^{-\frac{\beta H}{2}} \hat{\rho}_0 e^{-\frac{\beta H}{2}}. \tag{3.33}$$

Here, $Z(\beta) = Tr\big[e^{-\beta H}\big]$ is the partition function, and the operator $e^{-\frac{\beta H}{2}}$ can be reached by successive application of

$$e^{-\beta H} = (e^{-\frac{\Delta\beta H}{2}})^S \hat{\boldsymbol{I}} (e^{-\frac{\Delta\beta H}{2}})^S, \tag{3.34}$$

which we interpret as an imaginary time evolution with S smaller steps of $\Delta\beta$.

Since the Hamiltonian of interest in this thesis has long range interaction, imaginary time evolution must be implemented using the TDVP algorithm (see Section 3.2.5). The method is only defined in terms of an MPS and so it is necessary to turn our initial infinite temperature MPDO into a MPS by purification $\hat{\rho}_0 \to |\rho_0\rangle$ shown in Eq. (3.32). After this we simply apply the imaginary time evolution onto $|\rho_0\rangle$ in the doubled Hilbert space using TDVP algorithm to evolve to $|\rho_\beta\rangle$ using the small temperature step $\Delta\beta$,

$$|\rho_{(0+\Delta\beta)}\rangle\rangle = e^{-\frac{\Delta\beta}{2}(H\otimes\mathbb{I}+\mathbb{I}\otimes H^T)}|\rho_0\rangle\rangle \to |\rho_\beta\rangle\rangle = \left(e^{-\beta H/2} \otimes e^{-\beta H^T/2}\right)|\rho_0\rangle\rangle, \tag{3.35}$$

where the original Hamiltonian H is applied to physical sites, and H^T is applied to ancilla sites. The energy of the evolved state is tested throughout this imaginary time evolution to monitor if the target energy for a given β has been reached. Also note that the TDVP method requires two full sweeps along the chain to complete a single evolution step, and so the implied factor of $\frac{1}{2}$ is added to the desired time step to ensure correct imaginary time step size for the physical sites. Once the evolution has reached $|\psi_\beta\rangle$, thermal expectation values can be calculated directly in doubled space using

$$\langle \hat{O} \rangle_\beta = (Z(0)/Z(\beta))\langle \rho_\beta | \hat{O} | \rho_\beta \rangle, \tag{3.36}$$

where $Z(0) = d^N$, and the normalization factor $(Z(0)/Z(\beta))$ can be derived from the expectation value of the identity operator in the doubled Hilbert space

$$1 = \langle \hat{\boldsymbol{I}}_{\mathsf{H}_{\mathsf{phys}} \otimes \mathsf{H}_{\mathsf{phys}}} \rangle = \mathrm{Tr}[\hat{\rho}_\beta]_{\mathsf{H}_{\mathsf{phys}}} = (Z(0)/Z(\beta))\mathrm{Tr}\big[|\rho_\beta\rangle\langle\rho_\beta|\big] = (Z(0)/Z(\beta))\langle \rho_\beta | \rho_\beta \rangle,$$

$$\frac{1}{(Z(0)/Z(\beta))} = \langle \rho_\beta | \rho_\beta \rangle. \tag{3.37}$$

Thus any given operator can be evaluated simply by

$$\langle \hat{O} \rangle_\beta = \frac{\langle \rho_\beta | \hat{O} | \rho_\beta \rangle}{\langle \rho_\beta | \rho_\beta \rangle}. \tag{3.38}$$

The only difficulty is numerical, as the calculations must be performed in a doubled Hilbert space after the infinite temperature MPDO is purified. Given that imaginary time evolution operator is Hermitian, but not unitary, the state must be normalized after every step of the evolution. We can always recover $Z(\beta)$ by rearranging Eq. (3.37), allowing for the calculation of the thermodynamic constants $U(\beta) = \langle \hat{H} \rangle_\beta$, $F(\beta) = -\beta^{-1} \ln Z(\beta)$ and thus $S(\beta) = \beta(U(\beta) - F(\beta))$. The general procedure for the thermal state approximation thus takes the form:

1. **Write down the purified MPS**

   The first step in the calculation is to reformulate the infinite temperature temperature density operator as a purified MPS in doubled Hilbert space. An infinite temperature MPDO ,$\hat{\rho}_0$, for a Rydberg chain of length N can be factorized at every site [152] giving

   $$\hat{\rho}_0 = \frac{1}{d^N} \hat{\boldsymbol{I}} = \frac{1}{d} (\hat{\boldsymbol{I}})^{\otimes N}.$$

   This allows us to purify the mixed MPDO on each individual site independently, resulting in N physical-ancilla pairs of pure states that can then simply be multiplied to build up the final infinite temperature MPS in doubled Hilbert space $|\rho_0\rangle = |\rho_0\rangle_1 |\rho_0\rangle_2 |\rho_0\rangle_3 \cdots |\rho_0\rangle_N$.

   To define a purified state on the i^{th} site $|\rho_0\rangle_i$ we use the fact that the partial trace of a maximally entangled state is a maximally mixed state. Thus the maximally mixed identity operator for the infinite temperature MPDO for site i can be thought of as the partial trace over a maximally entangled pure state in the physical-ancilla space. Any of the Bell states satisfy this constraint, and for our purposes it will suffice to choose the singlet state

$$|\rho_0\rangle_i = \frac{1}{\sqrt{2}}\big[|1_{p_i}0_{a_i}\rangle - |0_{p_i}1_{a_i}\rangle\big], \tag{3.39}$$

where the numbers $1, 0$ signify spin up and spin down respectively, and the indices p_i, a_i signify the i^{th} physical and auxiliary site. It is straighforward to check that the original density operator can be recovered using

$$\begin{aligned}
\hat{\rho}_{pa} &= \frac{1}{2}\big[|1_{p_i}0_{a_i}\rangle\langle 1_{p_i}0_{a_i}| - |1_{p_i}0_{a_i}\rangle\langle 0_{p_i}1_{a_i}| - |0_{p_i}1_{a_i}\rangle\langle 1_{p_i}0_{a_i}| + |0_{p_i}1_{a_i}\rangle\langle 0_{p_i}1_{a_i}|\big], \\
\mathrm{Tr}_a[\rho_{pa}] &= \frac{1}{2}\big[(\hat{\boldsymbol{I}}_p \otimes \langle 0_{a_i}|)\hat{\rho}_{pa}(\hat{\boldsymbol{I}}_p \otimes |0_{a_i}\rangle) + (\hat{\boldsymbol{I}}_p \otimes \langle 1_{a_i}|)\hat{\rho}_{pa}(\hat{\boldsymbol{I}}_p \otimes |1_{a_i}\rangle)\big], \\
&= \frac{1}{2}\big[|0_{p_i}\rangle\langle 0_{p_i}| + |1_{p_i}\rangle\langle 1_{p_i}|\big].
\end{aligned}$$

Therefore, in the case of spin chains, we can define the infinite temperature purified MPS as a product state of N physical-ancilla singlet state pairs. This simplifies the first step by avoiding manual purification to the initial identity matrix, but does not generally apply in quantum systems.

2. **Applying time evolution**
   The purified infinite temperature MPS $|\rho_0\rangle$ is treated as a standard MPS when applying time evolution $|\rho_{(0+\Delta\beta)}\rangle = \exp\big[-\frac{\Delta\beta}{2}(H \otimes \mathbb{I} + \mathbb{I} \otimes H^T)\big]|\rho_0\rangle$ in steps of $\Delta\beta$. Make sure to normalize the state after every evolution step. In the case of long ranged interactions choose the TDVP method for time evolution as detailed in Section 3.2.5.

3. **Evaluating energy**
   Throughout the time evolution it will be necessary to monitor the energy of the evolved thermal state and compare it to the final energy of our prepared system. This can be done by evaluating $\langle\rho_\beta|\hat{H}_D|\rho_\beta\rangle$ as described in Eq. (3.38), where $H_D = H \otimes \mathbb{I} + \mathbb{I} \otimes H^T$ is the doubled Hilbert space Hamiltonian and β is the thermodynamic temperature of the evolved state. If the energies agree within the desired tolerance, we use our evolved state as a new thermal state.

Given that we are evolving downward from the infinite temperature state, the total evolution time is unclear and strongly dependent on the size of the time step, the size of the system, and the magnitude of the final β. If the system size is too big, the doubled Hilbert space time evolutions will take a long time, especially for a small time step. Likewise, if the target β is too close to the ground state energy, then integrating along the Boltzmann distribution will take exponentially more time steps. To mitigate these challenges, implementation of a variable time step scheme is advised, with an adaptive step $\Delta\beta$ based on the norm of the energy gradient $|\nabla E|$ that slows down when energy changes for every time step are too large and stops when they become too small, along with a fixed thresholding scheme that progressively reduces β as it approaches the target energy up to a predefined error tolerance.

Once the evolved state $|\rho_\beta\rangle$ reaches an energy that is equivalent (up to an error tolerance) to that of the system being studied, we have attained an approximation of the theoretical β that corresponds to that system being it thermal equilibrium. Thermalization in the system can be evaluated by comparing both the overlap of the evolved thermal state with the target state of the studied system, as well as comparing the difference between evaluating expectation values of different observables.

3.4 Summary

In Chapter 3 we introduced the tensor network formalism as powerful modern tool for numerical simulation of quantum systems. In particular, Section 3.2 introduces the concept of a matrix product state (MPS), in which the exponentially large matrix of wavefunction coefficients of a quantum state is factorized into a chain of lower-rank tensors. We discuss how the controlled truncation of such an MPS results in a numerically efficient approximation that can be used for simulating real one-dimensional systems. A graphical representation of the MPS is also provided in Section 3.2.1, improving the readability of tensor network calculations. Section 3.2.2 builds on this understanding by introducing the canonical form of the MPS which implements an orthonormality constraint on the bonds in the tensor chain to further improve the efficiency of MPS calculations, while Section 3.2.3 discusses matrix product operators (MPO) the tensor network equivalent of quantum operators. Both the canonical form of the MPS and the MPDO play a critical role in the time evolution algorithms for MPS, which are first discussed broadly in Section 3.2.4, before the focus is turned to the Time-Dependent Variational Principle

(TDVP) in Section 3.2.5 as the most suitable method for simulating time evolution for a system with long-range interactions like the chain of Rydberg atoms in this thesis.

In addition, Section 3.3 provides all the necessary tools to perform finite temperature calculations in the tensor network formalism. In Section 3.3.1 we introduce the concept of matrix product density operators (MPDO), as rank six tensors which is the outer product of the bra and ket of an MPS, while Section 3.3.2 provides a method of writing an infinite temperature MPDO in 'purified' form as an MPS in a doubled Hilbert space such that standard time evolution algorithms can be applied to it. Finally, Section 3.3.3 implements imaginary time evolution on the purified infinite temperature MPDO, providing a straightforward algorithm to evolve the state from an infinite temperature to a target temperature that matches the energy of a system of interest, thus approximating a thermal state that can be used for comparison. This algorithm will play a central role when evaluating thermalization in Chapter 5.

Chapter 4

Phase noise in adiabatic state preparation

Adiabatic state preparation can suffer considerable effects from laser phase noise because it inherently depends on the precise control and tuning of laser parameters over an extended period [38, 116, 118, 119]. Unlike sudden quenches or direct excitations, which introduce high-energy perturbations, adiabatic ramps are also sensitive to slow, cumulative errors. This makes adiabatic protocols an ideal testbed for investigating the long-term impact of phase noise on quantum evolution. As the system follows a trajectory through parameter space, phase noise acts as a time-dependent perturbation which causes excitation to higher energies which over time destroy the adiabatic preparation. Since the energy structure of the system evolves dynamically, different stages of a given ramp have varying responses to the same phase noise, providing insight into the interplay between noise-driven excitations and the underlying structure of the many-body Hamiltonian. In addition, the adiabatic framework enables systematic exploration of how different noise characteristics, such as spectral content and strength, affect excitation dynamics. By tuning the ramp duration, transverse field strength, and detuning, it becomes possible to probe regimes where phase noise leads to significant excitation or, conversely, where its impact is suppressed. Additionally, adiabatic state preparation offers a natural setting to investigate whether noise-driven excitations result in thermalization and how deviations from thermal predictions arise due to integrability constraints or specific noise features as will be discussed in the following chapter. These factors make adiabatic protocols not only practical tools for generating complex quantum states but also powerful probes of decoherence in many-body quantum systems.

The central findings in this thesis involve the simulation of a ground state adiabatic preparation of a one dimensional Rydberg spin chain, a closed system in which the effects of phase noise on system dynamics can be tested in isolation. The Rydberg spin chain implements the long-range transverse field Ising model (TFIM), a well-studied many-body model that leads to the formation of crystalline ground states in which an increasing number of evenly spaced excitations is favored in different Hamiltonian parameter sectors [41, 42, 59, 114, 182]. These crystalline ground states occur in the TFIM at a variety of parameter regimes, are robust against small changes in the transverse field, and can be prepared adiabatically by tuning the laser parameters in the Hamiltonian. The adiabatic theorem given in Appendix B provides the tools necessary to traverse the Hamiltonian parameter space and construct the linear adiabatic ramps discussed in this chapter, that allow for the adiabatic preparation of crystalline ground states. Although more efficient adiabatic experiments using ramps tailored to reduce timescales while maintaining fidelity have since been proposed [20, 183] and even experimentally demonstrated [59], the relatively simple architecture with linear adiabatic ramps and stronger long-range interactions discussed here is more conducive to the study of laser phase noise effects themselves (as opposed to their interplay with a particular optimized ramp), which is the main focus of this chapter.

The chapter is laid out as follows: after a brief introduction to the TFIM we discuss how the competition in the Hamiltonian parameters gives rise to the previously mentioned Rydberg crystals, the ground states that occur in specific parameter regimes and exhibit long range ordering. Building on this understanding, the subsequent sections of the chapter lay out a three-stage adiabatic state preparation first introduced in [114], which was devised to prepare the antiferromagnetic (Z_2) ordering along the spin chain. We analyze the performance and behavior of this adiabatic state preparation using numerical exact diagonalization tools. Continuing on, the second half of this chapter introduces laser phase noise into the TFIM, providing an in-depth analysis of the impact that phase noise has on the final fidelity of the prepared state for a variety of adiabatic ramp lengths, and phase noise profiles. Finally, we probe the behavior of phase noise in a TFIM system by analyzing the excitation dynamics in the energy spectrum. We do this by analyzing excitation spectra of Rydberg spin chains after a time-independent evolution of the ground state, followed by a discussion of the dominant matrix elements that describe the available energy transitions that can be excited with a given noise source, giving us a broad picture of the different mechanisms that influence dephasing at different stages along the adiabatic ramp.

4.1 The long-range transverse-field Ising Hamiltonian

The TFIM naturally maps to Rydberg atom systems because of the inherent structure of Rydberg interactions. By tuning the Rabi frequency and detuning, the competition between interaction-induced spin order and quantum fluctuations can be precisely controlled, making Rydberg arrays an ideal platform for simulating quantum magnetism and nonequilibrium dynamics in the TFIM. Due to this mapping, the past decade has seen extensive research in the Rydberg generated TFIM [49, 96, 184, 185] and its many interesting features.

All simulations discussed in this thesis will be carried out in a one-dimensional Rydberg spin Hamiltonian that takes the form

$$H_R = \frac{\Omega(t)}{2}\sum_{k}^{N}\hat{\sigma}^x - \delta(t)\sum_{k}^{N}\hat{n}_k + V_{dd}\sum_{k,l>k}^{N}\frac{\hat{n}_k\hat{n}_l}{|k-l|^3}, \tag{4.1}$$

where the first term is the transverse field that drives the transitions in the system at a Rabi frequency $\Omega(t)$, and the second term incorporates laser detuning with the prefactor $\delta(t)$ mediated by the number operator $\hat{n}_k \equiv \sigma_z^k - \hat{I}$. The terms $\delta(t)$ and $\Omega(t)$ are governed solely by the laser, and are tuneable in an experimental setting. Finally, we introduce long-range interactions scaled by interaction strength V_{dd} that enforce a Rydberg interaction penalty on neighboring excitations. We work in the dipole-dipole interaction regime in which Rydberg states must maintain a permanent dipole moment that is typically achieved through strong electric fields [186–188], and long range interactions decay as a function of distance between sites $d^3 = |k-l|^3$, where k and l are site indices, and the lattice constant is absorbed into V_{dd}. To emphasize long-range interactions, we have chosen to work in the dipole-dipole regime with cubic interaction decay as opposed to the Van Der Waals regime with d^{-6} decay. Although the Van der Waals regime is usually easier to realize experimentally as there is no need to engineer Förster resonances between atoms [189, 190], both regimes are accessible in modern systems [49] and have pros and cons that enable the study of different physics [49–53, 98, 191]. For computational simplicity, we define all Hamiltonian parameters in units of interaction strength which for the purpose of this chapter will be kept at an experimentally realizable value of $V_{dd}/2\pi = 10\text{MHz}$, with $\hbar = 1$ also assumed. This means that both Ω and δ are expressed in units of V_{dd}, while time is given in units of $1/V_{dd}$. In the following section, we show how the competition between these three Hamiltonian terms gives rise to ground states with crystalline ordering of Rydberg excitations along the one-dimensional chain.

4.1.1 Crystalline ground states

Crystalline ground states have been of particular interest in many-body physics communities over the past decade [192], describing phases of matter that exhibit self-order into rigid structures that are robust to small changes in the Hamiltonian. In the case of trapped Rydberg atom arrays described in Eq. (4.1) with no transverse field ($\Omega = 0$), such crystalline states arise naturally as the lowest energy eigenstates, as a result of the competition between laser detuning δ and the interactions V_{dd}. Figure 4.1(a) provides a schematic diagram of this competition for a one-dimensional array of atoms in optical tweezer arrays. In the absence of a transverse field ($\Omega = 0$), if a far red-detuned ($\delta < 0$) laser illuminates the array there is little energy transferred into the system, and the ground state has no excitations along the array. However, the energy in the system increases as δ is tuned up and the laser becomes blue-detuned ($\delta > 0$) and gradually begins to overcome the dipole-dipole blockade, making excitation more energetically favorable. This leads to an excitation ladder in the ground state as it transitions from having no Rydberg excitations to having incrementally increasing excitations. One can go up and down this excitation ladder simply by changing δ, as excitations arrange themselves uniformly to satisfy the dipole-dipole blockade as much as possible and thus balance the energy in the system. Since their prediction, such crystalline ground states have been studied theoretically [20, 114] and also observed experimentally [42, 59].

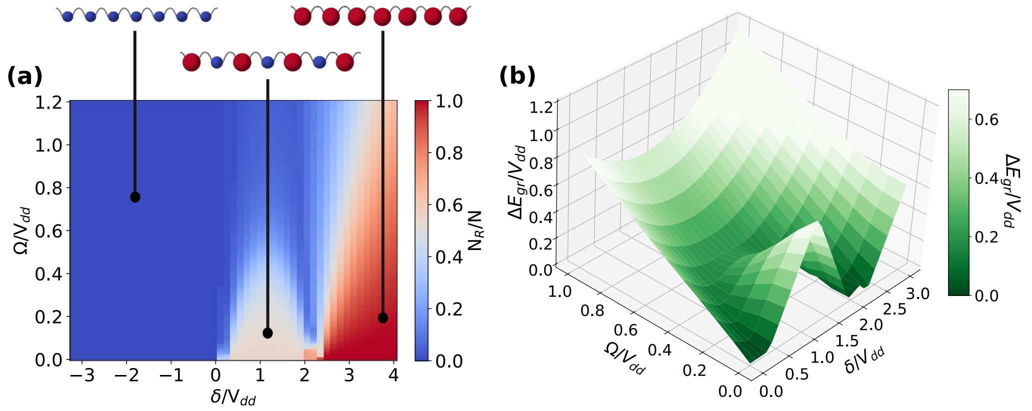

FIGURE 4.1: **Crystalline ground states and ground state energy gap in a one dimensional Rydberg spin chain.** **(a)** Fraction of Rydberg excitations along the spin chain N_R/N on a laser parameter surface plot Ω/δ. Also provided are diagrammatic representations of three regions with stable number of Rydberg excitations.The central lobe with excitation fraction $N_R/N = 0.5$ corresponds to the Z_2 crystalline state, which forms for $\delta/V_{dd} \in [0, 2]$, and is robust against small increases of transverse field up to $\Omega/V_{dd} \approx 0.4$. **(b)** Surface plot ground state energy gap ΔE_{gr} in the parameter region of the Z_2 crystalline state with green to white color gradient.

A given crystalline ground state remains energetically favorable even after quantum superpositions are introduced by increasing the transverse field, leading to entire regions in the δ/Ω parameter space where only a single crystalline state is represented in the ground state. Figure 4.1(a) provides the fraction of Rydberg excitations along chain N_R/N in a parameter space plot δ/Ω, clearly showing the formation of regions with a uniform number of Rydberg excitation. In the case of the dipole-dipole interaction regime of Eq. (4.1), two distinct lobes remain stable in non-zero Ω regions; one with a fraction of total Rydberg excitations $\mathrm{N}_R/\mathrm{N} = 0.5$, arranged in an antiferromagnetic (Z_2) ordering along the chain; and one that is filled with Rydberg excitations. If $\delta \gg 0$ is much larger than the dipole-dipole interaction V_{dd} then the off-resonance shift that Rydberg atoms impose on neighboring sites is overcome, and the most energetically favorable state is one fully filled with Rydberg excitations as seen in the high δ region of Figure 4.1. The fragility of these ground states is heavily dependent on the ground state energy gap ΔE_{gr}, with a larger energy gap providing insulation from unwanted excitations when such states are being prepared. Figure 4.1(b) provides insight on ΔE in the region of the Z_2 ordered crystalline state in the form of a surface plot on the same laser parameters. We observe that the Z_2 ordered crystalline region is surrounded by a ring of low ΔE, which then begins to rise towards the center of the lobe. Care must be taken in any potential preparation of such states that involves the tuning of laser parameters, as such experiments may suffer fidelity loss when crossing regimes with ΔE that is too low.

It is also important to discuss the boundary conditions when performing numerical simulations of the Hamiltonian in Eq. (4.1). For open boundary conditions, atoms found on the edges of the chain experience less of the effect of Rydberg interactions and are therefore more likely to achieve Rydberg excitation than atoms within the chain. This means that energetically favorable Z_2 ordering of Rydberg excitations can be arranged in chains with odd number of lattice sites, but even number of lattice sites incur a central domain wall after which ordering flips [41]. Ground states with such a central domain are no longer represented by a single maximally ordered state Z_2, but rather a superposition of states with opposite orientations. Hence, for clarity of the main elements of laser phase noise, we will omit discussion of even chains where the ground state becomes a more complicated superposition of degenerate states. Instead, the following sections describe a three-stage adiabatic process that takes a Rydberg spin array with an odd number of atoms and a ground state with no Rydberg excitations to one with a Z_2 ordered spin alignment that has both outer sites excited to the Rydberg state.

4.2 Adiabatic state preparation in the TFIM

In the Hamiltonian defined in Eq. (4.1), the transverse drive, $\Omega(t)$, induces Rydberg excitation, while the detuning, $\delta(t)$, controls the interaction-induced effective energy landscape. By starting from a far-detuned, weakly driven regime and adiabatically tuning both Ω and δ independently, the system can remain in the ground state while being guided from a phase with no Rydberg excitations into a crystalline Z_2 phase, where Rydberg excitations are arranged in an alternating pattern due to interactions. Numerical simulations of this adiabatic transition to the Z_2 phase space, where the competition between the drive and interactions can be systematically adjusted, provide a well-controlled testbed for studying the effects of phase noise.

The exact adiabatic protocol we will follow was first proposed in [114], and has also been designed for the one-dimensional Rydberg spin Hamiltonian in the dipole-dipole regime. The protocol consists of three linear ramps that tune Ω and δ

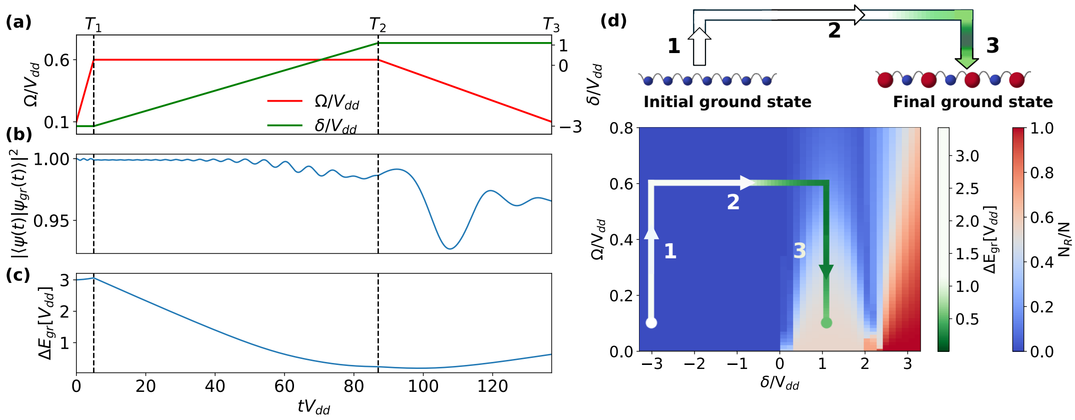

FIGURE 4.2: **Three-stage adiabatic preparation of a Z_2 ordered crystalline state.** **(a)** Hamiltonian parameters for three stage adiabatic state preparation of a Z_2 ordered crystalline state for a 11 atom Rydberg chain. Parameter Ω (red) is tuned linearly in stages 1 and 3 for periods T_1 and T_3, while δ (green) is tuned linearly only in stage 2 for a period of T_2. **(b)** Concurrent fidelity measured as overlap between the ground state $|\psi_{gr}\rangle$ of the instantaneous Hamiltonian $\hat{H}_R(t)$ and the evolved state $|\psi\rangle$. **(c)** Energy gap ΔE_{gr} between the instantaneous ground state and the first excited state. **(d)** Parameter space plot from Figure 4.1 with added adiabatic ramps. Also shown is a schematic diagram of crystalline ordering of excited (red) and non-excited (blue) atoms for initial and target many-body state. The path for the three-stage adiabatic state preparation studied is shown with color gradient from white to green tracking ΔE_{gr}. All parameters are provided in units of interaction strength V_{dd}.

independently. The goal of the procedure is to take a ground state with no Rydberg excitations to a ground state with Z_2 ordered Rydberg excitations, while maximizing the ground state energy gap, ΔE_{gr}, throughout most of the protocol to mitigate diabatic excitation out of the ground state. The initial Hamiltonian chosen is thus far detuned at laser parameters $\Omega/V_{dd} = 0.1$ and $\delta/V_{dd} = -3$, where a non-interacting ground state can be prepared experimentally by optical pumping. The target Hamiltonian occurs at $\Omega/V_{dd} = 0.1$ and $\delta/V_{dd} = 1.1$ with a much smaller ΔE_{gr} and a ground state with Z_2 excitation ordering. We choose to start and finish at $\Omega/V_{dd} = 0.1$ as opposed to $\Omega/V_{dd} = 0$ to ensure that the many-body ground state is well-defined throughout the protocol by avoiding degeneracies.

Figure 4.2 sketches out how this three-stage adiabatic state preparation looks in practice. Figure 4.2(a) provides a sketch of typical values for $\Omega(t)$ and $\delta(t)$ at the three different stages of preparation, with the system reaching a maximum Rabi frequency of $\Omega/V_{dd} = 0.6$, and with independent parameter variation rates during each stage. The adiabatic protocol is also projected onto the Ω/δ parameter plot in Figure 4.2(e) to illustrate the path taken from the initial ground state without Rydberg excitations to the target ground state with Z_2 ordering. Figures 4.2(b,c) show the concurrent changes in ΔE_{gr} and ground-state fidelity after a simulation of such an adiabatic state preparation for an 11 atom chain. Since the evolution time is finite and thus not perfectly adiabatic, there is a small amount of excitation away from the ground state and into higher-energy states throughout the process leading to a drop in the overall fidelity. At the end of stage 2 and beginning of stage 3 of the protocol there is a critical region where ΔE_{gr} decreases making excitation of higher energy many-body states and a drop in fidelity more probable. Most diabatic excitations occur around this parameter region, with some fidelity recovering towards the end of stage 3 as the ground state energy gap increases once again. In the next sections, we will probe this loss in fidelity for different variation rates to get a more complete understanding of the behavior of our system before adding and studying laser phase noise.

4.2.1 Energy gap and the variation rate

Unwanted excitations out of the ground state in adiabatic state preparations occur mainly due to violations of the adiabatic constraint which is provided in Appendix B, Eq. (B.11). If the variation rate of a given Hamiltonian parameter is large in comparison with the instantaneous ΔE_{gr}, the system can undergo diabatic transitions as some of the population in the ground state becomes correlated with the first few excited states, leading to oscillation. If not kept under control, over time such transitions cause loss of ground-state occupancy and an overall drop in fidelity. Combating this diabatic loss of fidelity can only be achieved by a decrease in the variation rate of laser parameters in the critical regions of the ramp.

This dependence between diabatic excitation and the parameter variation rate can be observed directly in the case of the three-stage adiabatic ramp discussed in Figure 4.2(a–c), where different variation rates correspond to distinct evolution times T_1, T_2, and T_3. For stage 1 of the protocol, the evolution time is $T_1 V_{dd} = 9$, and due to the large ground-state energy gap in this far-detuned regime, even such a short evolution time is sufficient to preserve 99.8% fidelity. However, it is evident from Figure 4.2(c) that the most critical region with the smallest energy gap begins at the end of stage 2 and is most dramatic in the first half of stage 3, resulting in increased oscillations in fidelity seen in Figure 4.2(b) as diabatic excitation populates the higher-energy states. Stage 2, with an evolution time of $T_2 V_{dd} = 82$, spans the parameter regime where the detuning is swept across

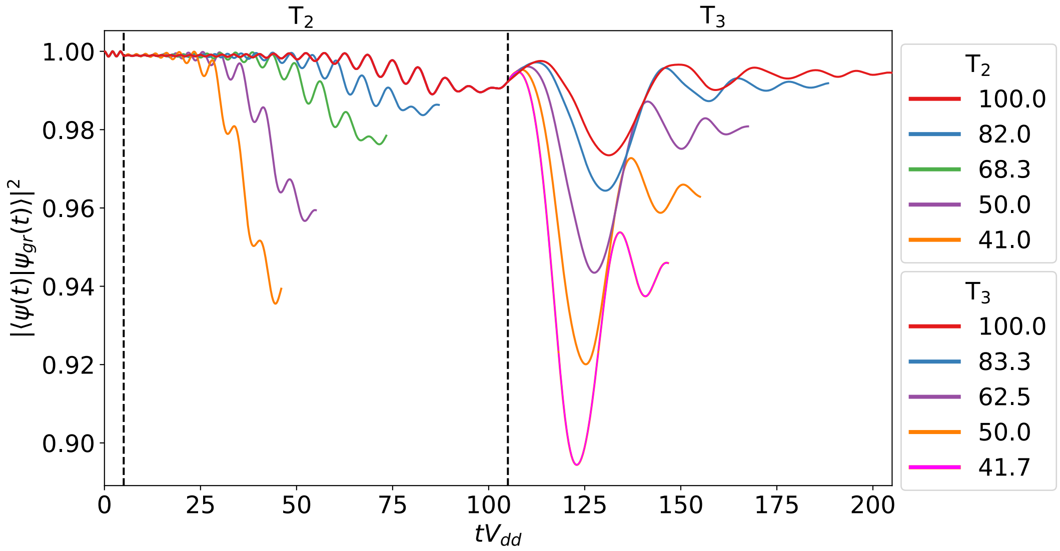

FIGURE 4.3: **Fidelity comparison for different variation rates for stages 2 and 3 of adiabatic state preparation**. Ground state fidelity during an adiabatic preparation of the Z_2 ordered state in an 11 site spin chain introduced in Figure 4.2, with time and laser parameters scaled by interaction strength V_{dd}. Stage 1 preserves high fidelity at an evolution time $T_1 = 5$ and is kept constant. Each colored line represents a different total evolution time for stage 2 (T_2) and stage 3 (T_3) of the protocol, corresponding to a different variation rate $\Delta\delta/\Delta t V_{dd}^2$ across the change in laser detuning $\Delta\delta/V_{dd} = 4.1$ in stage 2, and a variation rate $\Delta\Omega/\ tV_{dd}^2$ across a total change in Rabi frequency of $\Delta\Omega/V_{dd} = -0.5$ in stage 3. A given variation rate is calculated by dividing the total change in Ω across the entire ramp of $\Delta\Omega_{T_3}/V_{dd} = 0.45$, by the total ramp time.

resonance, leading to a moderate drop in fidelity to 98.7%. The lowest energy gap occurs during stage 3, which has a total evolution time of $T_3V_{dd} = 50$. Despite this longer evolution time, the system experiences a more pronounced drop in fidelity followed by a partial recovery as the energy gap rises again, with the final fidelity stabilizing at 96.37%. It is thus crucial to understand how adjusting these evolution times impacts the adiabaticity and overall performance of the protocol.

Figure 4.3 shows the drop in ground-state fidelity when using different evolution times for stages 2 and 3 of the adiabatic protocol. In the case of stage 2, we observe a rapid degradation of fidelity as the evolution time is reduced below $T_2V_{dd} = 82$ (as seen in Figure 4.2(b)), since faster variation rates lead to larger violations of the adiabatic condition and make it increasingly difficult to maintain ground-state fidelity. A fidelity above 99% is achieved only when the evolution time is increased to $T_2V_{dd} = 100$. Similarly, varying the evolution time in stage 3 affects both the magnitude of the drop in fidelity when the minimum ground-state energy gap is crossed, and the system's ability to recover afterwards. Here, an evolution time of $T_3 V_{dd} = 100$ is required to provide sufficient diabatic suppression for the protocol to conclude above 99% fidelity. Given that this simulation is performed in an idealized closed system—where the loss of adiabaticity is the only source of error—the total run time of $T_{123} V_{dd} = 209$, corresponding to approximately 20.9 μs, remains relatively long compared to current experimental realizations [42, 59]. Modern implementations of such ramps often employ nonlinear ramp schemes [59] or counterdiabatic driving techniques [193] to further suppress diabatic excitations. Nevertheless, the adiabatic state preparation studied here serves as a controlled and relevant many-body benchmark for investigating the effects of laser phase noise in later sections. To isolate these effects and avoid unnecessary complexity, we continue to employ linear ramp protocols throughout this work.

4.3 Introducing phase noise to the TFIM

In Section 4.1, Eq. (4.1) we introduced the TFIM Hamiltonian for a one dimensional chain of Rydberg atoms, and used it in Section 4.2 to implement an adiabatic state preparation from a ground state with no Rydberg excitations along the chain, to one with an antiferromagnetic Rydberg excitation pattern (see Figure 4.2). This type of many-body experiment is heavily reliant on a stable and predictable laser drive, with detuning and Rabi frequency that can be dynamically tuned to mitigate unwanted diabatic excitation. However, what happens to such an experiment when the laser itself is noisy? The central findings of this thesis concern exposing this adiabatic state preparation to laser phase noise, measuring the effect such noise has on the fidelity of the final prepared state, as well as the nature of the induced excitation out of the ground state.

Adding laser phase noise onto the optical drive of the TFIM amounts to a small modification of the transverse field term in Eq. (4.1), which will now take the form

$$\begin{aligned}\hat{H}_R = \; & \frac{\Omega(t)}{2} \sum_{k}^{N} \left[e^{-i\phi(t)} |0\rangle_k \langle 1|_k + e^{i\phi(t)} |1\rangle_k \langle 0|_k \right] \\ & - \delta(t) \sum_{k}^{N} \hat{n}_k + V_{dd} \sum_{k,l>k}^{N} \frac{\hat{n}_k \hat{n}_l}{|k-l|^3},\end{aligned} \tag{4.2}$$

where the transverse field ,$\hat{\sigma}_x^k$, term has been written explicitly in terms of spin-up ,$|1\rangle_k$, (to signify a Rydberg excited atom) and spin-down ,$|0\rangle_k$, (to signify an atom in the ground state) transition elements of the ,k^{th}i, site, modulated by a phase term with a uniquely generated noise signal ,$\phi(t)$, (see Section 2.3), with the sign of the applied phase reversed for the two transition elements to preserve unitarity. Note that it is sometimes useful to work in the rotating frame in which phase noise appears not as a phase factor in the transverse drive, but rather as a stochastic term in detuning $\delta(t) \to \delta(t) - \dot{\phi}(t)$, where $\dot{\phi}(t)$ is the instantaneous change in frequency due to noise [194, 195]. We achieve this change of frames by applying the unitary transformation $\hat{U}_t = \exp(-i\phi(t)\sum \hat{n}_k)$, which is shown explicitly in Appendix C. Adding noise to the optical drive ,$\Omega(t)$, results in dephasing of the dynamics that accumulates and over time causes unwanted excitation out of the ground state. We continue to work in the dipole-dipole regime with open boundary conditions and cubic decay in long range interactions. Moreover, we once again scale dynamics by a relative interaction strength $V_{dd}/2\pi = 10$ MHz where we impose $\hbar = 1$. The choice allows us to study many-body dynamics in a parameter regime that is near to experimentally realized systems [59, 116], while still being in reasonable range with the peak frequencies of the used noise signal at 480kHz (see Figure 2.6).

In the context of adiabatic state preparation, where the dynamics are designed to follow a carefully controlled path through parameter space, the presence of dephasing noise can be particularly disruptive. Even if diabatic errors are suppressed by a sufficiently slow ramp, accumulated phase fluctuations can introduce latent energy into the system, driving excitation out of the ground state that does not respect the adiabatic trajectory. The severity of this impact depends not only on the noise strength but also on its spectral structure, its resonance with many-body energy gaps, and the integrability of the underlying Hamiltonian. The following sections will explore the impact of phase noise on adiabatic state preparation by evaluating final fidelity with the target ground state, as well as a deeper look into the nature of the excitation such noise induces by performing a matrix element analysis of the excitation spectrum. The generation of a realistic laser phase noise used in the following Sections was the main topic of Chapter 2, and the spectral profile used along with several example noise realizations can be found in Figure 2.6.

4.4 Effects of phase noise on fidelity

The first step in analyzing the impact of laser phase noise on adiabatic state preparation is to look directly at the performance of noisy preparation, by evaluating fidelity. To this end, the following section focuses on the effects of noise on the final prepared state after performing the adiabatic state preparation discussed in Figure 4.3, evaluating stages 2 and 3 independently. We analyze the energy of the prepared state along with its fidelity with the target Z_2 ordered ground state of the final Hamiltonian, repeating this analysis for different laser parameter variation rates, interaction strengths between sites, and noise strengths.

Figure 4.4 demonstrates the error caused by noise induced dephasing when measuring the fidelity of the final prepared state with the target Z_2 ordered ground state for stages 1 and 2 in plot (a), and separately for stage 3 in plot (c) of the adiabatic protocol. To generate data for stage 3 we use the prepared state at the end of stage 2 that corresponds to the highest fidelity. In addition, the energy of the final prepared state relative to the ground state is also provided, in (b) for stages 1 and 2, and in (d) for stage 3. Each data point in Figure 4.4 thus represents a final fidelity or energy, averaged across 100 independent noise realizations of adiabatic ramps simulated at a given variation rate and system size, with a black line showing an 11-site system with no laser phase noise for reference. Consistent with Figure 4.3, when no laser noise is present, we see continued improvement in fidelity as the evolution time increases and diabatic excitations are suppressed. This improvement is rapid for short evolution times and more gradual in the case of longer ramp times. However, the addition of phase noise causes an overall drop in fidelity for preparation across all evolution times, and in particular for longer evolution times where the cumulative dephasing leads to prolonged excitation out of the ground state. This difference in fidelity and energy is present for both stages and is best observed for the system size of $N = 11$, with a clear divergence between realizations with and without noise.

Looking at the final fidelity of the prepared state at the end of stage 2, Figure 4.4(a) shows the competition between diabatic and dephasing excitations, as both have very different excitation profiles and opposite relationships to evolution time. While diabatic excitation involves low energy eigenstates and occurs for short evolution times after loss of adiabaticity during fast Ω and δ variation rates, dephasing

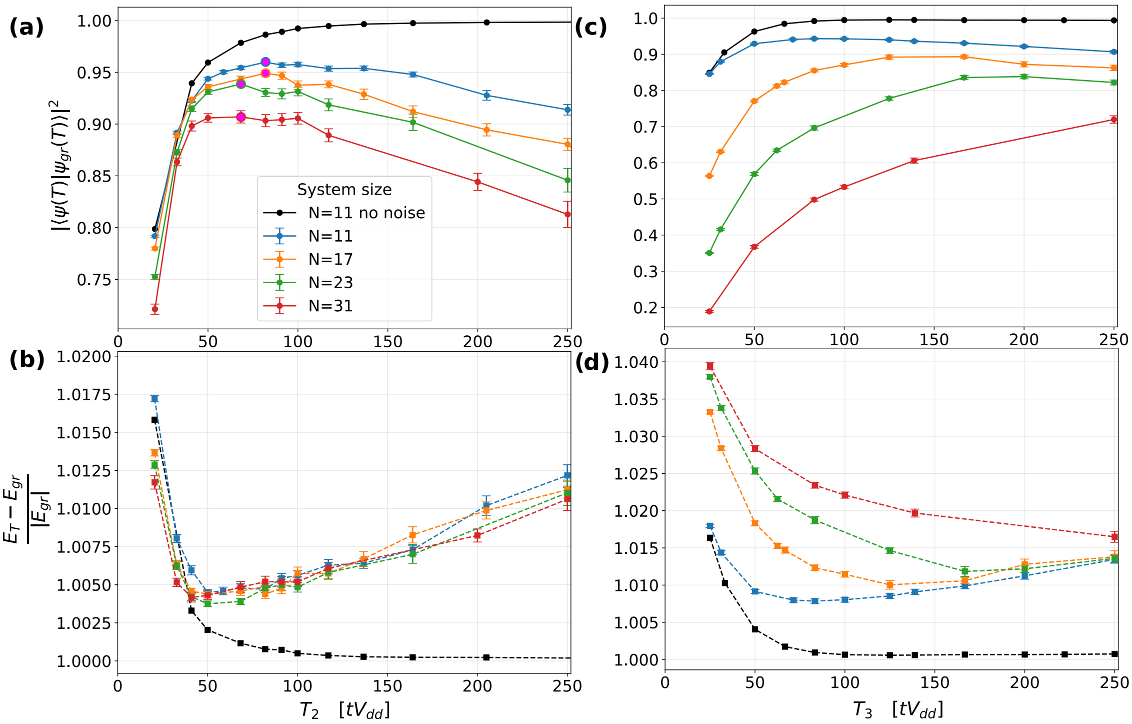

FIGURE 4.4: **Fidelity and energy after adiabatic state preparation of stages 2 and 3 with laser phase noise.** Final fidelity of prepared state $|\psi(T)\rangle$ with Z_2 ordered ground state $|\psi_{gr}(T)\rangle$ and final energy E_T relative to the ground state energy $E_{gr} = \langle\psi_{gr}|H_R|\psi_{gr}\rangle$ after simulations using different evolution times T_2 for stage 2 **(a,b)**, and T_3 for stage 3 **(c,d)** in the adiabatic state preparation described in Figure 4.3 with added laser phase noise. Colored lines show results for noisy state preparation with a variety of system sizes, while the black line provides a reference for 11 sites and no added noise. Optimal values of T_2 resulting in highest fidelity for a given N are highlighted in larger magenta circles in **(a)**, with their final states used for T_3 analysis. Each data point has error bars showing associated standard error after averaging over 100 preparations with unique laser phase noise signals generated from the same power spectrum in 2.6. These results have been calculated using tensor network simulations using the iTensor package in Julia [17], with time evolution achieved using the TDVP algorithm described in Section 3.2.5 with a maximum bond dimension of 100.

excitation can affect higher energy states and occurs after the gradual accumulation of phase errors in the laser drive affecting longer evolution times. This gradual accumulation is precisely why the standard error across all plots in Figure 4.4 increases with time and individual trajectories begin to diverge as independent phase errors build up. The competition between the two excitation mechanisms leads to the emergence of an optimal time T_{2O}, which is long enough to suppress most diabatic excitation but short enough to allow only small dephasing, thus corresponding to the largest achievable fidelity for a given system size. For stage 2 of the adiabatic state preparation T_{2O} remains roughly consistent between different system sizes, as diabatic excitation remains low except for the shortest evolution times, and the frequency profile of the added noise is the same across all simulations, and the generated noise signals take approximately the same time to begin affecting dynamics. The transition from mainly diabatic to mainly dephasing excitation occurs at a comparatively short evolution time of $T_2 V_{dd} \approx 60$ for all system sizes, as the ground state energy gap during this ramp remains large enough to permit faster variation rates without inducing excessive diabatic excitation (see Figure 4.2(c)). For stages 1 and 2, in ramps that are longer than $T_2 V_{dd} \approx 60$ diabatic excitation becomes insignificant, and we see a steady degradation of fidelity as phase error accumulates. In the context of added energy, Figure 4.4(b) echoes the transition between the two noise sources at $T_2 V_{dd} \approx 60$ as we see a clear shift in the rate of energy added by diabatic excitation and dephasing, with dephasing noise being a much more gradual process. Interestingly, for short evolution times energy appears to be lower for larger systems, since they have a higher density of states and smaller energy gaps, making it easier to excite diabatically out of the ground state and into states that have less energy with respect to the ground state than in the case of smaller systems. For longer adiabatic ramps we see energy rise linearly as a function of the time that phase noise has to accumulate, and this energy consistent across all system sizes since the same noise profile is being used

Moving on to stage 3 in Figures 4.4(c,d), we see that the dynamics become very different due to the dramatic increase in diabatic excitation as the system passes through a critical region in the parameter space where the ground state energy gap becomes very small (see Figures 4.1(b) and 4.2(c)). In Figure 4.4(c) this increase in diabatic excitation leads to much larger losses in fidelity that are more acute for larger system sizes, as they exhibit a larger density of states and smaller energy gaps. The improvements in fidelity from mitigating diabatic excitation when moving from short to longer evolution times are also much more gradual in stage 3 than across stages 1 and 2, where only ramps shorter than $T_2 V_{dd} = 50$ were strongly affected and the optimal ramp time remained consistently around $T_2 V_{dd} \approx 75$. Instead, the optimal evolution times in stage 3 increase with system size, from $T_3 V_{dd} = 100$ for 11 sites, to $T_3 V_{dd} = 167$ for 17 sites, and $T_3 V_{dd} = 200$ for 23 sites, as larger systems sizes are increasingly more susceptible to diabatic excitations and the variation rate must reduce considerably even at the cost of more dephasing. This system size susceptibility is echoed by Figure 4.4(d) where increasingly long evolution times are needed to return to the linear slope for which dephasing noise dominates added energy. This is consistent with recent analysis

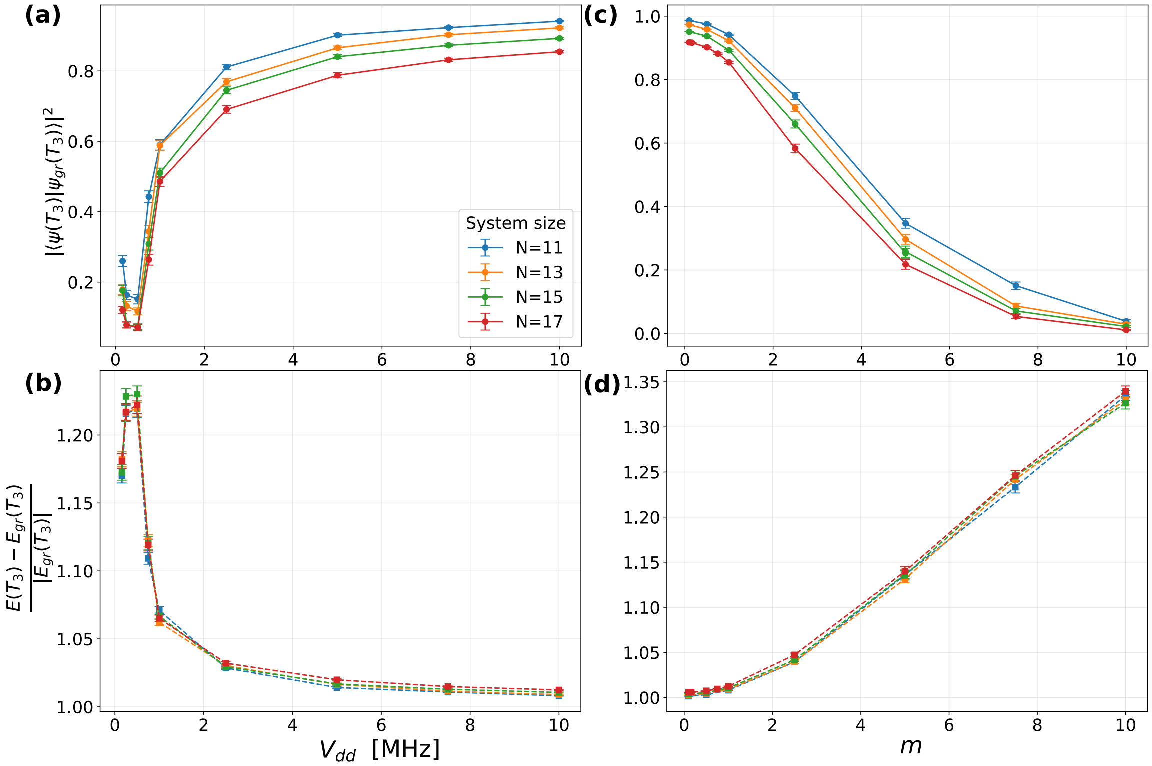

FIGURE 4.5: **Final fidelities and energies after adiabatic state preparation with varying interaction strength V_{dd} and noise strength m.** Final fidelities of the prepared state $|\psi(T_3)\rangle$ with Z_2 ordered ground state $|\psi_{gr}(T_3)\rangle$ along with corresponding energy $E(T_3)$ relative to the ground state $E_{gr}(T_3)$ for the adiabatic state preparation described in Figure 4.3 with optimal evolution times for stage 2 ($T_2V_{dd} = 82$) and stage 3 ($T_3V_{dd} = 83$). Results are provided for a variety of system sizes N, and two varying parameters. Final fidelity **(a)** and energy **(b)** for different values of $V_{dd}/2\pi$ ranging from $0.1 - 10$MHz. Final fidelity **(c)** and energy **(d)** for different linear scalings of magnitude m are applied directly to phase noise $\phi(t) \rightarrow m\phi(t)$, as was previously demonstrated in Figure 2.8. Error bars show standard error after averaging 100 preparations with unique laser phase noise signals. These results have been calculated using tensor network simulations using the iTensors package in Julia [17], with time evolution achieved using the TDVP algorithm from Section 3.2.5 with a maximum bond dimension of 100.

[20], predicting exceedingly long adiabatic ramps for larger system sizes due to diabatic losses.

Continuing the analysis, Figure 4.5 demonstrates the impact that a change in V_{dd} and noise strength has on the performance of the adiabatic protocol despite using optimal variation rates. First, Figures 4.5(a,b) show the final energies and fidelities after performing the protocol for a variety of V_{dd} values which, given that the laser parameters used are expressed in units of V_{dd}, shift the energy scaling of the entire system. Since the frequency profile of the noise remains constant with a broad peak in power at 480kHz (see Figure 2.6), tuning V_{dd} directly shifts the transitions to higher energy levels in and out of resonance. Phase noise made up of frequencies that are too high or too low relative to the dynamics of the system inhibits the transfer of power into the system, thereby causing less excitation out of the ground state. This is why Figures 4.5(a,b) show that the lowest energy added to the system, and thus the highest fidelity achieved, occurs furthest away from the peak noise frequency at $V_{dd} = 10$MHz, with a dramatic degradation in fidelity as the affected frequencies are approached at $V_{dd} = 0.5$MHz, and a visible improvement as they are surpassed. The result motivates the choice of 10MHz as a reasonable regime to test the performance of the protocol in Figure 4.4, and demonstrates that even if phase noise is present in a laser, the effects of phase noise on many-body experiments can be effectively mitigated by moving dynamics far away from affected frequencies. A similar conclusion was previously shown for single atoms and two qubit gates in [38, 116]. Following this, Figures 4.5(c,d) test how the protocol performs for different noise strengths by introducing a factor m that linearly scales the phase noise to $\phi(t) \rightarrow m\phi(t)$ (see Figure 2.8). The results demonstrate the susceptibility of such adiabatic protocols to phase noise, as we observe an almost complete degradation in fidelity with the target ground state within a single order of magnitude of amplification.

Studying the effects of phase noise on fidelity provides useful experiment-specific insight on imperfect adiabatic ramps in many-body systems. However, the measure considers only the ground state, revealing little about how dephasing distributes excitations across the energy eigenstates of the system. To get a deeper understanding of the mechanisms through which dephasing excitation propagates we have to analyze the full Hilbert space. The following section provides an analysis of the excitation dynamics for laser phase noise by studying the full energy spectrum of a one-dimensional chain of Rydberg atoms.

4.5 Excitation dynamics

To understand how laser phase noise excites a many-body system it is necessary to look beyond aggregate measures such as fidelity loss and total energy, and instead analyze how energy is distributed across the full Hilbert space. This section presents a detailed study of excitation dynamics in a one-dimensional Rydberg spin chain by examining how phase noise couples the ground state to other eigenstates.

To make the problem tractable, we consider a smaller system of $N = 11$ atoms, which allows for full diagonalization and symmetry-resolved analysis. We first explore how reflection symmetry splits the Hilbert space into distinct sectors, constraining the allowed transitions. We then evaluate matrix elements between instantaneous eigenstates at different points along the adiabatic path to identify which excitations are most strongly driven by phase noise. Finally, we supplement the matrix element analysis with a discussion of the excitation spectra of noisy time evolution under static Hamiltonians at various stages of the adiabatic preparation.

One of the goals of this analysis will be to reveal how integrability and spectral structure influence the ability of phase noise to spread energy throughout the system. However, before beginning the discussion on excitation dynamics is useful to define what is meant by integrability in the context of the Rydberg chain Ising Hamiltonian we are simulating in this thesis, as this term may often be used to cover a wide range of phenomena across different systems. In this work, integrability refers to the regime where the system's dynamics are governed by a complete set of conserved quantities, resulting in a highly structured and 'predictable' energy spectrum. In the limit of $\Omega \to 0$, the Hamiltonian reduces to a Ising model where the number of Rydberg excitations is conserved, as without the transverse field there is no mechanism to flip the states of individual sites. Consequently, eigenstates are simply computational basis states, and the ground state is determined by the competition between δ and V_{dd}. In this integrable regime, the system is 'stuck' in a specific energy sector with different degenerate configurations with the same number of Rydberg excitations. As the transverse field Ω is increased, these conservation laws are broken, and the system transitions into a non-integrable, or chaotic, regime. While the transition to a non-integrable regime is gradual and impossible to pinpoint precisely, it is marked by a break-down of degeneracy as Ω introduces state mixing which makes the degenerate computational states form superposition states with varying energies. At larger Ω the once isolated energy sectors merge into one sector with a high density of eigenstates that have distinct energies, making dynamics in such a system much more complex, as different couplings between states across the entire energy spectrum become accessible. Dynamics in such non-integrable systems becomes much more difficult to calculate especially at larger system sizes. The following discussions aim to show how this breakdown of integrability acts as a bridge, allowing phase noise to couple the ground state to a dense manifold of excited states that would otherwise be inaccessible in the highly structured and disconnected energy spectrum of the strictly integrable Hamiltonian.

4.5.1 Reflection symmetry

Importantly, the Hamiltonian defined in Eq. (4.2) has a reflection symmetry in the computational basis. Limiting ourselves once again to odd numbers of sites, a reflection operator that flips all sites about the center of the chain can be defined in terms of $\sigma_+ = (\sigma_x + i\sigma_y)/2$ and $\sigma_- = (\sigma_x - i\sigma_y)/2$ operators as

$$\begin{aligned}\hat{R} = \Bigg[\bigotimes_{i=1}^{(N-1)/2} \Bigg(&\hat{\sigma}_+^{(i)}\hat{\sigma}_-^{(N-i+1)} + \hat{\sigma}_-^{(i)}\hat{\sigma}_+^{(N-i+1)} \\ &+ \frac{1}{2}\big(1 + \hat{\sigma}_z^{(i)}\hat{\sigma}_z^{(N-i+1)}\big)\Bigg)\Bigg] \otimes 1^{(c)},\end{aligned} \tag{4.3}$$

where $c = (N+1)/2$ is the central site index and we leave it unchanged by applying the identity. The first two terms in the operator flip sites at either end of the chain while the third term ensures the preservation of the spin alignment if both sites are in the same state. The Hamiltonian in Eq. (4.2) can be shown to commute with this reflection operator, including the interaction term which governs diabatic excitation and the transverse field term through which phase noise is introduced. As a result, both forms of excitation in the system respect this reflection symmetry, leading to a Hilbert space that is split into two independent symmetry sectors of eigenstates made up of symmetric (for example: $|110\rangle + |011\rangle$) and anti-symmetric (for example: $|110\rangle - |011\rangle$) superpositions of computational states. Moreover, for open boundary one-dimensional spin chains with an odd number of sites, there will always be computational states that are invariant under reflection. The crystalline states discussed in Section 4.1.1 that dominate the ground state for low values of Ω are one such example of reflection invariance. Such reflection invariant computational states are only represented in the symmetric energy eigenstates. This means that if the initial state is fully represented by one of these symmetry sectors, as is the case with the symmetric ground state at the beginning of the adiabatic state preparation, all dynamics will be confined to that symmetry sector. This effectively inhibits excitation in approximately half of the Hilbert space, as the fraction of symmetric and anti-symmetric states remains roughly 0.5, with minor changes between different Hamiltonian parameter regimes.

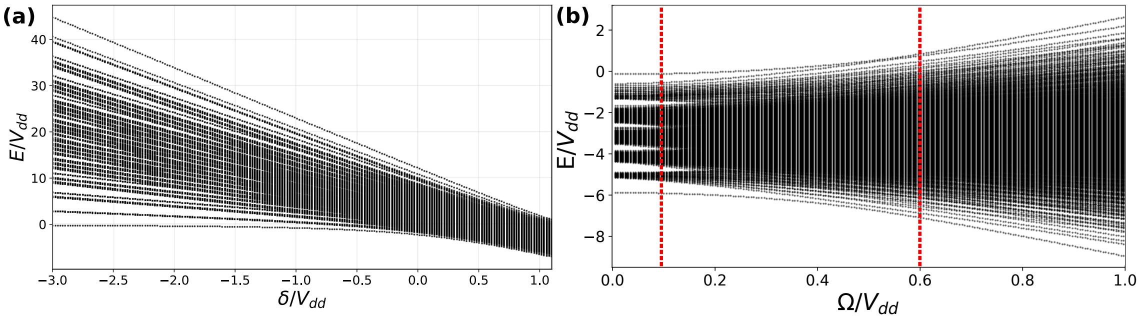

FIGURE 4.6: **Energies of symmetric eigenstates as a function of δ/V_{dd} for stage 2 and Ω/V_{dd} for stage 3 of the adiabatic protocol.** A plot of symmetric energy eigenvalues of the Rydberg Hamiltonian defined in Eq. (4.2) as a function of **(a)** detuning δ/V_{dd} with constant Rabi frequency $\Omega/V_{dd} = 0.6$ (as seen in stage 2 of the adiabatic protocol), and **(b)** Rabi frequency Ω/V_{dd} for a constant detuning of $\delta/V_{dd} = 1.1$ (as seen in stage 3 of the adiabatic protocol). Red lines mark final and initial Ω throughout stage 3, such that the set of eigenvalues at $\delta/V_{dd} = 1.1$ in **(a)** is the same as the set of eigenvalues at $\Omega/V_{dd} = 0.6$ in **(b)** marking the initial regime in stage 3.

4.5.2 Energy structure and integrability

Figure 4.6 shows the separation of eigenenergies corresponding to symmetric eigenstates as a function of the laser parameters in stages 2 and 3 of the adiabatic protocol. In the case of stage 2 in Figure 4.6(a), we are working at a constant Rabi frequency of $\Omega/V_{dd} = 0.6$, and ramping up from a red-detuned regime with $\delta/V_{dd} = -3$ to a blue detuned regime with $\delta/V_{dd} = 1.1$, which gradually lowers the energy gap between eigenstates and lowers the energy required for many-body states with Rydberg excitations along the chain to be more favorable. The non-zero Ω throughout this process ensures there is always a level of state mixing and the system is in a non-integrable regime. In stage 3, shown by Figure 4.6(b), we instead operate with a constant detuning of $\delta/V_{dd} = 1.1$ and the Rabi frequency is ramped down from $\Omega/V_{dd} = 0.6$ to $\Omega/V_{dd} = 0.1$. The two red lines indicate the minimum value for Ω/V_{dd} at the beginning and end of the protocol, as well as the maximum value that is held constant through stage 2. Tracing the bottom line, which represents the ground state energy, we see that the minimum ground state energy gap which corresponds to the critical region of the preparation occurs between $\Omega/V_{dd} \in \{0.4 - 0.6\}$. For low values of Ω/V_{dd} there is an underlying structure of clustered energy eigenstates that is consistent with what one might expect in an integrable Ising Hamiltonian. However, as Ω/V_{dd} is increased there is a rapid breakdown of this structure, as energy clusters merge and the total energy spanned increases. This merging corresponds to the breaking of integrability that occurs when a transverse field is applied to the Ising Hamiltonian. This transition from an integrable to a non-integrable system is captured within the maximum and minimum Ω/V_{dd}, with the low energy eigenstates that typically dominate dynamics in ground state protocols appearing mixed at the highest values and starting to segregate after $\Omega/V_{dd} = 0.2$, and will be shown in the following sections to have direct implications for phase noise excitation.

4.5.3 Matrix element analysis

The anatomy of excitation in a quantum system is governed by transition rates between different energy eigenstates, and the ability of a given excitation mechanism to transfer energy through those available channels. In terms of laser phase noise acting on a ground state, the crucial factor is the density of energy eigenstates both with a high enough transition rate with the ground state and that are resonant with the frequency components carrying significant power in the noise spectrum. The relevant operator that mediates excitation along the spin chain is the many-body number operator $\hat{n}$, or equivalently, the many body operator $\hat{\sigma}_z = \sum_k^N \hat{\sigma}_k^z$ operator. Thus, working in the rotating frame in which noise acts on the system as $-\left[\delta(t) - \dot{\phi}(t)\right] \sum_k^N \hat{n}_k$ (see Appendix C for details), we can evaluate available transition rate to any energy state ,$|E_m\rangle$, by calculating the square of the off-diagonal matrix elements $|\langle E_l|\hat{\sigma}_z|E_m\rangle|^2$, where l is an index of all states along the Hilbert space $l \in [0, 2^N]$. As discussed in the previous subsections, we only consider symmetric eigenstates.

Figure 4.7 shows the distribution of transition rates between different many-body energy eigenstates for the Hamiltonian defined in Eq. (4.2) with parameters that occur at four different points throughout stages 2 and 3 of the adiabatic state preparation studied in this chapter. Each plot shows transitions for the ground state $|E_0\rangle$, along with transitions for the state with the highest transition rate with respect to $|E_0\rangle$, in addition to states that have the highest transition rates with the preceding analyzed state. In this way, we trace the most probable excitation path for a population starting in the ground state, getting insight on how excitation dynamics changes throughout the protocol. Each analyzed state is marked by a dashed line of the same color as its transition rates, and we denote higher energy states as $|E_x\rangle$ where the index x represents the order in which they appear in the

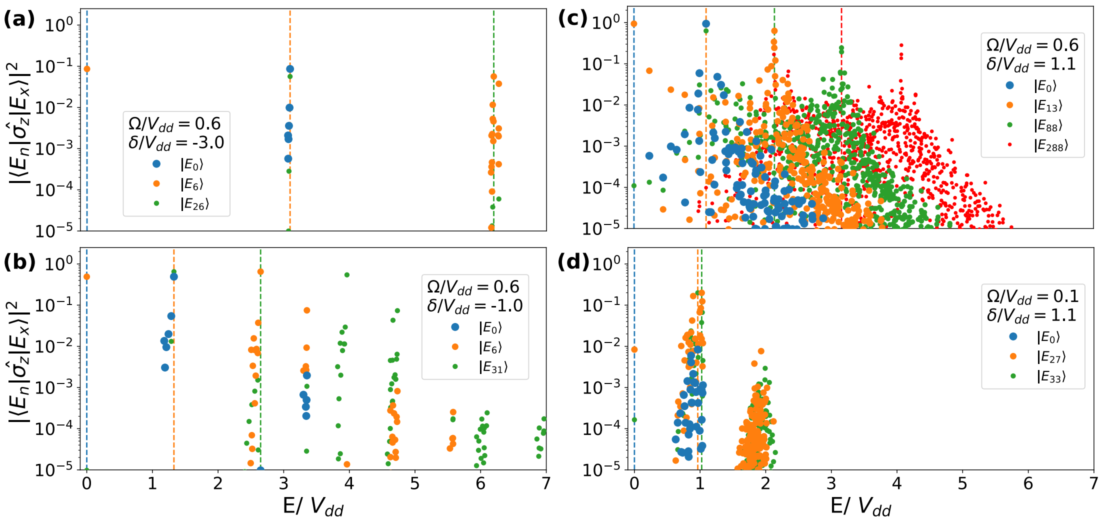

FIGURE 4.7: **Transition rates for eigenstates of different Hamiltonians along stages 2 and 3 of the adiabatic state preparation for 11 sites.** Off-diagonal matrix elements representing transition rates of the many-body operator $\hat{\sigma}_z = \sum_k^N \hat{\sigma}_z^k$ between energy eigenstates $|E_i\rangle$ of Hamiltonians at different points during stages 2 and 3 of the adiabatic state preparation initialized in the ground state $|E_0\rangle$. We show results for the initial Hamiltonian of stage 2 **(a)**, with laser parameters $\Omega/\mathrm{V}_{dd} = 0.6$ and $\delta/\mathrm{V}_{dd} = -3$, an intermediate stage 2 Hamiltonian with parameters **(b)** $\Omega/\mathrm{V}_{dd} = 0.6$ and $\delta/\mathrm{V}_{dd} = -1$, the initial Hamiltonian of stage 3 **(c)** with parameters $\Omega/\mathrm{V}_{dd} = 0.6$ and $\delta/\mathrm{V}_{dd} = 1.1$, as well as the final Hamiltonian of the protocol **(d)**, with parameters $\Omega/\mathrm{V}_{dd} = 0.1$ and $\delta/\mathrm{V}_{dd} = 1.1$. Dashed lines mark energies analyzed states starting with the ground state (blue), the state with the highest ground state transition rate (yellow), and subsequent states that correspond to the highest transition rates from the preceding state (green, red). Dots of matching color represent off-diagonal matrix elements for that state.

energy structure. Note that different eigenstates may occupy the same index at different stages of the protocol as the energy structure changes dynamically.

We begin in Figure 4.7(a) with the Hamiltonian occurring at the start of stage 2, where there is a single dominant transition from the ground state $|E_0\rangle$ to the sixth excited eigenstate $|E_6\rangle$ at an energy of $E_6/V_{dd} \approx 3$. The remaining non-negligible transition probabilities are at least an order of magnitude smaller, found at a similar energy to E_6. As $|E_6\rangle$ becomes excited over time, its transition elements also become relevant, with two dominant excitation channels that excite upwards to $|E_{26}\rangle$ with energy $E_{26}/V_{dd} \approx 6$ and other nearby states, or de-excite back to $|E_0\rangle$ leading to an oscillatory behavior between the two states. This behavior is repeated for $|E_{26}\rangle$. Comparing with the stage 2 eigenstate distribution plot in Figures 4.6(a) we see that the large negative detuning $\delta/V_{dd} = -3$ in this regime makes higher energy states energetically unfavorable, resulting in lower and sparser transition rates that require more noise power to overcome large energy gaps. Moving on to transition rates in Figure 4.7(b), occurring in a parameter range directly in the middle of stage 2, we see a marked drop in energy gaps between eigenstates and an increase in their transition rates as detuning becomes less negative at $\delta/V_{dd} = -1$. The state $|E_6\rangle$ now appearing at an energy $E_6/V_{dd} \approx 1.3$ remains the preferred transition from $|E_0\rangle$, with small cohorts of higher excited states also becoming relevant. The increase in δ throughout stage 2 decreases the energy gaps between states (as seen in Figure 4.6(a)), such that diabatic and dephasing noise require less energy for excitation. Coupled with a high transverse field of $\Omega/V_{dd} = 0.6$ that keeps the Hamiltonian non-integrable by introducing state mixing that makes delocalized transitions (transitions which are far apart energetically) more favorable, stage 2 reconfigures the energetic structure not only to make phase noise excitation out of the ground state more likely, but also to increase the occurrence of subsequent excitation to disperse added energy across the entire spectrum. The culmination of these effects can be seen at the transition point between stages 2 and 3 in Figure 4.7(c) with laser parameters $\Omega/V_{dd} = 0.6$ and $\delta/V_{dd} = 1.1$, where we see a dramatic increase in both the density of available state and the magnitude of their respective transition rates. The highlighted excitation path of $|E_0\rangle \to |E_{13}\rangle \to |E_{88}\rangle \to |E_{288}\rangle$ is the most dominant, forming an array of equidistant peaks that can allow fast transfer of energy from the ground state to higher energy sectors. Furthermore, the high number of eigenstates with an elevated transition rate give phase noise a greater scope to excite the system at a wider range of frequencies than at any other point throughout the adiabatic process. In the final Hamiltonian of the adiabatic state preparation with $\Omega/V_{dd} = 0.1$ in Figure 4.7(d) we see that the excitation probability from the ground state as well as the higher energy states becomes strongly suppressed. For $|E_0\rangle$, the most dominant transition has a probability that is two orders of magnitude smaller than the one in Figure 4.7(c), suggesting that the ground state is much more robust to noise excitation in the final stages of the ramp. Moreover, the energy eigenvectors that dominated the excitation dynamics in Figure 4.7(c) appear as higher excited states, and the equidistant transition peaks of the matrix elements are replaced with transitions for much smaller probabilities that cluster near their respective eigenstate. This suggests that excitation due to laser phase noise is much more constrained in the final stages of the experiment, with available excitation states localized in energy and having smaller transition rates.

The differences between the last two sets of matrix elements can be explained by the competition between the two laser parameters in the Hamiltonian in Eq. (4.2). As Ω/V_{dd} is decreases, the integrability of the Hamiltonian changes, which has strong implications on the transition element spectrum. This change transitions the system from a non-integrable state with large state mixing to an integrable state that approaches the Ising model [196, 197]. Higher integrability leads to underlying structure in the energy levels, which form clusters separated by large energy gaps (see Figure 4.6). Such energy gaps, coupled with the lack of transition elements that are delocalized in energy that could facilitate excitation to different energy regions, inhibit the spread of excitation energy throughout the Hilbert space. Of course, the picture is much more complicated in the dynamical setting of adiabatic state preparation where a time dependent $\Omega(t)$ constantly changes excitation patterns, but Figure 4.7, along with phase noise evolutions of time-independent Hamiltonians at various stages of the preparation, provides evidence that phase noise excitation is highly interlinked with the integrability of the system. As the transverse field that breaks integrability decreases, so does the ability of the phase noise to excite the system.

4.5.4 Constant Hamiltonian analysis

While it is possible to treat the adiabatic state preparation as a black box and analyze only the final state, getting a deeper understanding of the complicated excitation dynamics of laser phase noise in a time-dependent Hamiltonian with ever changing energy level structure is much harder. The transition rates discussed in Figure 4.7 provide a road map for a given source of energy to excite the system to higher many-body states. In order to bring these transition rate snapshots to life, in this section we perform an analysis of excitation dynamics using the same time-independent Hamiltonians in the parameter regimes shown in Figure 4.7.

Since this work considers laser phase noise excitation, we want to know exactly how much energy such noise can transfer to the system at these different stages of the adiabatic ramp and if the excitation dynamics align with transition rate predictions. The specific experimentally realistic noise used is shown in Figure 2.6 with a broad power peak at 480kHz, and in this chapter we have predominately studied it in a regime with interactions scaled at $V_{dd}/2\pi = 10$MHz to mitigate a majority of the power transfer and make the preparation of the adiabatic state perform reasonably well. Figure 4.8 shows the diagonal ensembles $|\langle\psi(T_3)|E_i\rangle|^2$ for

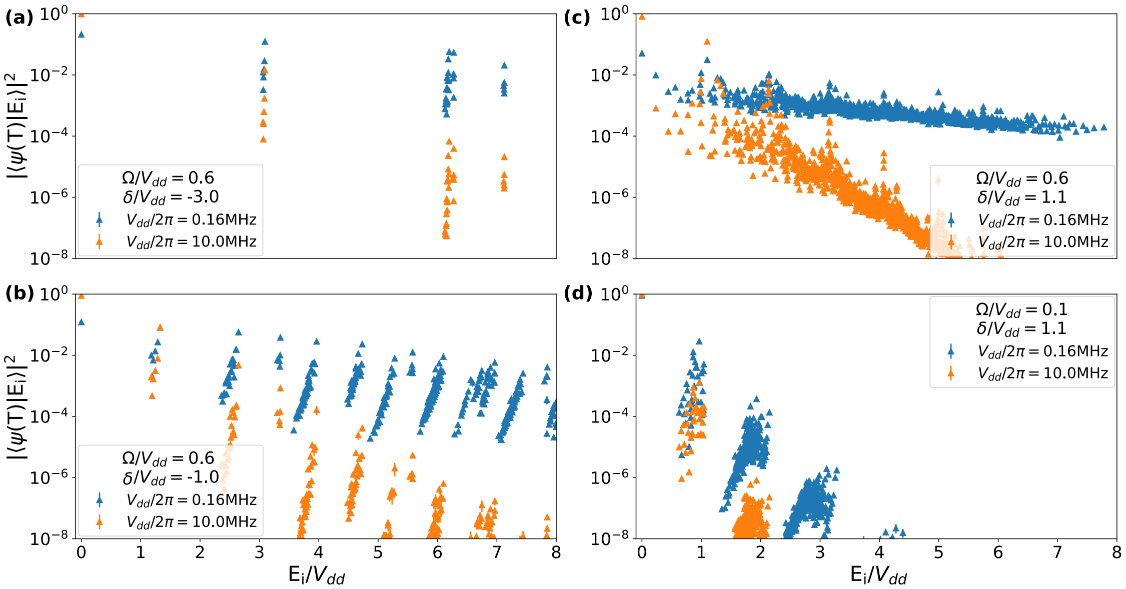

FIGURE 4.8: **Excitation spectra after ground state evolution with time-independent Hamiltonian with 11 sites.** The ground state of the Hamiltonian from Eq. (4.2) is evolved with noise for a total time of $TV_{dd} = 300$, for different laser parameters **(a)** $\Omega/V_{dd} = 0.6$ and $\delta/V_{dd} = -3.0$, **(b)** $\Omega/V_{dd} = 0.6$ and $\delta/V_{dd} = -1.0$, **(c)** $\Omega/V_{dd} = 0.6$ and $\delta/V_{dd} = 1.1$, **(d)** $\Omega/V_{dd} = 0.1$ and $\delta/V_{dd} = 1.1$. In orange we have the diagonal ensemble after noisy evolution with site interaction strength set to $V_{dd}/2\pi = 10$MHz, while in blue we have the same simulation reproduced for an interaction strength of $V_{dd}/2\pi = 0.16$MHz. Error bars plot standard error across 100 time evolutions with independent laser phase noise signals using the same noise profile from Figure 2.6, but are too small to be seen on the log scale suggesting a consistent excitation pattern.

state $|\psi(T_3)\rangle$ after a ground state evolution of the time-independent Hamiltonians with energy eigenstates $|E_i\rangle$ and laser parameter regimes studied in Figure 4.7, averaged across 100 independent noise realizations and for two separate interaction strength regimes $V_{dd}/2\pi = 0.159, 10$ MHz. To ensure both regimes have equivalent dynamics when no phase noise is added, simulations are performed for a fixed total evolution time of $TV_{dd} = 300$, which corresponds to completing the protocol in $\approx 4.8\mu$s for the fast 10MHz regime and 300μs for the slow 0.159MHz regime. The resulting diagonal ensembles show occupation probability across all energy eigenstates averaged over one hundred noise realizations, and are generally in strong agreement with transition rate predictions of Section 4.5.3.

Figure 4.8(a) shows the noisy evolution of the ground state of a Hamiltonian that occurs at the beginning of stage 2 of the adiabatic protocol. The resulting excitation is very low in the $V_{dd}/2\pi = 10$MHz regime with a final ground state occupation of 98.2% at a standard error of 0.2%, but much larger in the $V_{dd}/2\pi = 0.16$MHz regime in which ground state population dropped to 21.1% with standard error of 3%, suggesting that proximity of the dynamical frequency of the system to the 0.48MHz peak is a key factor for driving excitation even in the far detuned regime with a low density of states with high transition rates. Figure 4.8(b) with laser parameters from the middle of stage 2 paints a similar picture but with a modest increase in excitation across the spectrum as the energy gap between states decreases and more states become viable for excitation. The $V_{dd}/2\pi =$ 10MHz regime here has a final ground state population 89.4% at a standard error of 2%, while the ground state of the $V_{dd}/2\pi = 0.16$MHz regime drops further to 12.1% with a standard error increasing to 4%. In particular, energy in the $V_{dd}/2\pi = 0.16$MHz regime is much more evenly distributed throughout the energy spectrum than in the case of the $V_{dd}/2\pi = 10$MHz regime, which has a much higher drop-off in occupation of higher energy states as most energy is still concentrated in the ground state and states with the highest ground state transition rate. As predicted in the matrix element analysis, Figure 4.8(c) that uses a parameters from the transition point between stages 2 and 3 results in the most overall excitation, with a ground state occupancy of 81.5% at a 3% standard error for the $V_{dd}/2\pi =$ 10MHz regime, and an almost fully depleted ground state occupancy of 5.1% at a 1% standard error for the $V_{dd}/2\pi = 0.16$MHz regime. The evolution of the $V_{dd}/2\pi = 10$MHz regime results in the formation of well-defined equidistant peaks as the energy of the phase noise occupancy cascades from one high transition rate to the next with gradually decreasing probability. While these peaks are still visible in the $V_{dd}/2\pi = 0.16$MHz regime, the comparatively stronger effect of phase noise leads to higher energy transfer with occupancy largely equilibrating across the entire spectrum. All three of these figures with a high transverse field at $\Omega/V_{dd} = 0.6$ have excitation profiles dominated by transitions that are delocalized in energy, allowing noise to access the entire energy spectrum over time. Moreover, the rate of energy transfer improves as δ becomes increasingly positive and the energy required for transitions between many-body states with different numbers of atoms in a Rydberg state drops (see Figure 4.6(a)). However, for the Hamiltonian that occurs at the end of the protocol seen in Figure 4.8(d), in which δ is positive but the transverse field drops down to $\Omega/V_{dd} = 0.1$, there is a dramatic decrease in excitation across both regimes of 99.4% and 90.0% for the $V_{dd}/2\pi = 10$MHz and $V_{dd}/2\pi = 0.16$MHz regimes respectively. The main difference is that the system here is much more integrable, leading to available transition rates that are not only lower but also highly localized in energy, meaning that phase noise can both transfer less energy to the system, and also is restricted in how far across the spectrum that energy can spread.

4.6 Summary

In this Chapter we introduced adiabatic state preparation as an established technique for accessing complex many-body ground states in quantum systems, with a focus on its implementation in one-dimensional Rydberg spin chains. The Chapter built upon the motivation behind adiabatic ramps and their utility in quantum simulation and annealing protocols discussed in Section 1.2.1.1, introducing it in the context of preparation of crystalline phases and spin-ordered ground states in Rydberg tweezer arrays that are otherwise difficult to access. The numerical simulation of such an adiabatic experiment was then used for the study of laser phase noise in a many-body system, with a detailed analysis of the detrimental effect of dephasing on the adiabatic process, as well as the mechanisms that control the resulting excitation dynamics.

Section 4.1 introduced the transverse-field Ising model (TFIM) and described how it arises naturally in Rydberg atom arrays. Section 4.1.1 explored the crystalline ground states of the TFIM in different parameter regimes, explaining how blockade interactions and detuning lead to self-ordered phases such as the Z_2 ordered state. It was shown that such states emerge within well-defined regions of parameter space and exhibit robustness against small perturbations, making them suitable targets for state preparation. Building on this understanding, Section 4.2 detailed the three-step adiabatic state preparation protocol described in [114] that prepared the Z_2 ordered phase with high fidelity by slowly tuning the Rabi frequency and detuning of the laser drive. Numerical results were presented to illustrate how diabatic errors accumulate, particularly in regions of small energy gap, and how careful tuning of the ramp speed is necessary to preserve ground-state occupancy. Finally, Section 4.2.1 provides a discussion on variation rate sensitivity, showing how fidelity depends critically on the speed of parameter changes near critical points in the ramp.

After laying the foundations for adiabatic state preparation of crystalline ground states in the TFIM, Section 4.3 initiates work on the central findings of this thesis by subjecting these simulations to realistic laser phase noise generated using the

the TK95 algorithm described in Section 2.3. This is done by modifying the transverse drive to include a fluctuating phase term, allowing the noise to manifest as an effective time-dependent detuning in the rotating frame. This formulation provided a natural framework for analyzing the influence of laser noise on many-body dynamics by inducing excitation. Section 4.4 evaluates final fidelities of ramps with different durations and noise profiles to assess the performance of the state preparation with added phase noise. Here, we identified a competition between diabatic excitation—dominant at short ramp times—and phase noise-induced dephasing, which accumulates over longer durations. This competition leads to an optimal ramp time that balances both effects and maximizes fidelity. In addition to this, we show that fidelity can be improved significantly by decreasing interaction strength as well as by shifting the noise spectrum away from the frequencies most relevant to the system's dynamics.

To gain deeper insight into the excitation dynamics of phase noise, Section 4.5 works in a smaller fully diagonalizable system of $N = 11$ atoms, focusing on how phase noise distributes energy across the entire Hilbert space. To begin with, Section 4.5.1 explored how reflection symmetry splits the Hilbert space into symmetry sectors, constraining excitation dynamics. We showed that, since all dynamics originate from the symmetric ground state, transitions are confined to the symmetric subspace—effectively halving the accessible density of states. In addition we also discuss integrability in the system in Section 4.5.2. Next, Section 4.5.3 provides matrix element analysis of the number operator $\hat{n}$ which describes the available energy transitions for excitation. The analysis reveals that dominant off-diagonal couplings first increase throughout stage 2 of the protocol to a point where density of states with high transition rates covers a majority of the energy spectrum, and then diminish in stage 3. The reason for this is the increasing detuning in stage 2 that makes Rydberg excitation more favorable and lowers energy gaps between states, and a subsequent lowering of the transverse field in stage 3 that makes the system increasingly integrable, suppressing state mixing and reduces the system's susceptibility to noise. Finally, in section 4.5.3 we studied excitation using time-independent simulations with static Hamiltonians sampled along the adiabatic path. These revealed a clear correspondence between the strength of off-diagonal couplings and the observed excitation spectra: as detuning increases through stage 2, enhanced state mixing enables broader energy redistribution, while the reduced transverse field in stage 3 restores integrability, suppresses off-diagonal transitions, and limits further excitation. This establishes a direct link between the evolving Hamiltonian structure and the system's susceptibility to phase noise throughout the adiabatic protocol.

Overall, the results in this chapter demonstrate the importance of understanding and mitigating laser phase noise in a given system, demonstrating useful tools for simulating and analyzing laser phase noise in a given quantum system. We find that the structure and dynamics of phase noise excitation are intricately linked to the spectral properties and integrability of the underlying Hamiltonian. The findings emphasize the importance of both system design and noise engineering in ensuring robust quantum control in Rydberg-based platforms.

Chapter 5

Thermalization of laser phase noise

The presence of phase noise introduces energy into the system, and it is natural to ask if and how this added energy thermalizes. We define thermalization as a relaxation to states where the values of macroscopic observables become stationary over long periods of time, across widely differing initial conditions, that is predictable by the use of statistical mechanics [197]. The mechanisms underpinning thermalization in quantum systems vary considerably from classical systems. In the classical case, we typically discuss thermalization in terms of chaotic dynamics in the phase space of ergodic systems [198, 199], which, when evolved for a long time at a given energy, will explore all accessible states such that the statistical distribution for occupancy resembles the Boltzmann distribution. For a truly ergodic system, such a statistical distribution across all available states remains constant in time and is reached independently of initial conditions, thus constituting a thermal equilibrium to which the system will eventually relax. However, this understanding of thermalization is incompatible with isolated quantum systems for which the notion of dynamical chaos is absent due to the linearity of time evolution and discreteness of available states but also because the basic variables of classical phase space, position and momentum, are incommensurate in quantum mechanics. This means that no sharp, deterministic path through phase space exists to support the notion of ergodicity in the classical sense. Instead, thermalization in quantum many-body systems is believed to arise through mechanisms such as the Eigenstate Thermalization Hypothesis (ETH), which posits that individual energy eigenstates already encode thermal behavior when probed by local observables. Under ETH, a quantum system can appear thermal even while evolving unitarily, assuming the system in question is sufficiently non-integrable and the observable being evaluated behaves locally as a smooth function of energy. In this framework, energy injected by noise may distribute itself across the many-body Hilbert space in a way that mimics relaxation to a thermal distribution, not through random trajectories but through excitation dynamics in the complex structure of energy eigenstates.

Thermalization of the kind described by the ETH has been observed in several isolated quantum systems [23, 200–205], but integrable systems that exhibit a large number of conserved quantities do not reach thermal equilibrium [204, 206–208], and instead relax to the generalized Gibbs ensemble [209, 210]. Whether or not thermalization is observed at the end of the adiabatic state preparation discussed in Chapter 4 depends strongly on the choice of observable and the integrability of the Hamiltonian. In the case of the Rydberg spin system described in Chapter 4 (see Sections 4.1,4.3), the long-range dipole-dipole interactions between Rydberg atoms introduce a layer of complexity beyond conventional nearest-neighbor models [211] which instead resemble the integrable Ising model. These long-range interactions weaken integrability and lead to emergent many-body phenomena such as quasi-long-range order [42, 51, 114], frustration [212], and modified critical behavior [213]. Furthermore, such interactions modify the excitation spectrum, allowing for nonlocal transitions and collective dynamics that provide phase noise with additional avenues to propagate through the system. This enhanced sensitivity to noise affects the response of the system to dynamical protocols such as adiabatic state preparation in nontrivial ways, making them both experimentally relevant and theoretically intriguing. To probe thermalization under noise for such systems, the operators discussed in this chapter are chosen to quantify long-range interactions. The $\sigma_z \sigma_z$ correlation operator and the interaction energy operator, $\hat{H}_{int}$, are natural choices: the former captures spatial correlations and emergent ordering, while the latter directly reflects the amount of energy across all interactions. Importantly, features of the adiabatic state preparation such as long evolution times and changing integrability in the Hamiltonian also make it a pertinent testbed for studying thermalization. The discussion in Section 4.5.3 and 4.5.4 reveals that the state preparation traverses regions of differing integrability as the transverse field is reduced in stage 3, dynamically shifting the system's susceptibility to noise. Furthermore, the presence of a reflection symmetry discussed in Section 4.5.1 constrains the dynamics to a symmetry sector that makes up roughly half of all eigenstates in the Hilbert space, not only reducing available excitation paths for the phase noise but also limiting relaxation processes for any energy that is added to the system.

This Chapter is organized as follows: we first discuss a change of regime, performing the simulations in this chapter using an interaction strength of $V_{dd}/2\pi = 0.16$ also seen in Figure 4.8, where the noise has considerably more effect on the experiment and thermalization can be studied more readily. Then, after a brief formal introduction to the ETH and its connection to statistical ensembles, we begin by evaluating thermalization of phase noise in simulations of adiabatic state preparation for a fully diagonalizable system of $N = 11$ atoms with long-range interactions. We use diagonal and canonical ensembles to compare long-time expectation values for thermal predictions of two observables that relate to long-range interactions in the interaction energy $\hat{H}_{\text{int}}$ and the Z_2 order parameter $\hat{O}_{Z_2}$. Building on this, we isolate the role of long-range interactions by repeating the thermalization analysis for a modified nearest-neighbor TFIM. Such nearest-neighbor interacting systems are known to be more integrable and thus display a more structured energy spectrum that can suppress excitation. Finally, the last section of the Chapter explores system size effects by extending the analysis to larger spin chains using matrix product state (MPS) simulations. In this regime, where exact diagonalization is no longer feasible, thermal behavior is inferred by comparing the expectation values of prepared states to thermal predictions at equivalent energy.

5.1 Changing parameter regimes

Before we formally introduce thermalization it is useful to shift our simulations to a regime in which noise excitation is stronger. In Chapter 4 the focus was placed on studying the impact of laser phase noise on high-fidelity adiabatic state preparation. Operating in the $V_{dd}/2\pi = 10$ MHz regime kept the characteristic system frequencies well above the dominant noise peak near 0.48 MHz (see Chapter 2, Figure 2.6), which suppressed excitation and maintained the system close to its instantaneous ground state. In contrast, the following chapter examines the dynamics from the opposite perspective; rather than mitigating phase noise, we exploit its coupling to the system to study how noise can drive energy redistribution and apparent thermalization in an interacting Rydberg chain. For this purpose, we shift to a lower frequency interaction regime of $V_{dd}/2\pi = 0.16$ MHz

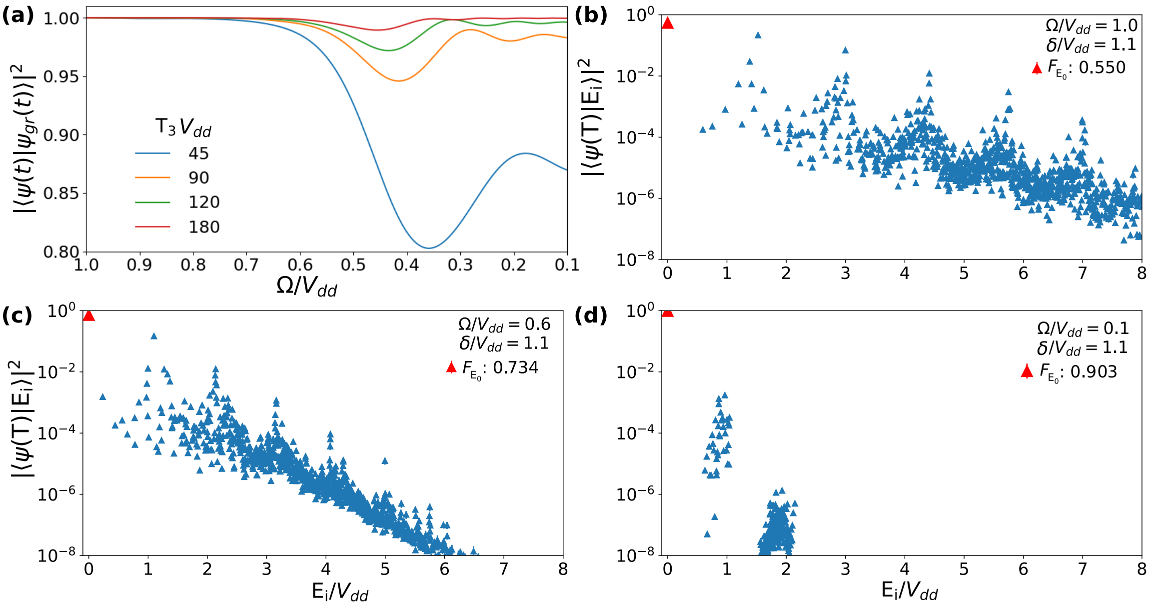

FIGURE 5.1: **Isolating a modified stage 3 of the adiabatic state preparation for 11 sites with $V_{dd}/2\pi = 0.16$ MHz. (a)** Plot of fidelity against decreasing values of Ω/V_{dd} for a modified version of the stage 3 adiabatic ramp discussed in Chapter 4, now starting from $\Omega/V_{dd} = 1.0$. Simulations have no phase noise and colored lines show the fidelity for different evolution times, with faster ramps incurring more diabatic excitation. **(b-d)** The ground state evolution of time independent Hamiltonians from Eq. (4.2) with laser phase noise for a total time of $TV_{dd} = 400$. Plots show different laser parameters throughout stage 3 with detuning set to $\delta/V_{dd} = 1.1$ and Rabi frequency set to **(b)** $\Omega/V_{dd} = 1.0$, **(c)** $\Omega/V_{dd} = 0.6$, and **(d)** $\Omega/V_{dd} = 0.1$. Red triangles mark the ground state fidelity, F_{E_0}, which is also provided in the legend. Error bars plot standard error across 100 time evolutions with independent laser phase noise signals using the same noise profile from Figure 2.6, but are too small to be seen on the log scale suggesting a consistent excitation pattern.

that was also studied in Figure 4.8, where the characteristic transition energies of the Hamiltonian become comparable to the spectral components of the laser noise.

In the $V_{dd}/2\pi = 0.16$ MHz regime, preparation of high-fidelity adiabatic states is no longer feasible, as shown in Figure 4.5(a), in which the fidelity of the prepared state decreased to below 20% even for the smallest system size of 11 sites. Instead, our analysis in this chapter is isolated to stage 3 of the adiabatic ramp, in which phase noise dynamics undergo a dramatic change as the system moves from high to low integrability when the transverse field is reduced. Going further, we also modify the stage 3 adiabatic ramp to begin from $\Omega/V_{dd} = 1.0$ as opposed to the starting point of $\Omega/V_{dd} = 0.6$ used in the original protocol throughout Chapter 4. Keeping the final value of the Rabi frequency the same at $\Omega/V_{dd} = 0.1$ we thus prolong the transition towards a more integrable Hamiltonian to study how this process affects noise.

Figure 5.1 demonstrates the key changes in the dynamics of the modified adiabatic ramp for stage 3. Firstly, Figure 5.1(a) plots instantaneous fidelity against the full range of Ω/V_{dd} for simulations with no phase noise, and for a variety of evolution times. We begin by initializing in the ground state of the initial Hamiltonian of our modified ramp with laser parameters $\Omega/V_{dd} = 1.0$ and $\delta/V_{dd} = 1.1$. Simulations with no laser phase noise reveal that the main loss of fidelity due to diabatic excitation is now shifted to the middle of stage 3, coinciding with the critical region in the ground state energy gap that occurs at $\Omega/V_{dd} \approx 0.55$. Following this, Figures 5.1(b-d) provide simulations of ground state evolution with phase noise for the time independent Hamiltonians occurring at the beginning, middle, and towards the end stages of the ramp. Unlike diabatic excitation, phase noise excitation is shown to be strongest in the first half of the adiabatic ramp when the transverse field is high and the Hamiltonians are most non-integrable. For a long evolution time of $TV_{dd} = 400$ simulations at $\Omega/V_{dd} = 1.0$ and $\Omega/V_{dd} = 0.6$ result in considerable excitation with final ground state fidelities of 55.0%, and 73.3% respectively. Moreover, we once again observe a distinct excitation profile of equidistant peaks corresponding to states with dominant transition rates and a high separation in the energy spectrum that allow energy to reach higher energy sectors. However, as was shown in previous analysis in Figure 4.6, below $\Omega/V_{dd} = 0.6$ the energy landscape begins to undergo dramatic changes as energy states begin to cluster together, and transition rates between them are suppressed, especially for eigenstates with large energy gaps. As a consequence, the final ground state fidelity of time independent Hamiltonian with $\Omega/V_{dd} = 0.1$ remains at 90.3%, as phase noise finds it much harder to excite the system.

The following chapters will use the adiabatic ramp defined in this section to study if a closed system under environmental noise, such as a Rydberg chain driven by a noisy laser, can act as an effective thermal bath when absorbing added energy.

5.2 The eigenstate thermalization hypothesis

For systems that relax to a thermal equilibrium, the underlying mechanism is most robustly described by the eigenstate thermalization hypothesis (ETH) [108, 200, 214, 215]. The ETH states that nonintegrable systems (that do not exhibit many-body localization [216, 217]) with non-degenerate energy eigenstates $|E_\alpha\rangle$, have a broad class of operators $\hat{A}$ for which expectation values $A_{\alpha\alpha} = \langle E_\alpha|\hat{A}|E_\alpha\rangle$ converge in the long time limit to values predicted by thermal ensembles, where they fluctuate negligibly around $|E_\alpha\rangle$ that are close to the energy of the system. Crucially, the hypothesis also presumes that $\hat{A}$ is 'well behaved', in that $A_{\alpha\alpha}$ behaves smoothly as a function of $|E_\alpha\rangle$, with no sudden discontinuities in the vicinity of the expected energy that would create a sensitivity to slight changes in relaxation dynamics. In the thermodynamic limit, the resulting state should be constant in time and be predictable by the total energy of the system. Thus, the individual eigenstate or cluster of eigenstates to which represent the converged expectation value can be thought of as an independent thermal state. Given these conditions, the ETH predicts that the long-time (LT) expectation value of a few-body operator $\hat{A}$ with an eigenstate $|E_\alpha\rangle$ of a many-body system Hamiltonian $\hat{H}$ with corresponding well-defined total energy E_α is equal to the thermal ensemble $\langle\hat{A}\rangle_{\text{Therm}}(E_\alpha)$ of $\hat{A}$ at a mean energy E_α

$$\langle E_\alpha|\hat{A}|E_\alpha\rangle_{LT} = \langle\hat{A}\rangle_{\text{Therm}}(E_\alpha). \tag{5.1}$$

Hence, the ETH provides a framework for comparing expectation values which are directly dependent on initial conditions to thermal ensembles which instead depend only on the total energy of the system. This implies a universal equilibrium for a thermalizing system across many trajectories of equivalent energy.

It will be necessary to define what is meant by a long-time average in Eq. (5.1). In the Heisenberg picture, the state $|\psi\rangle$ is time-independent, and the dynamics are carried by the operator $\hat{O}(t) = e^{i\hat{H}t}\hat{O}(0)e^{-i\hat{H}t}$. Expanding the expectation value in the energy eigenbasis $\{|E_n\rangle\}$, we obtain:

$$\langle\psi|\hat{O}(t)|\psi\rangle = \sum_n c_{nn}O_{nn} + \sum_{n\neq m} c_{nm}e^{i(E_n-E_m)t}O_{nm}, \tag{5.2}$$

where $O_{nm} = \langle E_n|\hat{O}(0)|E_m\rangle$ are the static matrix elements of the operator at $t = 0$. The coefficients $c_{nm} = \langle\psi|E_n\rangle\langle E_m|\psi\rangle$ are time-independent constants determined by the initial preparation of the system. The off-diagonal terms ($n \neq m$) represent the dynamical fluctuations of the observable. For non-integrable systems, the phase factors $e^{i(E_n-E_m)t}$ lead to dephasing over sufficiently long times. The long-time average is then formally defined by the diagonal ensemble:

$$\langle \hat{O} \rangle_{LT} = \lim_{T\to\infty} \frac{1}{T} \int_0^T \langle \psi | \hat{O}(t) | \psi \rangle dt = \sum_n c_{nn} O_{nn}, \tag{5.3}$$

where the time-averaging procedure eliminates the oscillatory off-diagonal contributions. Any dynamics in a quantum system leads to non-zero values of c_{nm} that represent fluctuations in the expectation value as a function of time and energy difference. The time it takes for the off-diagonal term with values of c_{nm} to die down drops with increasing system size, but for small and intermediate systems with large energy gaps this can be too long to measure or even simulate. Still, for non-integrable systems with minimal degeneracies in energy states these correlations do die down eventually, and numerically it is straightforward to evaluate long-time averages directly by considering only the diagonal ensemble at the end of a simulation.

To fully understand ETH fully it is also important to define the thermal ensemble $\langle \hat{A} \rangle_{\text{Therm}}(E_\alpha)$. In statistical mechanics the thermal equilibrium of a dynamical system is defined in terms of the Boltzmann distribution normalized by a partition function $Z = \sum_n \exp(-\beta E_n)$ where β is the thermodynamic temperature of the system. An ensemble of available energy states is then scaled by the thermodynamic temperature β which can be calculated using the total energy of the system. Adapting this to the Dirac notation, we define the canonical ensemble as

$$\langle \hat{A} \rangle_{\text{canon}} = \frac{1}{Z} \sum_n \exp(-\beta E_n) \langle E_n | \hat{A} | E_n \rangle, \tag{5.4}$$

where we sum over all the energy eigenstates $|E_n\rangle$. Previous work has shown that for closed systems, such as the one discussed in this thesis, the canonical ensemble is not always representative of final equilibrium [218]. In such finite systems thermalization occurs when energy in a small neighborhood of eigenstates uses the rest of the eigenstates as a thermal reservoir to dissipate into. Since the reservoir itself is not infinite, we see finite-size effects which become more prevalent at smaller system sizes. Instead, thermalization in these isolated quantum systems is typically discussed in terms of the microcanonical ensemble which considers only a small shell of energies, equally weighted and centered around the expected energy. Nevertheless, this approach is highly dependent on the density of states around the average energy of the system. The exact size of the energy shell should be small in comparison to the energy scale of the system, but large enough to include a statistically significant number of energy eigenstates. Relaxation to the microcanonical ensemble is therefore more readily observed in the middle of the energy spectrum, and for larger system sizes, where gaps between energies narrow down and density of states is higher [23]. The lower part of the energy spectrum, which dominates in adiabatic state preparation, usually exhibits a much lower density of states, leading to nonsensical microcanonical averages as very few or even no eigenstates fall within the vicinity of a given energy shell. The following section will discuss evaluating thermalization in the case of adiabatic state preparation in a Rydberg spin chain, motivating the choice of the canonical ensemble as the preferred distribution with which to evaluate the ETH.

5.3 Phase noise thermalization in the adiabatic state preparation

The main goal of this chapter is to investigate thermalization of laser phase noise energy in the adiabatic state protocol discussed in Section 5.1. To do this we first introduce a simple method of estimating the thermodynamic temperature for a given quantum system, which can then be used to evaluate the canonical ensemble defined in 5.4. Following this, we also define explicitly the antiferromagnetic (Z_2) order parameter and interaction energy observables, discussing their behavior as a function of energy by projecting them across the entire energy spectrum. The resulting spectra will be weighted by the diagonal and microcanonical ensembles to generate long-time and thermal expectation values that can be compared to evaluate thermalization directly; performing this calculation for different system parameters and adiabatic evolution times allows for an in depth analysis of this phenomenon.

5.3.1 Evaluating thermalization

In the case of adiabatic state preparation with experimentally relevant levels of phase noise, a comparatively small amount of energy is added to the system. This means that the dynamics will be mainly contained in the low energy spectrum where the microcanonical average is not well defined, limiting the analysis to the canonical ensemble. A value for thermodynamic temperature β of a quantum system at a given energy can always be calculated by solving the equation

$$\langle\psi|\hat{H}|\psi\rangle = \frac{1}{Z}\sum_n \exp(-\beta E_n)\langle E_n|\hat{H}|E_n\rangle, \tag{5.5}$$

where $|E_n\rangle$ and E_n represent the n^{th} eigenstate and its corresponding energy, and $|\psi\rangle$ represents the state of the system. The left hand side of the equation calculates the system energy using the Hamiltonian operator $\hat{H}$, leaving β as the only unknown. Once a value for β is determined it can be used in Eq. (5.4) to evaluate arbitrary thermal expectation values at the appropriate energy. In the case of adiabatic state preparation, we consider the final energy by taking $|\psi\rangle$ at the end of the adiabatic state preparation. Given that phase noise has the potential for exciting across the full energy spectrum it is important to access the full Hilbert space, meaning that we limit ourselves to a system size of 11 sites which can be completely diagonalized.

The next step in evaluating thermalization is choosing the appropriate observables for the system in question. As was discussed in the beginning of the chapter, the choice of observables stems around the feature of long-range interaction that is intrinsic to Rydberg atom systems due to the Rydberg blockade interaction. We define the interaction operator $\hat{H}_{\text{int}}$ explicitly by isolating the interacting term from the TFIM defined in Eq. (4.2) as

$$\hat{H}_{\text{int}} = V_{dd}\sum_{k,l>k}^{N} \frac{\hat{n}_k\hat{n}_l}{|k-l|^3}, \tag{5.6}$$

in which a dipole-dipole potential V_{dd} is mediated by $\hat{n}_k\hat{n}_l$ interactions that enforce a Rydberg interaction penalty on neighboring excitations, and indices k and l label interacting sites. Physically, this observable tracks the energy cost of Rydberg interactions which enforces a long-range constraint on excitation. When appearing in the full Hamiltonian, $\hat{H}_{int}$ sets the ground-state structure, and influences which configurations are energetically favorable. Another way of quantifying interactions is by looking at the long-range spin ordering that they induce. Given that the adiabatic protocol simulated in Chapter 4 performs a ground state preparation of a one-dimensional spin chain with Z_2 ordering, a natural choice for an observable is the the order parameter observable

$$\hat{O}_{Z_2} = \sum_{k,l\neq k}^{N} \sigma_z^k (-1)^{k+l} \sigma_z^l. \tag{5.7}$$

Physically, $\hat{O}_{Z_2}$ measures how close a given state is to the perfect Z_2 ordered spin chain by checking $\sigma_z\sigma_z$ anti-alignment over all different lattice sites k and l.

With two relevant observables defined in Eq. (5.6) and Eq. (5.7), as well as a method of estimating their thermal expectation value provided in Eq. (5.5), we are ready to evaluate thermalization. To do this we first simulate the adiabatic ramp for a variety of evolution times, measuring the final energy E_R of the prepared state $|\psi_R\rangle$ after a given adiabatic ramp and using it in Eq. (5.5) to get a value for β. The value of β can then be used directly in Eq. (5.4) to generate thermal expectation values of a given observable corresponding to the energy of the prepared state. Likewise, the probabilities $|c_{nn}|^2$ that make up the diagonal ensemble of the long-time expectation value can be directly calculated using the overlap $p_n = |\langle E_n|\psi_R\rangle|^2$. The energy distributions $\langle E_n|\hat{H}_{int}|E_n\rangle$ and $\langle E_n|\hat{O}_{Z_2}|E_n\rangle$ feature in both expectation value equations, and in the case of a fully diagonalizable Hamiltonian these can be pre-generated to save computational time.

5.3.2 Thermalization in an 11 site spin chain

In this section we analyze thermalization results for a small fully diagonalizable Rydberg spin chain of 11 sites. The goal is to find out weather thermal and long-time expectation values, for the two observables introduced in Section 5.3.1, converge for a variety of evolution times of the adiabatic ramp. The fact that accessing the full Hilbert space is computationally feasible allows for the calculation of true canonical and long-time ensembles, which is necessary given that during the non-integrable stages of the preparation phase noise excitations transfer energy even to the highest energy eigenstates (see Section 5.1). Furthermore, it is possible to plot energy distributions $\langle E_n|\hat{H}_{int}|E_n\rangle$ and $\langle E_n|\hat{O}_{Z_2}|E_n\rangle$, providing an idea of how smoothly the chosen operators vary as a function of energy. This smoothness in energy is a central requirement for ETH to hold, as non-linear behavior and

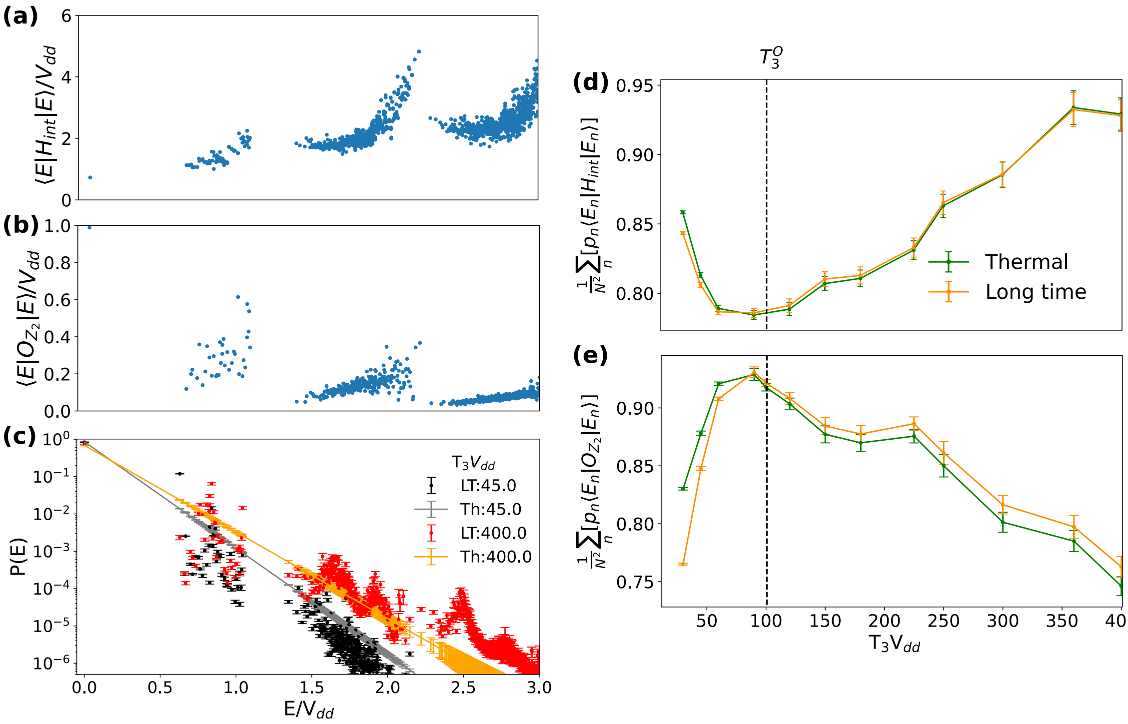

FIGURE 5.2: **Evaluating thermalization in $\sigma_z\sigma_z$ correlations and interaction energy**. **(a)** Interaction energy $\langle H_{int}\rangle$ defined in Eq. (5.6) and **(b)** $\langle\hat{O}_{Z_2}\rangle$ ordering parameter defined in Eq. (5.7) as a function of low energy eigenstates of the target Hamiltonian with $\Omega = 0.1V_{dd}$ and $\delta = 1.1V_{dd}$ in a one dimensional Rydberg spin chain with 11 sites. **(c)** Energy distributions $P(E)$ of the prepared state projected onto the long-time ensemble (LT) as defined in Eq. (5.3), and thermal ensemble (Th) as predicted by the canonical ensemble from Eq. (5.4), of the adiabatic ramp introduced in Section 5.1 with evolution times $\mathrm{T}_3V_{dd} = 45, 400$. Expectation values for **(d)** interaction energy H_{int} and **(e)** $\hat{O}_{Z_2}$ ordering for a variety of T_3, calculated by averaging over long-time and canonical energy distributions in **(c)** weighed by expectation value distributions in **(a)** and **(b)** respectively. A dashed line shows optimal T_3^O for maximum ground state fidelity of the prepared state. Energy is defined with respect to ground state energy and error bars show standard error over 100 preparations with distinct laser phase noise realizations.

sharp discontinuities mean that the observables are very sensitive to small changes in energy causing canonical and long-time expectation values to diverge.

Figure 5.2 provides all the distributions required to generate long-time and thermal expectation values as a function of energy relative to the ground state. Figures 5.2(a) and 5.2(b) show the two observables chosen for the comparison to be the interaction energy $\hat{H}_{int}$ as defined in Eq. (5.6), as well as a $\hat{O}_{Z_2}$ order parameter defined in Eq. (5.7) that measures long-range Z_2 ordering that is maximally represented in the ground state. Given the relatively small Rabi frequency $\Omega = 0.1V_{dd}$ at the end of the state preparation, we are investigating a Hamiltonian that is highly integrable, with structured energy levels that appear as regions of clustered eigenvalues (see Figure 4.6 in Section 4.5.1). Although neither of these observables vary smoothly as a function of energy as prescribed by the ETH, the energy distribution of H_{int} is visibly less scattered compared to that of the $\hat{O}_{Z_2}$ order parameter, meaning that small changes in the excitation energy should affect the expectation values of the latter more, leading to erratic behavior. The distributions as a function of eigenstate energy for H_{int} and the $\hat{O}_{Z_2}$ order parameter are then weighted by the diagonal and canonical ensembles.

Figure 5.2(c) provides example energy distributions of a final state after a short preparation of $T_3 V_{dd} = 45$ and a much longer preparation at $T_3 V_{dd} = 400$, projected onto the long-time and canonical ensembles. Practically speaking, the determining factors of thermalization will be: how well the uniform Boltzmann distribution with of the canonical ensemble (of an equivalent many-body energy) acts as a 'line of best fit' for the long-time distribution, and, at energies where these distributions disagree, how does the local behavior of the tested observable exacerbate or lessen the impact on the averaged expectation value. Moreover, since we are dealing with ground sate preparation, most of the energy will be held in the low-energy spectrum even after longer evolution times, meaning that the low-energy eigenvalues will have an out-sized impact on the final expectation values. The diagonal ensemble for the shorter evolution time of $T_3 V_{dd} = 45$ is dominated by diabatic excitation, with most excitation occurring to the first excited state appearing far above the canonical ensemble, while the majority of higher energy states are left largely unexcited, thus leaving them with a lower occupancy than is predicted by the canonical ensemble. This type of excitation is inherently non-thermalizing. For a much longer preparation of $T_3 V_{dd} = 400$ the first excited state drops far below the occupancy of the Boltzmann distribution, as diabatic excitation is suppressed. Instead, we see a general increase in occupancy across the entire energy spectrum, with a cohort of low energy eigenstates clustered within $E = 1V_{dd}$ from the ground state being most prominent. The irregular peaks that appear in the diagonal ensemble of the $T_3 V_{dd} = 400$ preparation form during the initial stages of the ramp where the non-integrability of the system leads to cascading equidistant excitation peaks across the entire Hilbert space (see Figures 4.7(b) and 5.1(b) for this mechanism). These peaks become distorted as the system changes to increasingly integrable in the latter half of the ramp, and dynamics become dominated by transition elements that are localized in energy and have much smaller transition rates. Notably, we see less excitation out of the ground state as in constant Hamiltonian evolution in Figure 5.1, as in a dynamical ramp with changing laser parameters the transition rates change dramatically, making excitation more distributed throughout the spectrum and less potent when the system becomes integrable. Clearly, in both the long and short ramps, the diagonal ensembles do not resemble the uniform exponential decay of the Boltzmann distribution, but given that thermalization is only measured through expectation values, it is their averaged behavior that matters.

Averaging over the operator distributions of Figures 5.2(a) and 5.2(b) weighted by the long-time and thermal ensembles of a particular T_3 results in a single expectation value. Figures 5.2(c,d) provide a comparison between thermal and long-time expectation values of $\hat{H}_{int}$ and the $\hat{O}_{Z_2}$ order parameter for a variety of T_3. The general relationship between both types of expectation value and time T_3 is roughly consistent with the results in Figure 4.4, as the optimal ramp time for this modified ramp coincides with the lowest interaction energy in the system and therefore the highest fidelity with the Z_2 ordered ground state. For durations shorter than the one corresponding to the optimal fidelity (shown as a dashed line in Figures 5.2), where diabatic excitation dominates, we see a clear divergence between the long-time and thermal expectation values. The cause of this divergence can be seen in Figure 5.2(c), which shows that for the shorter preparation time of $T_3 = 45tV_{dd}$ a majority of energy eigenstates have occupancy probabilities below the Boltzmann distribution. The dashed line labeled T_3^O marks the evolution time corresponding to the lowest energy added to the system, long enough for diabatic excitation to subside but too short for notable dephasing to occur (see Chapter 4 Figure 4.4). At this point, not enough energy is added to the system to differentiate the thermal and long time expectation values. However, as the duration of T_3 passes its optimum, and laser phase noise begins to dominate excitation, we see convergence of the long-time and thermal expectation values persist. In the case of H_{int} the convergence is strong as soon as $T_3V_{dd} = 60$ up until $T_3V_{dd} = 400$. In the case of the $\hat{O}_{Z_2}$ order parameter, a similar divergence of the two expectation values occurs at short T_3, along with the expected convergence around the optimal time. For longer T_3, the expectation values for this parameter behave more erratically, as can be expected given the large variance of the operator as a function of energy seen in 5.2(b). Despite this, there is still good convergence between the thermal and long-time expectation values for the $\hat{O}_{Z_2}$ operator, even though expectation values consistently appear above thermal predictions, suggesting disproportionate excitation into states with some Z_2 ordering. A possible reason for this is that the ground state throughout the adiabatic ramp is also predominantly Z_2 ordered, making excitation into states with some Z_2 ordering more probable than into completely disordered states.

In Sections 4.5.4, 4.5.3, and 5.1 we show that due to a change in integrability, phase noise excitation is considerably more prominent when Ω/V_{dd} is higher. In such cases when integrability is sufficiently broken, and the phase noise is given enough time, the transitions that are highly delocalized in energy dominate excitation and form energy peaks across the entire spectrum. However, by the end of the state preparation when Ω/V_{dd} decreases and the Hamiltonian becomes integrable, these excitation peaks become distorted as energy eigenstates shuffle into tightly packed clusters separated by large energy gaps. There is an overall drop in transition probability as highly delocalized excitations disappear, limiting the energy mobility around the system to the local excitation of neighboring eigenstates shown in Figures 4.7(d), 4.8(d), and 5.1(d). The combination of delocalized excitation that facilitates rapid energy transfer in the first half of the ramp and the suppressed localized excitation of this transferred energy in the latter half seems to excite the system in a way such that averaged behavior is very close to the uniform predictions of the Boltzmann distribution, albeit by comparing distributions that differ considerably. In this way, we can say that the adiabatic state preparation 'facilitates' the convergence of the long-time and thermal ensemble, and the resulting expectation values appear to thermalize.

The continuous transition from integrable to non-integrable is necessary for the thermalization observed in Figure 5.2(d,e), as the constant reshuffling of energy eigenstates and changing behavior of phase noise excitation ensures that there is no concentration of excitation in any particular energy sector but the energy is roughly equally distributed. Figure 5.3 shows the evolution of the $\hat{H}_{int}$ expectation value when phase noise is added to two time independent Hamiltonians that occur at the beginning and end of the adiabatic ramp. When phase noise is left uncontrolled in a non-integrable regime, as is the case for the initial Hamiltonian of the adiabatic ramp shown in Figure 5.3(a), it leads to the formation of excitation peaks previously shown in Figure 5.1(b,c). As the Hamiltonian is constant, the phase noise has access to the same excitation profile throughout the whole evolution, exciting dominant transition elements that have large energy gaps. This

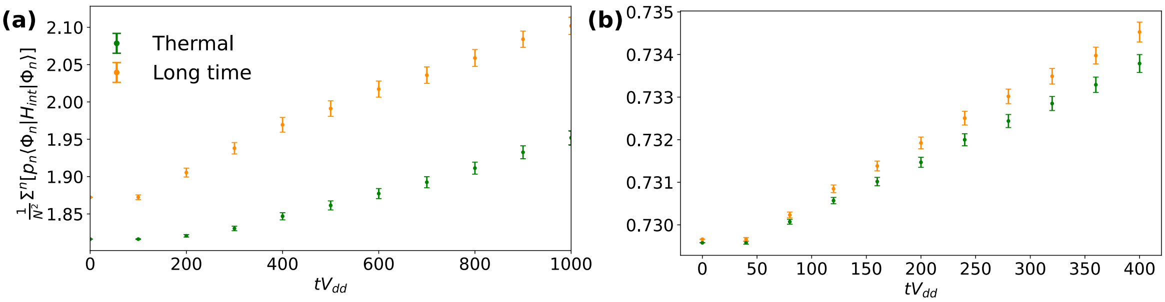

FIGURE 5.3: **Long-time and thermal expectation values for ground state evolution of a constant Hamiltonian with added laser phase noise**. **(a)** Thermal and long-time expectation values for constant Hamiltonian with parameters $\Omega = 1.0V_{dd}$ and $\delta = 1.1V_{dd}$ for a total evolution time $T_3V_{dd} = 1000$. **(b)** Thermal and long-time expectation values for constant Hamiltonian with parameters $\Omega = 0.1V_{dd}$ and $\delta = 1.1V_{dd}$ for a total evolution time $T_3V_{dd} = 400$. The variable n provides the index across all energy eigenvalues summed in the calculation, weighted by p_n which are the probabilities associated with either the thermal or long time probability distributions. Error bars show standard error in occupancy after 100 independent noise realizations.

facilitates energy transfer from the ground state to states that would be otherwise energetically unfavorable with a higher H_{int}, representing configurations that are similar to the ground state but with added blockade violations that phase noise excitation can overcome. The result is expectation values that do not thermalize with increasing evolution time, but instead have long-time expectation values that grow faster than predicted by the canonical ensemble as energy flows into states with high transition rates as opposed to all states uniformly. This process is slower for the final Hamiltonian of the adiabatic ramp shown in Figure 5.3(b), where evolving in a regime that is close to integrable leads to much less total energy transfer, with more localized excitation inhibiting the uniform excitation of the full energy spectrum. In this case, the divergence is considerably more gradual, but because the dephasing excitation paths still seem to favor states with higher H_{int}, the outcome remains the same.

Nevertheless, this interplay between integrability and thermalization is governed entirely by a complicated dynamical energy structure of the Hamiltonian and its response to random phase fluctuation, and even though we do observe a persisting thermal behavior for this 11 site system, just how robust this is to changes in system parameters is an open question. To explore some potential avenues of this question the following section s test the fragility of the thermalization observed in Figure 5.2 first when long-range interactions are removed, and then for larger system sizes.

5.4 Thermalization for nearest neighbor interactions

Long-range interactions play an important role in the non-equilibrium dynamics and thermalization behavior of Rydberg atom arrays, where the presence of dipole-dipole or van der Waals interactions that decay algebraically with distance introduce complex many-body correlations that span the entire system. In the context of Rydberg arrays in the TFIM, such long-range couplings further degrade integrability by increasing available energy configurations and thus the density of states. Such non-integrability increases the number of resonant transitions and helps transport noise excitations across the entire system which should improve thermalization in theory. In Section 5.3.2 we demonstrated a relationship between thermalization and the adiabatic state protocol which dynamically changes both the energy structure and susceptibility to dephasing, facilitating a more uniform distribution of energy. However, it is unclear how fragile such a complicated relationship is, and if long-range interactions play a key role in preserving the balance. To this end, this Section provides the same analysis done in Section 5.3.2 for a Hamiltonian that is limited to nearest neighbor interactions

$$\begin{aligned}\hat{H}_R = \quad & \frac{\Omega(t)}{2}\sum_{k=1}^{N}\left[e^{-i\phi(t)}|0\rangle_k\langle 1|_k + e^{i\phi(t)}|1\rangle_k\langle 0|_k\right] \\ & - \delta(t)\sum_{k=1}^{N}\hat{n}_k + V_{\mathrm{dd}}\sum_{k=1}^{N-1}\hat{n}_k\hat{n}_{k+1}, \end{aligned} \tag{5.8}$$

To begin with, Figure 5.4 provides a comparison for the diagonal ensemble of the same adiabatic state preparation with a long evolution time, done on systems with nearest neighbor and long-range interactions (the latter also features in Figure 5.2(c)). The model with only nearest neighbor interactions has experienced slightly less overall excitation, as evidenced by the final ground state fidelity of $F = 0.753$ compared to the final fidelity $F = 0.733$ for the system with long-range interactions. The suppressed excitation in the nearest neighbor system leads to less defined excitation peaks, and slightly less excitation in the highest energy eigenstates. However, the low energy eigenstates that dominate excitation dynamics

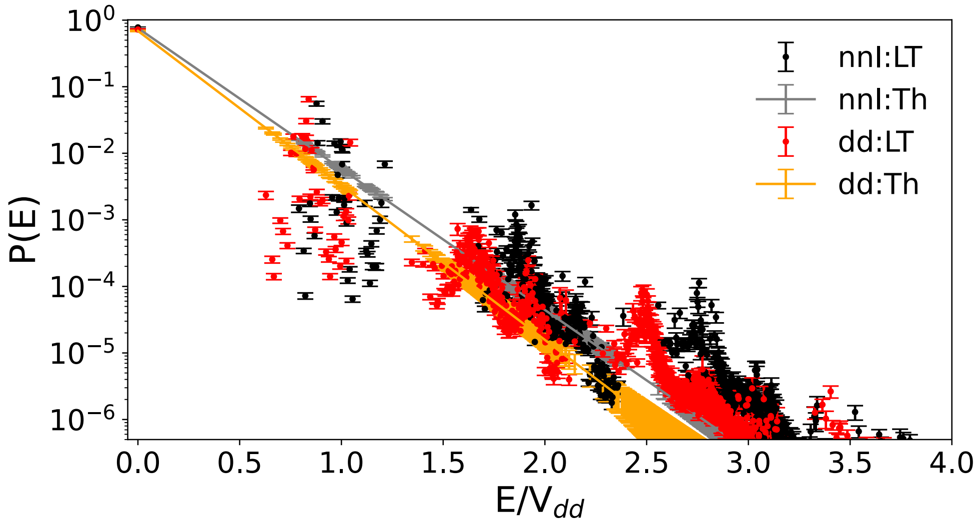

FIGURE 5.4: **Diagonal ensembles for noisy adiabatic state preparations with and without long-range interactions**. Side by side comparison of long time (LT) and canonical (Th) probability distributions after a noisy adiabatic state preparation with an evolution time of $T_3 = 400tV_{dd}$ with only nearest neighbor interactions (black, grey) and long-range interactions (red, yellow) (seen also in Figure 5.2(c)).Error bars show standard error in occupancy after 100 independent noise realizations.

are not dramatically different in the two systems. Given the fact that thermalization evaluates only the averaged behavior, the minimal difference between the two systems when considering the number of eigenstates with occupancy probabilities above and below the canonical ensemble suggests that thermalization properties do not vary dramatically.

In Figure 5.5 we show the energy distributions of observables $\langle E|\hat{H}_{int}|E\rangle$ and $\langle E|\hat{O}_{Z_2}|E\rangle$ weighted by the diagonal and canonical ensembles to generate thermal and long-time expectation values for adiabatic state preparations with a variety of ramp times T_3 in a system with only nearest neighbor interactions. As an example, the diagonal ensemble shown in Figure 5.4(a) is combined with energy distributions in Figures 5.5(a,b) to generate the probability distributions in Figures 5.5(c,d) that are averaged to generate an expectation value in Figures 5.5(e,f) corresponding to the time $T_3V_{dd} = 400$. Immediately, we can see that the two observables tell a different story, with thermalization preserved in the $\hat{O}_{Z_2}$ operator, but signs of divergence in the $\hat{H}_{int}$ operator as the long-time expectation value deviates from the thermal prediction and rises above it. One reason for this is the stark difference in the behavior of $\langle E|\hat{H}_{int}|E\rangle$ for the nearest neighbor interacting system in comparison to its long-range counterpart seen in Figure 5.2(a). In the absence of integrability-breaking long-range interactions the energy landscape is much more

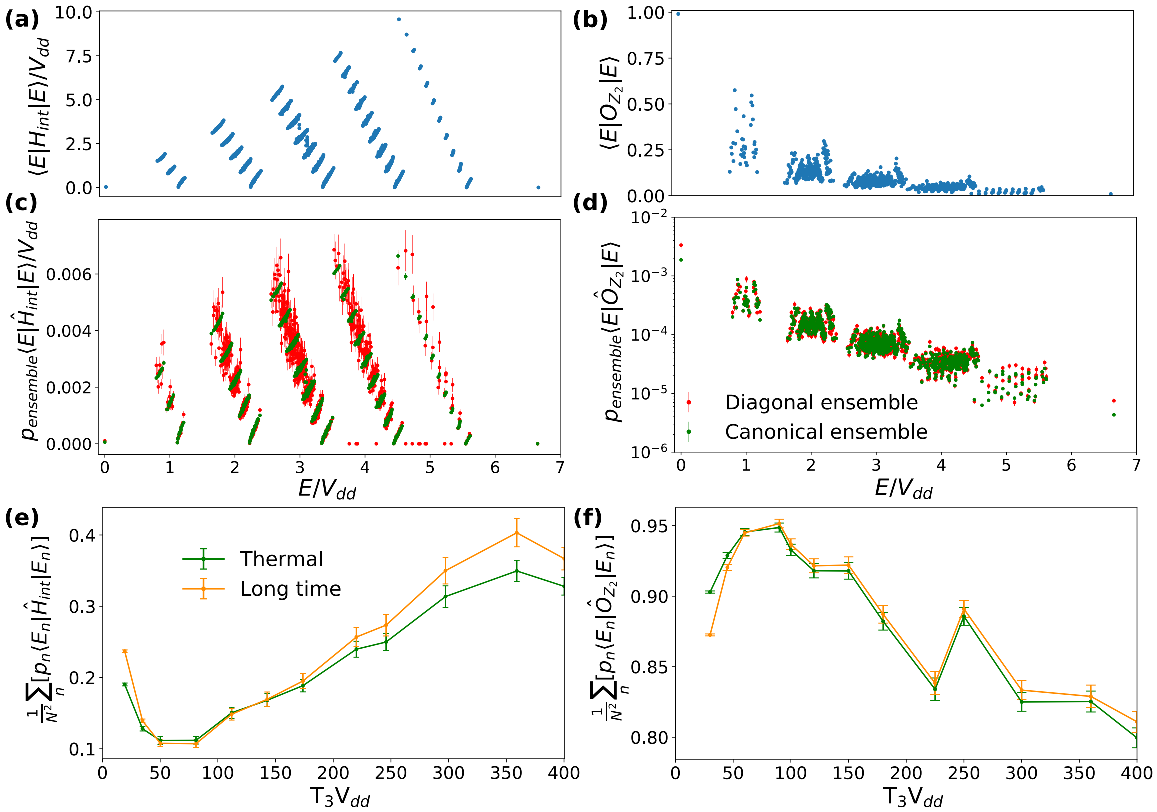

FIGURE 5.5: **Generating expectation values for $\hat{H}_{int}$ and $\hat{O}_{Z_2}$ in a system with nearest neighbor interactions**. **(a,b)** Distributions of $\langle E|\hat{H}_{int}|E\rangle$ and $\langle E|\hat{O}_{Z_2}|E\rangle$ across all energy eigenstates of a system with only nearest neighbor interactions. **(c,d)** The same energy distributions as weighted by diagonal and canonical ensembles after an adiabatic state preparation with a total ramp duration of $T_3V_{dd} = 400$. **(e,f)** Long-time and thermal expectation values for $\hat{H}_{int}$ and $\hat{O}_{Z_2}$ after averaging across weighted energy distributions, and for a variety of ramp times T_3V_{dd} .All error bars provide standard error after averaging across 100 unique noise realizations.

structured, with a large number of conserved quantities that lead to degeneracies and highly segregated clusters of energy states.

The probability distributions in Figure 5.5(c,d) are attained by weighting the highly non-linear energy distribution with the diagonal and canonical ensembles in Figure 5.4(a). As expected from a system following the ETH, these distributions reveal that, despite constant total energy and general agreement in the final expectation values, the energy added into the system with phase noise does not present itself with exponential decay expected by the canonical ensemble. Instead, we see disproportionate excitation to states with higher interaction energy that exhibit a larger number of violations of the Z_2 ordering. This is possible because most of the excitation occurs in the initial stages of the ramp, where the ground state is not a well defined Z_2 ordered state, but rather a constantly changing mix of disordered configurations with an ever increasing Z_2 ordered component. At first, the instantaneous ground state is coupled to high energy states with high transition rates (see Figure 4.7(c)), but by the time we make our measurements on the final Hamiltonian the system is integrable and all the excitation that occurred in the initial stages appears very energetically unfavorable. Such states display not only higher occupancy probabilities but also larger standard errors suggesting considerable variability in the excitation pattern across different noise realizations. This is in contrast with states with low interaction energy that are either in consistent agreement with the canonical prediction or are left completely unexcited. This shows the propensity of dephasing noise to induce excitations along the chain that would otherwise be energetically unfavorable, underscoring how noise-induced excitation bypasses the typical energetic constraints of adiabatic evolution. The corresponding averaged behavior in Figure 5.4(c) thus shows the long-time expectation value skewing towards a higher interaction energy in comparison with the thermal prediction as the evolution time increases and the dephasing has more time to accumulate.

In the case of the $\hat{O}_{Z_2}$ operator, thermalization seems robust even when long-range interactions are removed. The first important element to this result is seen in Figure 5.5(b) where $\langle E_n|\hat{O}_{Z_2}|E_n\rangle$ is largest for the ground state which is completely Z_2 ordered, as well as the first two clusters of low energy eigenstates after which there is a consistent drop off in Z_2 ordering and excitation has little impact on the final expectation value. Thus, the final expectation value will depend on the average probability distribution across the low energy eigenstates when $\langle E_n|\hat{O}_{Z_2}|E_n\rangle$ is weighted by the diagonal and canonical ensembles in Figure 5.5(c). The largest discrepancy between the diagonal and canonical probability distributions is seen in the ground state, which is considerably more occupied in the diagonal ensemble than in the canonical, which assumes uniform Boltzmann distribution. Given the sustained agreement of the resulting long-time and thermal expectation values in Figure 5.5(f), the ground state discrepancy must be compensated by the rest of the energy eigenstates for which the majority of states have a diagonal ensemble occupancy that is either similar to or below its canonical counterpart. We conclude that thermalization is maintained by the competing effects: the first is less overall excitation due to the absence of long-range interactions, which maintains a disproportionate occupancy in the Z_2 ordered ground state, and the second is the fact that phase noise excitation skews towards eigenstates with a high $\langle E_n|\hat{H}_{int}|E_n\rangle$ that do not exhibit long-range Z_2 ordering.

In summary, the comparison between systems with and without long-range interactions reveals that while long-range couplings increase excitation and may promote thermalization through enhanced connectivity in Hilbert space, they also introduce additional pathways for dephasing-induced excitation. The removal of these interactions leads to reduced overall excitation and a more structured energy landscape, which limits the spread of noise and may also inhibit full thermalization of some observables. Interestingly, the $\hat{O}_{Z_2}$ order parameter shows robust thermalization behavior even in the absence of long-range interactions. In contrast, the interaction energy observable $\hat{H}_{\text{int}}$ deviates from thermal predictions, reflecting the highly disordered nature of phase noise excitations. These results demonstrate the nuanced role of long-range interaction in balancing excitation dynamics, thermalization, and the fidelity of quantum state preparation protocols.

5.5 Thermalization and system size

The final topic addressed in this chapter is the relationship between thermalization, long-range order, and system size. We again consider the $\hat{O}_{Z_2}$ order parameter for the final state of an adiabatic state preparation in a one-dimensional Rydberg chain. Due to the computational complexity arising from the exponential growth of the Hilbert space with system size, the simulations presented in this section are performed using matrix product state (MPS) techniques. Thermal state approximations are obtained using the finite-temperature methods described in Section 3.3. While this approach allows for accurate simulations of significantly larger systems, full diagonalization remains impossible and techniques such as DMRG primarily provide access to ground-state properties, rendering much of the Hilbert space inaccessible. This means that the kind of ensemble analysis performed in Sections 5.3 and 5.4 cannot be performed, and the analysis will be limited to comparing the expectation value of the final prepared state to the approximate thermal state of the same energy. Furthermore, given that the diagonal ensemble and therefore the long-time average can no longer be calculated, we attempt to mitigate any quantum correlation by allowing the system to evolve at constant energy for a fixed time of $tV_{dd} = 16$ after the adiabatic state preparation, averaging out any oscillatory behavior in the expectation value.

Figure 5.6 provides a direct comparison of expectation values of the $\hat{O}_{Z_2}$ order parameter for both adiabatic and thermal states of equivalent energy. Much like

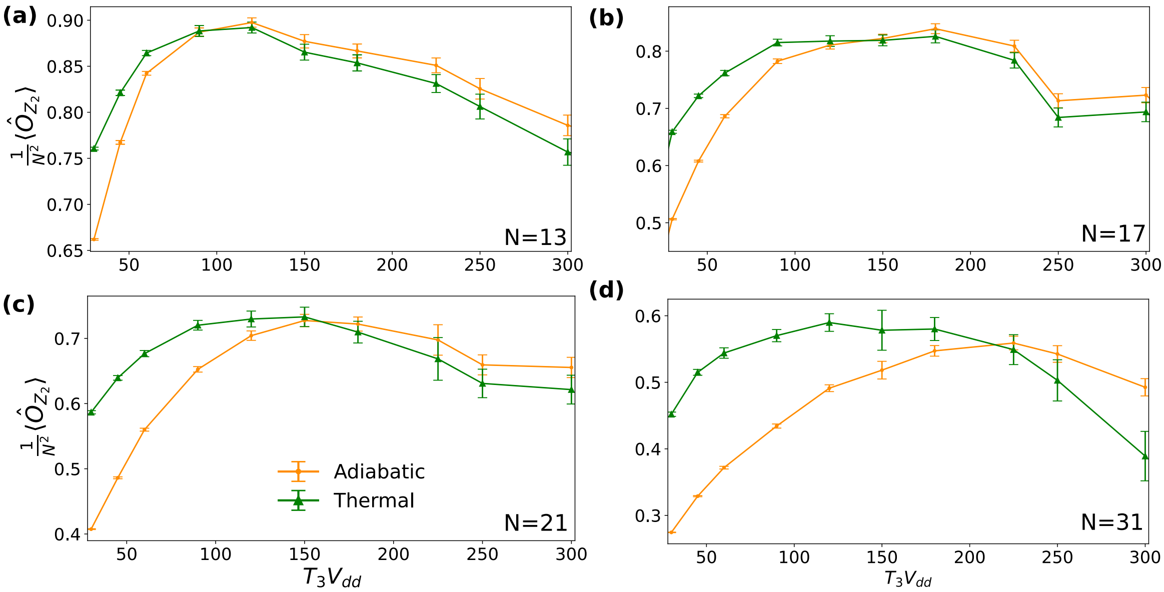

FIGURE 5.6: **Thermalization of $\hat{O}_{Z_2}$ after adiabatic state preparation in a Rydberg spin chain as a function of system size**. Expectation values for the $\hat{O}_{Z_2}$ order parameter as defined in Eq. (5.7) for the final prepared state after an adiabatic state preparation (yellow) and an approximated thermal state (green) of the same energy. Expectation values are shown for a variety of ramp times T_3V_{dd} and for system sizes of $N =$ **(a)**13, **(b)**17, **(c)**21, **(d)**31 sites. Error bars show standard error after 100 unique noise realizations.

in the case of the 11 site system analyzed in Sections 5.3 and 5.4 there is no thermalization for shorter ramp times, during which phase noise does not have time to accumulate and energy in the system is primarily added through diabatic excitation. However, there is an increase in the value of T_3 around which thermal and adiabatic expectation values begin to agree, taking approximately $T_3V_{dd} = 90$ in the case of $N = 13$ sites and approximately $T_3V_{dd} = 225$ in the case of $N = 31$. This finding is consistent with final fidelity plots provided in Chapter 4.4 and Figure 4.4(b), where optimal fidelity was found occur at the ramp time that minimized both diabatic and dephasing excitations. More interesting however is the comparison after this turning point, when accumulated noise dominates excitation and leads to a gradual loss of ground state fidelity and therefore a drop in the $\hat{O}_{Z_2}$ order parameter. Despite the erratic behavior in expectation values of longer ramp times, the energy added into the system by laser phase noise leads to sustained thermalization for smaller system sizes. However, despite some remaining within standard error we see a systematic lack of thermalization for the larger system sizes as N grows. This is most pronounced in the case of $N = 31$ where thermal and adiabatic predictions decouple.

A speculative reason for the lack of thermalization in large system sizes could be that, because of the larger density of states and smaller energy gaps between states, the larger the system size the less time it takes for a rapid excitation to states with high transition rates in the initial non-integrable stages of the ramp (as seen in Figure 5.1 for 11 sites). Since the latter stages of the ramp are in an integrable regime where excitation is subdued and excited energy becomes 'locked' in place, if this energy transfer is too fast the resulting long-time ensemble will be much more skewed towards specific resonant high energy sectors which, when over-excited, ruin the tenuous balance that makes the average behavior agree with the canonical ensemble. Essentially, there is a window during which the long-time and canonical ensembles agree, governed by the time it takes to minimize the inherently non-thermal diabatic excitation on one side and the speed at which the system gets excited in the non-integrable regime. The larger the system size, the narrower this window becomes, and by 31 sites we can see that when diabatic excitation is minimized and phase noise excitation becomes the dominant noise source the long-time and canonical ensembles begin to diverge once again.

Interestingly, across all system sizes where the adiabatic expectation value follows the thermal approximation within the given standard error, the long-time expectation value is also consistently the highest of the two expectation values. This behavior was also observed for the $N = 11$ sites in Figure 5.4 which was derived using exact diagonalization, and the agreement between a variety of system sizes and two different numerical methods suggests that the underlying excitation mechanisms remain the same. Although this phenomenon was not studied in depth, for the 11 site systems in Figure 5.2(c) and 5.4 all have the ground state occupancy appearing above the canonical prediction, as energy is shared between the ground state and a few energy sectors with high transition rates as opposed to being equally Boltzmann distribution across all eigenstates. This leads to slightly more representation in the Z_2 ordered grounds state that would be expected in a thermal equilibrium, leading to consistently higher values in $\langle \hat{O} \rangle$ for the prepared state rather than the thermal state.

5.6 Summary

The focus of this chapter was to investigate thermalization properties of laser phase noise induced excitation in the context of a well known many-body Rydberg experiment of adiabatic state preparation. We investigate how interaction range, system size, and observable choice influence long-time behavior and how this compares with the thermal predictions. Building on the groundwork laid in Chapter 4, where the effect of phase noise on the performance of the adiabatic protocol was explored, this chapter transitioned from analyzing final state fidelity to the thermal properties of the energy added to prepared states.

After an introductory discussion on the eigenstate thermalization hypothesis (ETH) in Section 5.2, we discuss a change of interaction regimes in 5.1, moving the dynamics of the system closer to resonance with the generated phase noise, as the simulations performed in this chapter are geared solely towards measuring noise rather than adiabatic performance. Section 5.3 began the analysis using the diagonal and canonical ensembles as tools to evaluate whether adiabatic state preparation with realistic dephasing leads to thermalization. Simulations were performed on a fully diagonalizable system of $N = 11$ atoms featuring long-range interactions, where ensemble averaging allowed for direct comparisons of thermal and long-time expectation values. The two observables chosen for this analysis were the interaction energy $\hat{H}_{int}$ and the Z_2 order parameter $\hat{O}_{Z_2}$ due to their close relationship to long-range interaction. The results demonstrated that, given the variation rates of the laser parameters are slow enough to minimize diabatic excitation, accumulated phase noise gradually drives the system into a perceived thermal equilibrium, where expectation values of the long-time ensemble agree with the statistical mechanical predictions of the canonical ensemble. This was found to occur despite excitation mechanisms that are highly non-uniform and depend on the underlying energy structure of the many-body Hamiltonian as well as the power spectral structure of the noise.

To isolate the role of long-range interactions in this process, Section 5.4 repeated the same thermalization analysis for a modified TFIM Hamiltonian constrained to nearest-neighbor interactions. In contrast to the long-range case, this system exhibited a more structured and degenerate energy spectrum, leading to suppressed overall excitation. While thermalization of the $\hat{O}_{Z_2}$ order parameter remained robust, significant deviations were observed for the interaction energy $\hat{H}_{int}$, which skewed away from thermal predictions. This was attributed to the structured nature of the energy eigen-basis, which prevented uniform distribution of noise-induced excitations. In particular, phase noise preferentially excited states with high interaction energy and numerous blockade violations, breaking the thermal equilibrium prediction of uniform energy spreading. The results revealed a nuanced interplay: while long-range interactions enhance overall excitation and help distribute energy and promote thermalization, they also break degeneracy and provide more pathways for excitation, whereas nearest-neighbor models limit overall excitation and concentrate it towards states with larger interaction energies.

The final section of this chapter, Section 5.5, explored the impact of system size on thermalization by extending simulations to larger chains using matrix product state (MPS) methods. Here, exact diagonalization was no longer feasible, and thermal behavior was assessed by comparing the expectation value of the final state to that of a thermal state of equivalent energy. Simulations agreed with analysis in Section 4.4 in which short ramps result in diabatic excitation and prevent thermalization, while longer ramps dominated by accumulated phase noise produced expectation values that agreed with thermal predictions. The results also revealed a size-dependent delay in the onset of thermal behavior, consistent with the competition between diabatic and dephasing excitation discussed broadly in Chapter 4. Notably, the Z_2 order parameter $\hat{O}_{Z_2}$ again displayed some level of convergence to thermal values across all system sizes studied except the largest and $N = 31$. For smaller system sizes this convergence was consistent with results from the $N = 11$ exact diagonalization analysis, suggesting a consistent mechanism underpinning noise-induced thermalization. Although eigenvector analysis is impossible for the largest system, we reason that clear loss of thermalization could be caused by increased non-integrability throughout the adiabatic ramp that leads to an energy spectrum highly delocalized energy peaks that do not approach thermalization.

Together, these findings provide insight into many-body thermalization of laser phase noise in Rydberg quantum systems. Thermalization is studied in the context of adiabatic state preparation which is a foundational protocol in quantum simulation, with two standard observables which probe long-time equilibration in interaction energy and long-range ordering. We also compare the effect of removing long-range interactions, as well as changing system size to see how such system parameters influence whether and how observables equilibrate. A deviation in the thermalization of interaction energy was observed in the absence of long-range interactions as well as for large system sizes, exposing a close connection between thermalization and system integrability. For the system size of $N = 11$, for which eigenvector analysis was possible, the Z_2 order parameter emerged as a robust indicator of equilibrium behavior across all parameter regimes. On the whole, these results demonstrate mechanisms by which thermalization can arise in closed many-body Rydberg systems, providing fundamental insight into how energy from a realistic source of phase noise distributes and equilibrates.

Chapter 6

Conclusions

This thesis explored the complex behavior of realistic phase noise in the context of a closed many-body system, specifically a Rydberg spin chain. Through a combination of stochastic noise modeling, exact diagonalization, and tensor network simulations we develop a comprehensive numerical framework capable of simulating and analyzing the effects of experimentally relevant phase noise on quantum many-body dynamics. These tools were implemented in the simulation of an adiabatic state preparation of the Z_2 ordered spin chain in a transverse field Ising model (TFIM) with noise induced dephasing errors in the transverse field. The findings attained from these simulations provide a detailed look into the effects of realistic dephasing on the adiabatic process, showing not only resulting degradation in the performance of the preparation for a variety of system sizes and noise profiles, but also the mechanisms that allow for the thermalization of standard many-body observables. In this final chapter, we provide a broad summary of the topics and results discussed, as well as an outlook for future directions opened by this work.

6.1 Summary

In Chapter 2 we laid the foundation for modeling noise by introducing the mathematics of stochastic processes and their use in simulating realistic laser phase fluctuations. By leveraging well known stochastic processes such as the Wiener and Ornstein-Uhlenbeck processes and implementing the Timmer-Koenig algorithm, we developed an efficient method for generating long, correlated phase noise sequences whose spectral characteristics can be tailored to match experimental power spectral densities (PSDs). The TK95 algorithm is in essence a Gaussian sampling model that generates unique instances of a given noise profile in Fourier space, and is chosen for its versatility and ease of implementation in comparison to other generative noise models. This approach allowed for the generation and implementation of realistic dephasing effects into simulations of quantum dynamics as a phase modulating term on the transverse field of a TFIM.

In Chapter 3, we introduced the tensor network formalism, particularly matrix product states (MPS), which enabled the efficient numerical treatment of quantum systems too large for exact diagonalization. The use of MPS and matrix product operators (MPOs), along with canonical forms and the time-dependent variational principle (TDVP), equipped us with powerful tools to simulate time evolution of the TFIM with added phase noise. These methods were critical for extending simulations to larger system sizes, allowing us to move beyond the constraints of exact diagonalization while preserving accuracy. Moreover, finite temperature techniques such as imaginary time evolution and purification made it possible to construct thermal states for direct comparison with noise-driven dynamics, forming a crucial part of our thermalization analysis in Chapter 5.

With these tools in hand, Chapter 4 examined the principles of adiabatic state preparation in the TFIM, highlighting the role of slow, coherent parameter ramps in accessing non-trivial many-body ground states. The crystalline phases emerging from the interplay between detuning and blockade effects served as ideal test cases for understanding state preparation fidelity. This chapter established the baseline behavior of a clean adiabatic protocol, critical for distinguishing between diabatic errors intrinsic to the protocol and additional decoherence effects arising from the later addition of phase noise. The dynamics were shown to be highly sensitive to variation speed, particularly near critical points where energy gaps are small, underlining the need for carefully tuned ramp profiles in practical implementations. Following this, we introduced phase noise into the picture and analyzed its immediate effect on state preparation fidelity. We found that phase noise, despite being slow and classical in origin, can drive significant excitation over longer ramp times where decoherence accumulates. This highlighted a key trade-off: while slow ramps minimize diabatic error, they also expose the system to prolonged dephasing, resulting in lowered fidelity as a result of dephasing excitation. Also important was the phase noise profile, with spectral content of a given PSD resonant with many-body gaps driving particularly strong excitation. This chapter thus provided an in depth look at the direct effect of noise on state preparation, and set the stage for the following central inquiry of this thesis: does phase noise excitation lead to thermalization, and under what conditions?

This question was addressed in Chapter 5, where we moved beyond fidelity and toward characterizing the equilibrium behavior of noise-perturbed systems. To achieve this, we define long-time and thermal expectation values as averages over the diagonal ensemble which provides the true equilibrium state, and the canonical ensemble which is derived from the Boltzmann distribution for a given thermodynamic temperature, as weighted by the energy distribution of a given observable. Comparing these expectation values provides a direct measure of thermalization that can then be used to study a variety of parameter regimes. We observe how such thermalization depends on interaction range, system size, and the properties of a given observable as a function of energy. Our results demonstrated that realistic phase noise can, in fact, drive thermalization in many-body systems,but the underlying mechanisms are not trivial and consist of many non-uniform excitation patterns that on average behave according to thermal prediction. We report that the presence of long-range interactions breaks degeneracies and enables richer excitation pathways, allowing the noise to distribute energy more evenly and leading to thermal-like equilibrium in both of the studied observables. In contrast, more integrable systems with only nearest-neighbor interactions showed suppressed excitation and deviation from thermal predictions when thermalization over the interaction energy observable was evaluated, since phase noise leads disproportionately to excitation of highly disordered states with larger corresponding energy. This distinction underscores the role of Hamiltonian structure in determining how effectively noise can explore the Hilbert space and mimic thermal equilibration. Notably, thermalization remained robust when evaluated for the Z_2 order parameter even after long-range interactions were removed. This was caused by a combination of disproportionate excitation into specific high energy states with high transition rates, but with less overall excitation across the spectrum such that most occupancy was still in the fully Z_2 ordered ground state. This resilient thermalization of the Z_2 order parameter was also seen in increasing system sizes, which were calculated using tensor-network methods for time evolution and thermal state approximation. However, for the largest system size of 31 sites we see thermalization break down. We believe that although the excitation dynamics that lead to thermalization remain constant across system size, there is a window within which the system can appear to behave thermal with increasing system size: the mitigation of diabatic excitation requires longer evolution times, but over-excitation into energy sectors with high transition rates skews the expectation spectra away from the uniform distributions predicted by a thermal equilibrium, and thus requires shorter evolution times. Simulations in 31 sites appear to have closed this window and no longer thermalize.

6.2 Outlook

The work presented in this thesis provides a solid foundation for the study of realistic experimental noise in dynamical many-body quantum systems. The techniques developed here offer scalable and faithful approaches for incorporating laser phase noise into many-body simulations, and can be readily extended to a plethora of other experimentally relevant noise sources including amplitude and even thermal noise. Such noise generation techniques allow us to bridge the gap between idealized quantum simulations and the noisy conditions under which current and near-term experiments operate. What is more, tensor network methods that have in recent years drastically improved the capabilities of numerical simulation of quantum mechanics can only benefit from the integration of realistic noise.

Looking towards the physics discussed in this thesis, study of phase noise in adiabatic protocols has broad implications for quantum simulation and computation with Rydberg atom arrays, especially as system sizes increase and noise mitigation becomes a growing challenge. Future research in this topic could explore a broader range of phase noise spectra [119], higher-dimensional Rydberg geometries, as well as observing the effects of phase noise on different Rydberg accessible interacting Hamiltonians to test the generality of our results. Also of interest is a parallel investigation of phase noise in the Van der Waals Rydberg interaction regime in which interactions scale as $1/r^6$ as opposed to the $1/r^3$ scaling of dipole-dipole interactions, and has become common in experimental setups in recent years [49, 51, 219, 220]. The study of thermalization in particular can also be made more rigorous by introducing more observables and testing a variety of adiabatic protocols, as well as Rydberg accessible Hamiltonians to get further insight into phase noise excitation dynamics and the effects of changing integrability. Of particular interest would be protocols that are not restrained to ground states, such that thermalization can be tested higher in the energy spectrum where the larger density of states makes the use of the microcanonical ensemble possible. Furthermore, order parameters may stand out as a reliable metric for assessing equilibrium behavior across system sizes and interaction models, and could play a role as valuable diagnostic tools in both theoretical and experimental contexts.

In conclusion, this thesis has illuminated the rich and subtle dynamics that emerge when controlled quantum evolution is perturbed by realistic noise. By combining advanced numerical methods with physical modeling grounded in experimental systems, we have contributed a detailed and nuanced understanding of how decoherence impacts adiabatic preparation by introducing energy that under some conditions results in thermalization in many-body quantum systems. These results not only inform future experimental design but also deepen our theoretical understanding of quantum thermalization and noise resilience in complex quantum devices.

Appendix A

Derivation of the theoretical solution for the O-U process

To derive the analytical solution for the Ornstein-Uhlenbeck (O-U) process, we start with the stochastic differential equation (SDE)

$$dx(t) = k(\mu - x(t))dt + \sqrt{D}dW. \tag{A.1}$$

We introduce a time-dependent transformation (ansatz) to eliminate the state-dependent drift term

$$f(x,t) = xe^{kt}. \tag{A.2}$$

Taking the total differential df using the product rule (noting that the second-order Ito term $\frac{\partial^2 f}{\partial x^2}$ is zero)

$$df = \frac{\partial f}{\partial t}dt + \frac{\partial f}{\partial x}dx = kxe^{kt}dt + e^{kt}dx. \tag{A.3}$$

Substituting the expression for dx from the SDE into the differential df

$$df = kxe^{kt}dt + e^{kt}\left[k(\mu - x)dt + \sqrt{D}dW\right] \tag{A.4}$$

$$df = kxe^{kt}dt + k\mu e^{kt}dt - kxe^{kt}dt + \sqrt{D}e^{kt}dW. \tag{A.5}$$

The terms involving $x(t)$ cancel out, leaving

$$df = k\mu e^{kt}dt + \sqrt{D}e^{kt}dW. \tag{A.6}$$

Integrating both sides from 0 to t

$$\int_0^t df = \int_0^t k\mu e^{ks}ds + \int_0^t \sqrt{D}e^{ks}dW(s). \tag{A.7}$$

Evaluating the left side using $f(x,t) = x(t)e^{kt}$

$$x(t)e^{kt} - x(0) = \mu(e^{kt} - 1) + \sqrt{D}\int_0^t e^{ks}dW(s). \tag{A.8}$$

Multiplying through by e^{-kt} to isolate $x(t)$

$$x(t) = x(0)e^{-kt} + \mu(1 - e^{-kt}) + \sqrt{D}\int_0^t e^{-k(t-s)}dW(s). \tag{A.9}$$

This confirms the solution presented in Eq. (2.27).

Appendix B

The adiabatic theorem and adiabatic approximations

The adiabatic theorem is one of the foundational results in quantum mechanics, providing a controlled way to dynamically evolve a system from a given initial state, such as a ground state of a non-interacting Hamiltonian, to a more complex final state, while suppressing unwanted excitations to higher-energy states. In this appendix, we describe the adiabatic theorem and adiabatic approximations. The description of the adiabatic theorem is given, providing the tools necessary to traverse Hamiltonian parameter space and construct adiabatic ramps that allow for the adiabatic preparation of states.

The adiabatic theorem states that a quantum system initialized in an eigenstate of a slowly varying Hamiltonian will remain in its instantaneous eigenstate, provided the evolution is slow compared to the energy gap between the considered state and nearby states in the spectrum. If the Hamiltonian parameters are tuned sufficiently slowly, then the physical properties of the system will adjust dynamically so that the a system initialized in a given state remains in the same state but for the instantaneous Hamiltonian. This theorem only holds in the limit of infinite time, and generally, the smaller the energy gap to the nearest state ΔE the slower the change of the parameters needs to be to minimize the loss of adiabaticity. In practice, where evolution times are finite, this effect is only approximated. The theorem can be derived explicitly by expanding the initial time dependent state into a superposition of eigenstates of the Hamiltonian at a given time t,

$$|\psi_0(t)\rangle = \sum_n c_n(t)|\alpha_n(t)\rangle. \tag{B.1}$$

This expansion can then be placed into the Schrodinger equation

$$\hat{H}(t)|\psi_0(t)\rangle = i\hbar\frac{\partial}{\partial t}|\psi_0(t)\rangle, \tag{B.2}$$

$$\sum_n c_n(t)\Big[H(t)|\alpha_n(t)\rangle\Big] = \sum_n \Big[i\hbar\frac{\partial}{\partial t}c_n(t)|\alpha_n(t)\rangle + i\hbar c_n(t)\frac{\partial}{\partial t}|\alpha_n(t)\rangle\Big]. \tag{B.3}$$

Now we can take the inner product of this equation with the eigenstate $|\alpha_m\rangle$ to get

$$\sum_n c_n(t)E_n(t)\langle\alpha_m(t)|\alpha_n(t)\rangle = i\hbar\sum_n \Big[\dot{c}_n(t)\langle\alpha_m(t)|\alpha_n(t)\rangle + c_n(t)\langle\alpha_m(t)|\dot{\alpha}_n(t)\rangle\Big], \tag{B.4}$$

$$c_m(t)E_m(t) = i\hbar\Big[\dot{c}_m(t) + \sum_n c_n(t)\langle\alpha_m(t)|\dot{\alpha}_n(t)\rangle\Big]. \tag{B.5}$$

This equation gives us a sense of how the average energy expectation values change with time, but leads to an inner product with a $\langle\alpha_m(t)|\dot{\alpha_n}(t)\rangle$ term which is not straightforward to evaluate. To move forward with this we instead evaluate the time derivative of eigenvalue equation for the LHS of Eq. B.2 to get

$$\frac{\partial}{\partial t}\Big(\hat{H}_{(t)}|\alpha_n(t)\rangle\Big) = \frac{\partial}{\partial t}\Big(E_n(t)|\alpha_n(t)\rangle\Big), \tag{B.6}$$

$$\dot{\hat{H}}(t)|\alpha_n(t)\rangle + \hat{H}(t)|\dot{\alpha_n}(t)\rangle = \dot{E}_n(t)|\alpha_n(t)\rangle + E_n(t)|\dot{\alpha_n}(t)\rangle. \tag{B.7}$$

Now, using the fact that $\langle\alpha_m(t)|\hat{H}(t) = E_m(t)\langle\alpha_m|$ we once again take the inner product with an eigenstate $|\alpha_m\rangle$ leading to

$$\langle\alpha_m(t)|\dot{\hat{H}}(t)|\alpha_n(t)\rangle + E_m(t)\langle\alpha_m(t)|\dot{\alpha_n}(t)\rangle = \langle\alpha_m(t)|\dot{E}_n(t)|\alpha_n(t)\rangle + E_n(t)\langle\alpha_m(t)|\dot{\alpha_n}(t)\rangle. \tag{B.8}$$

Here we can employ orthonormality $\langle\alpha_m(t)|\alpha_n(t)\rangle = 0$ for $n \neq m$, as well as the fact that E and $\dot{E}$ are just numbers to eliminate the first term on the RHS. The case of $n \neq m$ is of particular interest as we want to get an understanding of the state mixing that occurs when the initial state $|\alpha_n\rangle$ is excited to nearby energy eigenstates $|\alpha_m\rangle$. We see the inner product $\langle\alpha_m(t)|\dot{\alpha_n}(t)\rangle$ also appear here, and we can rearrange for this term as follows

$$-\frac{\langle \alpha_m(t)|\dot{\hat{H}}(t)|\alpha_n(t)\rangle}{E_m - E_n} = \langle \alpha_m(t)|\dot{\alpha_n}(t)\rangle \qquad for \quad m \neq n. \tag{B.9}$$

We can now insert this new expression back into Eq. B.5 to get an expression for the dynamics of the coefficients $c_m(t)$ in the form

$$i\hbar\dot{c}_m(t) = E_m(t)c_m(t) - i\hbar\sum_{n\neq m}\frac{\langle \alpha_m(t)|\dot{\hat{H}}(t)|\alpha_n(t)\rangle}{E_m - E_n}c_n(t). \tag{B.10}$$

Since the choice of n and m is arbitrary here, we can instead choose m to represent our initial state. Thus, we can see that for the change in the ground state coefficient $\dot{c}_m(t)$ to remain dependent only on the instantaneous values of $c_m(t)$ and a ground state energy $E_m(t)$ (thus avoiding state mixing), the second term on the RHS must be minimized. The adiabatic theorem follows

$$\therefore |\langle \alpha_m(t)|\dot{\hat{H}}(t)|\alpha_n(t)\rangle| \ll \frac{1}{\hbar}|E_m(t) - E_n(t)|^2. \tag{B.11}$$

In other words, to minimize the probability of mixing our ground state with any given higher energy state the change in the Hamiltonian due to the tuning of laser parameters Ω and δ must always remain much smaller than the energy gap ΔE between the two states.

Landau–Zener Approximation

The adiabatic theorem above gives a qualitative condition for remaining in the instantaneous eigenstate, but does not directly quantify the probability of excitation when the system passes near an avoided crossing, where ΔE is small. A more precise estimate is provided by the Landau–Zener (LZ) model, which describes a two-level system with a linearly changing energy bias:

$$H_{\mathrm{LZ}}(t) = \begin{pmatrix} vt/2 & \Delta \\ \Delta & -vt/2 \end{pmatrix}, \tag{B.12}$$

where v is the rate of change of the diabatic energy levels, and 2Δ is the minimum energy gap at the avoided crossing. The Landau–Zener formula gives the probability of a non-adiabatic transition as:

$$P_{\mathrm{LZ}} = \exp\left(- \frac{2\pi\Delta^2}{\hbar v} \right). \tag{B.13}$$

In the limit $P_{\mathrm{LZ}} \to 0$, the evolution is adiabatic, while for larger P_{LZ}, excitations are created. In experimental settings such as adiabatic quantum computing or the Rydberg atom state preparation discussed in this thesis, this expression is widely used to choose optimal ramp rates for detuning and Rabi frequency, balancing adiabaticity against finite experimental times.

Appendix C

Rotating frame transformations in a Rydberg Hamiltonian with laser phase noise

The standard representation of laser phase noise in a Rydberg Hamiltonian involves a stochastic phase term coupled to the transverse drive. It is often desirable to transform the system into a frame where the Hamiltonian remains purely real. We begin with the Hamiltonian for a Rydberg atom array in the fixed-frequency rotating frame

$$\hat{H}_R(t) = \frac{\Omega(t)}{2} \sum_{k}^{N} \left[e^{-i\phi(t)} \hat{\sigma}_k^+ + e^{i\phi(t)} \hat{\sigma}_k^- \right] - \delta(t) \sum_{k}^{N} \hat{n}_k + \sum_{k<l} V_{kl} \hat{n}_k \hat{n}_l, \tag{C.1}$$

where $\hat{\sigma}_k^+ = |1\rangle_k \langle 0|_k$ and $\hat{\sigma}_k^- = |0\rangle_k \langle 1|_k$ are the raising and lowering operators, $\hat{n}_k$ is the number operator counting Rydberg occupation, and $\phi(t)$ is a stochastic variable representing phase fluctuations. To eliminate the phase factor from the Rabi term, we define a time-dependent unitary transformation

$$\hat{U}(t) = \exp\left(-i\phi(t) \sum_{k}^{N} \hat{n}_k \right), \tag{C.2}$$

which effectively rotates the basis states to a frame that is in line with the phase jitter of the laser. Under a time-dependent unitary transformation, the effective

Hamiltonian in the new frame, $\hat{H}'$, is given by the relation

$$\hat{H}' = \hat{U}\hat{H}_R\hat{U}^\dagger + i\left(\frac{\partial \hat{U}}{\partial t}\right)\hat{U}^\dagger. \tag{C.3}$$

Applying the first term in this transformation, we observe that the detuning $\delta(t)$ and the interaction term V_{kl} commute with $\hat{U}$ because they are built using only $\hat{n}_k$. Consequently, these terms remain invariant in the new frame. However, the transverse coupling term is modified by the transformation of the raising and lowering operators, where $\hat{U}\hat{\sigma}_k^+\hat{U}^\dagger = \hat{\sigma}_k^+ e^{i\phi(t)}$ and $\hat{U}\hat{\sigma}_k^-\hat{U}^\dagger = \hat{\sigma}_k^- e^{-i\phi(t)}$. Substituting these into the Rabi term of Eq. (C.1) yields

$$\frac{\Omega(t)}{2}\sum_k \left(e^{-i\phi(t)}e^{i\phi(t)}\hat{\sigma}_k^+ + e^{i\phi(t)}e^{-i\phi(t)}\hat{\sigma}_k^-\right) = \frac{\Omega(t)}{2}\sum_k^N \hat{\sigma}_x^k. \tag{C.4}$$

This step effectively “unwinds” the phase noise from the transverse drive. The second part of the transformation law in Eq. (C.3) accounts for the “inertial” or “gauge” term arising from the explicit time-dependence of the unitary operator. Differentiating $\hat{U}$ with respect to time gives

$$\frac{\partial \hat{U}}{\partial t} = -i\dot{\phi}(t)\left(\sum_k^N \hat{n}_k\right)\exp\left(-i\phi(t)\sum_k^N \hat{n}_k\right). \tag{C.5}$$

Multiplying by i and $\hat{U}^\dagger$ results in the addition of a longitudinal term $\dot{\phi}(t)\sum \hat{n}_k$ to the Hamiltonian. Physically, $\dot{\phi}(t)$ represents the instantaneous frequency fluctuation of the laser, and can thus be understood as a stochastic jitter in phase. Combining all components, the final transformed Hamiltonian is expressed as

$$\hat{H}' = \frac{\Omega(t)}{2}\sum_k^N \hat{\sigma}_x^k - \left[\delta(t) - \dot{\phi}(t)\right]\sum_k^N \hat{n}_k + \sum_{k<l} V_{kl}\hat{n}_k\hat{n}_l. \tag{C.6}$$

This result provides a rigorous mathematical justification for treating laser phase noise as a stochastic fluctuation of the detuning. In the context of numerical modeling using the TK95 algorithm, this transformation allows the use of purely real-valued matrices.

Bibliography

[1] Niels Bohr. I. on the constitution of atoms and molecules. *The London, Edinburgh, and Dublin Philosophical Magazine and Journal of Science*, 26 (151):1–25, 1913. doi: 10.1080/14786441308634955. URL `https://doi.org/10.1080/14786441308634955`.

[2] J. S. Bell. On the Einstein, Podolsky Rosen paradox. *Physics Physique Fizika*, 1:195–200, 1964. doi: 10.1103/PhysicsPhysiqueFizika.1.195. URL `https://link.aps.org/doi/10.1103/PhysicsPhysiqueFizika.1.195`.

[3] Stuart J. Freedman and John F. Clauser. Experimental test of local hidden-variable theories. *Phys. Rev. Lett.*, 28:938–941, 1972. doi: 10.1103/PhysRevLett.28.938. URL `https://link.aps.org/doi/10.1103/PhysRevLett.28.938`.

[4] Simon M. Sze and Kwok K. Ng. *Physics of Semiconductor Devices*. John Wiley & Sons, Ltd, Hoboken, NJ, 3rd edition, 2006. ISBN 978-0-470-06832-8. doi: 10.1002/9780470068328. URL `https://onlinelibrary.wiley.com/doi/book/10.1002/9780470068328`.

[5] Antonio Acín, Immanuel Bloch, Harry Buhrman, Tommaso Calarco, Christopher Eichler, Jens Eisert, Daniel Esteve, Nicolas Gisin, Steffen J Glaser, Fedor Jelezko, Stefan Kuhr, Maciej Lewenstein, Max F Riedel, Piet O Schmidt, Rob Thew, Andreas Wallraff, Ian Walmsley, and Frank K Wilhelm. The quantum technologies roadmap: a European community view. *New Journal of Physics*, 20(8):080201, 2018. doi: 10.1088/1367-2630/aad1ea. URL `https://dx.doi.org/10.1088/1367-2630/aad1ea`.

[6] A. Fedorov, N. Gisin, Serguei Beloussov, and A. Lvovsky. Quantum computing at the quantum advantage threshold: a down-to-business review. *arXiv preprint arXiv:2203.17181*, 2022. doi: 10.48550/arXiv.2203.17181. URL `https://api.semanticscholar.org/CorpusID:247839279`.

[7] Dongxin Gao, Daojin Fan, Chen Zha, Jiahao Bei, Guoqing Cai, Jianbin Cai, Sirui Cao, Fusheng Chen, Jiang Chen, Kefu Chen, Xiawei Chen, Xiqing Chen, Zhe Chen, Zhiyuan Chen, Zihua Chen, Wenhao Chu, Hui Deng, Zhibin Deng, Pei Ding, Xun Ding, Zhuzhengqi Ding, Shuai Dong, Yupeng Dong, Bo Fan, Yuanhao Fu, Song Gao, Lei Ge, Ming Gong, Jiacheng Gui, Cheng Guo, Shaojun Guo, Xiaoyang Guo, Lianchen Han, Tan He, Linyin Hong, Yisen Hu, He-Liang Huang, Yong-Heng Huo, Tao Jiang, Zuokai Jiang, Honghong Jin, Yunxiang Leng, Dayu Li, Dongdong Li, Fangyu Li, Jiaqi Li, Jinjin Li, Junyan Li, Junyun Li, Na Li, Shaowei Li, Wei Li, Yuhuai Li, Yuan Li, Futian Liang, Xuelian Liang, Nanxing Liao, Jin Lin, Weiping Lin, Dailin Liu, Hongxiu Liu, Maliang Liu, Xinyu Liu, Xuemeng Liu, Yancheng Liu, Haoxin Lou, Yuwei Ma, Lingxin Meng, Hao Mou, Kailiang Nan, Binghan Nie, Meijuan Nie, Jie Ning, Le Niu, Wenyi Peng, Haoran Qian, Hao Rong, Tao Rong, Huiyan Shen, Qiong Shen, Hong Su, Feifan Su, Chenyin Sun, Liangchao Sun, Tianzuo Sun, Yingxiu Sun, Yimeng Tan, Jun Tan, Longyue Tang, Wenbing Tu, Cai Wan, Jiafei Wang, Biao Wang, Chang Wang, Chen Wang, Chu Wang, Jian Wang, Liangyuan Wang, Rui Wang, Shengtao Wang, Xiaomin Wang, Xinzhe Wang, Xunxun Wang, Yeru Wang, Zuolin Wei, Jiazhou Wei, Dachao Wu, Gang Wu, Jin Wu, Shengjie Wu, Yulin Wu, Shiyong Xie, Lianjie Xin, Yu Xu, Chun Xue, Kai Yan, Weifeng Yang, Xinpeng Yang, Yang Yang, Yangsen Ye, Zhenping Ye, Chong Ying, Jiale Yu, Qinjing Yu, Wenhu Yu, Xiangdong Zeng, Shaoyu Zhan, Feifei Zhang, Haibin Zhang, Kaili Zhang, Pan Zhang, Wen Zhang, Yiming Zhang, Yongzhuo Zhang, Lixiang Zhang, Guming Zhao, Peng Zhao, Xianhe Zhao, Xintao Zhao, Youwei Zhao, Zhong Zhao, Luyuan Zheng, Fei Zhou, Liang Zhou, Na Zhou, Naibin Zhou, Shifeng Zhou, Shuang Zhou, Zhengxiao Zhou, Chengjun Zhu, Qingling Zhu, Guihong Zou, Haonan Zou, Qiang Zhang, Chao-Yang Lu, Cheng-Zhi Peng, Xiaobo Zhu, and Jian-Wei Pan. Establishing a new benchmark in quantum computational advantage with 105-qubit ZUCHONGZHI 3.0 processor. *Phys. Rev. Lett.*, 134:090601, 2025. doi: 10.1103/PhysRevLett.134.090601. URL `https://link.aps.org/doi/10.1103/PhysRevLett.134.090601`.

[8] He-Liang Huang, Dachao Wu, Daojin Fan, and Xiaobo Zhu. Superconducting quantum computing: A review. *Science China Information Sciences*, 63, 2020. doi: 10.1007/s11432-020-2881-9.

[9] Manuel Morgado and Shannon Whitlock. Quantum simulation and computing with Rydberg-interacting qubits. *AVS Quantum Science*, 3:023501, 2021. doi: 10.1116/5.0036562. URL `https://api.semanticscholar.org/CorpusID:226254232`.

[10] Sergei Slussarenko and Geoff J. Pryde. Photonic/ quantum information processing: A concise review. *Applied Physics Reviews*, 6(4):041303, 2019. ISSN 1931-9401. doi: 10.1063/1.5115814. URL `https://doi.org/10.1063/1.5115814`.

[11] Marcus W. Doherty, Neil B. Manson, Paul Delaney, Fedor Jelezko, Jörg Wrachtrup, and Lloyd C.L. Hollenberg. The nitrogen-vacancy colour centre in diamond. *Physics Reports*, 528(1):1–45, 2013. ISSN 0370-1573. doi: https://doi.org/10.1016/j.physrep.2013.02.001.

[12] Colin D. Bruzewicz, John Chiaverini, Robert McConnell, and Jeremy M. Sage. Trapped-ion quantum computing: Progress and challenges. *Applied Physics Reviews*, 6(2):021314, 2019. ISSN 1931-9401. doi: 10.1063/1.5088164.

[13] J. Ignacio Cirac and Peter Zoller. Goals and opportunities in quantum simulation. *Nature Physics*, 8(4):264–266, 2012. ISSN 1745-2481. doi: 10.1038/nphys2275. URL `https://doi.org/10.1038/nphys2275`.

[14] Neill Lambert, Eric Giguère, Paul Menczel, Boxi Li, Patrick Hopf, Gerardo Suárez, Marc Gali, Jake Lishman, Rushiraj Gadhvi, Rochisha Agarwal, Asier Galicia, Nathan Shammah, Paul Nation, J. R. Johansson, Shahnawaz Ahmed, Simon Cross, Alexander Pitchford, and Franco Nori. QuTiP 5: The Quantum Toolbox in Python. *quant-ph*, 2024. URL `https://arxiv.org/abs/2412.04705`.

[15] Sebastian Weber, Sylvain de Léséleuc, Vincent Lienhard, Daniel Barredo, Thierry Lahaye, Antoine Browaeys, and Hans Peter Büchler. Topologically protected edge states in small Rydberg systems. *Quantum Science and Technology*, 3(4):044001, 2018. ISSN 2058-9565. doi: 10.1088/2058-9565/aaca47. URL `http://dx.doi.org/10.1088/2058-9565/aaca47`.

[16] A.F. Albuquerque, F. Alet, P. Corboz, P. Dayal, A. Feiguin, S. Fuchs, L. Gamper, E. Gull, S. Gürtler, A. Honecker, R. Igarashi, M. Körner,

A. Kozhevnikov, A. Läuchli, S.R. Manmana, M. Matsumoto, I.P. McCulloch, F. Michel, R.M. Noack, G. Pawłowski, L. Pollet, T. Pruschke, U. Schollwöck, S. Todo, S. Trebst, M. Troyer, P. Werner, and S. Wessel. The ALPS project release 1.3: Open-source software for strongly correlated systems. *Journal of Magnetism and Magnetic Materials*, 310(2, Part 2): 1187–1193, 2007. ISSN 0304-8853. doi: https://doi.org/10.1016/j.jmmm.2006.10.304. URL `https://www.sciencedirect.com/science/article/pii/S0304885306014983`. Proceedings of the 17th International Conference on Magnetism.

[17] Matthew Fishman, Steven R. White, and E. Miles Stoudenmire. The ITensor Software Library for Tensor Network Calculations. *SciPost Phys. Codebases*, page 4, 2022. doi: 10.21468/SciPostPhysCodeb.4. URL `https://scipost.org/10.21468/SciPostPhysCodeb.4`.

[18] Tyson Jones, Anna Brown, Ian Bush, and Simon C. Benjamin. QuEST and high performance simulation of quantum computers. *Scientific Reports*, 9 (1):10736, 2019. doi: 10.1038/s41598-019-47174-9. URL `https://doi.org/10.1038/s41598-019-47174-9`.

[19] Ali Javadi-Abhari, Matthew Treinish, Kevin Krsulich, Christopher J. Wood, Jake Lishman, Julien Gacon, Simon Martiel, Paul D. Nation, Lev S. Bishop, Andrew W. Cross, Blake R. Johnson, and Jay M. Gambetta. Quantum computing with Qiskit, 2024.

[20] David Petrosyan, Klaus Mølmer, and Michael Fleischhauer. On the adiabatic preparation of spatially-ordered Rydberg excitations of atoms in a one-dimensional optical lattice by laser frequency sweeps. *Journal of Physics B: Atomic, Molecular and Optical Physics*, 49(8), 2016. ISSN 1361-6455. doi: 10.1088/0953-4075/49/8/084003. URL `http://dx.doi.org/10.1088/0953-4075/49/8/084003`.

[21] Marcin Kalinowski, Rhine Samajdar, Roger G. Melko, Mikhail D. Lukin, Subir Sachdev, and Soonwon Choi. Bulk and boundary quantum phase transitions in a square Rydberg atom array. *Phys. Rev. B*, 105:174417, 2022. doi: 10.1103/PhysRevB.105.174417. URL `https://link.aps.org/doi/10.1103/PhysRevB.105.174417`.

[22] G. Pelegrí, A. J. Daley, and J. D. Pritchard. High-fidelity multiqubit Rydberg gates via two-photon adiabatic rapid passage. *Quantum Science*

and Technology, 7(4):045020, 2022. doi: 10.1088/2058-9565/ac823a. URL `https://dx.doi.org/10.1088/2058-9565/ac823a`.

[23] Hyungwon Kim, Tatsuhiko N. Ikeda, and David A. Huse. Testing whether all eigenstates obey the eigenstate thermalization hypothesis. *Phys. Rev. E*, 90:052105, 2014. doi: 10.1103/PhysRevE.90.052105. URL `https://link.aps.org/doi/10.1103/PhysRevE.90.052105`.

[24] A. Dauphin, M. Müller, and M. A. Martin-Delgado. Quantum simulation of a topological Mott insulator with Rydberg atoms in a Lieb lattice. *Phys. Rev. A*, 93:043611, 2016. doi: 10.1103/PhysRevA.93.043611. URL `https://link.aps.org/doi/10.1103/PhysRevA.93.043611`.

[25] Simone Notarnicola, Mario Collura, and Simone Montangero. Real-time-dynamics quantum simulation of (1 + 1)-dimensional lattice qed with Rydberg atoms. *Phys. Rev. Res.*, 2:013288, 2020. doi: 10.1103/PhysRevResearch.2.013288. URL `https://link.aps.org/doi/10.1103/PhysRevResearch.2.013288`.

[26] M. D. Lukin, M. Fleischhauer, R. Cote, L. M. Duan, D. Jaksch, J. I. Cirac, and P. Zoller. Dipole blockade and quantum information processing in mesoscopic atomic ensembles. *Phys. Rev. Lett.*, 87:037901, 2001. doi: 10.1103/PhysRevLett.87.037901. URL `https://link.aps.org/doi/10.1103/PhysRevLett.87.037901`.

[27] Immanuel Bloch. Quantum coherence and entanglement with ultracold atoms in optical lattices. *Nature*, 453(7198):1016–1022, 2008. ISSN 1476-4687. doi: 10.1038/nature07126. URL `https://doi.org/10.1038/nature07126`.

[28] M. Saffman, T. G. Walker, and K. Mølmer. Quantum information with Rydberg atoms. *Rev. Mod. Phys.*, 82:2313–2363, 2010. doi: 10.1103/RevModPhys.82.2313. URL `https://link.aps.org/doi/10.1103/RevModPhys.82.2313`.

[29] Daniel Barredo, Sylvain de Léséleuc, Vincent Lienhard, Thierry Lahaye, and Antoine Browaeys. An atom-by-atom assembler of defect-free arbitrary two-dimensional atomic arrays. *Science*, 354(6315):1021–1023, 2016. doi: 10.1126/science.aah3778. URL `https://www.science.org/doi/abs/10.1126/science.aah3778`.

[30] F. Nogrette, H. Labuhn, S. Ravets, D. Barredo, L. Béguin, A. Vernier, T. Lahaye, and A. Browaeys. Single-atom trapping in holographic 2D arrays of microtraps with arbitrary geometries. *Phys. Rev. X*, 4:021034, 2014. doi: 10.1103/PhysRevX.4.021034. URL `https://link.aps.org/doi/10.1103/PhysRevX.4.021034`.

[31] P. Huft, Y. Song, T. M. Graham, K. Jooya, S. Deshpande, C. Fang, M. Kats, and M. Saffman. Simple, passive design for large optical trap arrays for single atoms. *Phys. Rev. A*, 105:063111, 2022. doi: 10.1103/PhysRevA.105.063111. URL `https://link.aps.org/doi/10.1103/PhysRevA.105.063111`.

[32] Guy Bensky, Robert Amsüss, Johannes Majer, David Petrosyan, Jörg Schmiedmayer, and Gershon Kurizki. Controlling quantum information processing in hybrid systems on chips. *Quantum Information Processing*, 10(6): 1037, 2011. doi: 10.1007/s11128-011-0302-6. URL `https://doi.org/10.1007/s11128-011-0302-6`.

[33] Irfan Siddiqi. Engineering high-coherence superconducting qubits. *Nature Reviews Materials*, 6(10):875–891, 2021. doi: 10.1038/s41578-021-00370-4. URL `https://doi.org/10.1038/s41578-021-00370-4`.

[34] J. I. Cirac and P. Zoller. Quantum computations with cold trapped ions. *Phys. Rev. Lett.*, 74:4091–4094, 1995. doi: 10.1103/PhysRevLett.74.4091. URL `https://link.aps.org/doi/10.1103/PhysRevLett.74.4091`.

[35] K. A. Landsman, Y. Wu, P. H. Leung, D. Zhu, N. M. Linke, K. R. Brown, L. Duan, and C. Monroe. Two-qubit entangling gates within arbitrarily long chains of trapped ions. *Phys. Rev. A*, 100:022332, 2019. doi: 10.1103/PhysRevA.100.022332. URL `https://link.aps.org/doi/10.1103/PhysRevA.100.022332`.

[36] S. Ebadi, A. Keesling, M. Cain, T. T. Wang, H. Levine, D. Bluvstein, G. Semeghini, A. Omran, J.-G. Liu, R. Samajdar, X.-Z. Luo, B. Nash, X. Gao, B. Barak, E. Farhi, S. Sachdev, N. Gemelke, L. Zhou, S. Choi, H. Pichler, S.-T. Wang, M. Greiner, V. Vuletić, and M. D. Lukin. Quantum optimization of maximum independent set using Rydberg atom arrays. *Science*, 376(6598):1209–1215, 2022. doi: 10.1126/science.abo6587. URL `https://www.science.org/doi/abs/10.1126/science.abo6587`.

[37] Ivaylo S. Madjarov, Jacob P. Covey, Adam L. Shaw, Joonhee Choi, Anant Kale, Alexandre Cooper, Hannes Pichler, Vladimir Schkolnik, Jason R. Williams, and Manuel Endres. High-fidelity entanglement and detection of alkaline-earth Rydberg atoms. *Nature Phys.*, 16(8):857, 2020. ISSN 17452481. doi: 10.1038/s41567-020-0903-z. URL `http://dx.doi.org/10.1038/s41567-020-0903-z`.

[38] Sylvain de Léséleuc, Daniel Barredo, Vincent Lienhard, Antoine Browaeys, and Thierry Lahaye. Analysis of imperfections in the coherent optical excitation of single atoms to Rydberg states. *Phys. Rev. A*, 97:053803, 2018. doi: 10.1103/PhysRevA.97.053803. URL `https://link.aps.org/doi/10.1103/PhysRevA.97.053803`.

[39] Dolev Bluvstein, Simon J. Evered, Alexandra A. Geim, Sophie H. Li, Hengyun Zhou, Tom Manovitz, Sepehr Ebadi, Madelyn Cain, Marcin Kalinowski, Dominik Hangleiter, J. Pablo Bonilla Ataides, Nishad Maskara, Iris Cong, Xun Gao, Pedro Sales Rodriguez, Thomas Karolyshyn, Giulia Semeghini, Michael J. Gullans, Markus Greiner, Vladan Vuletić, and Mikhail D. Lukin. Logical quantum processor based on reconfigurable atom arrays. *Nature*, 626(7997):58–65, 2023. ISSN 1476-4687. doi: 10.1038/s41586-023-06927-3. URL `http://dx.doi.org/10.1038/s41586-023-06927-3`.

[40] Deep Lall, Abhishek Agarwal, Weixi Zhang, Lachlan Lindoy, Tobias Lindström, Stephanie Webster, Simon Hall, Nicholas Chancellor, Petros Wallden, Raul Garcia-Patron, Elham Kashefi, Viv Kendon, Jonathan Pritchard, Alessandro Rossi, Animesh Datta, Theodoros Kapourniotis, Konstantinos Georgopoulos, and Ivan Rungger. A review and collection of metrics and benchmarks for quantum computers: definitions, methodologies and software, 2025. URL `https://arxiv.org/abs/2502.06717`.

[41] Hannes Bernien, Sylvain Schwartz, Alexander Keesling, Harry Levine, Ahmed Omran, Hannes Pichler, Soonwon Choi, Alexander S. Zibrov, Manuel Endres, Markus Greiner, Vladan Vuletić, and Mikhail D. Lukin. Probing many-body dynamics on a 51-atom quantum simulator. *Nature*, 551 (7682):579–584, 2017. ISSN 1476-4687. doi: 10.1038/nature24622. URL `http://dx.doi.org/10.1038/nature24622`.

[42] T. Pohl, E. Demler, and M. D. Lukin. Dynamical crystallization in the dipole blockade of ultracold atoms. *Phys. Rev. Lett.*, 104:043002, 2010. doi: 10.1103/PhysRevLett.104.043002. URL `https://link.aps.org/doi/10.1103/PhysRevLett.104.043002`.

[43] Michel Fabrice Serret, Bertrand Marchand, and Thomas Ayral. Solving optimization problems with Rydberg analog quantum computers: Realistic requirements for quantum advantage using noisy simulation and classical benchmarks. *Physical Review A*, 102(5), 2020. ISSN 2469-9934. doi: 10.1103/physreva.102.052617. URL `http://dx.doi.org/10.1103/PhysRevA.102.052617`.

[44] Minh-Thi Nguyen, Jin-Guo Liu, Jonathan Wurtz, Mikhail D. Lukin, Sheng-Tao Wang, and Hannes Pichler. Quantum optimization with arbitrary connectivity using Rydberg atom arrays. *PRX Quantum*, 4(1), 2023. ISSN 2691-3399. doi: 10.1103/prxquantum.4.010316. URL `http://dx.doi.org/10.1103/PRXQuantum.4.010316`.

[45] Hannah J. Manetsch, Gyohei Nomura, Elie Bataille, Kon H. Leung, Xudong Lv, and Manuel Endres. A tweezer array with 6100 highly coherent atomic qubits. *Arxiv*, 2024. URL `https://api.semanticscholar.org/CorpusID:268531555`.

[46] Thomas F. Gallagher. Rydberg atoms (cambridge monographs on atomic, molecular and chemical physics). In *Rydberg atoms*. Cambridge University Press, 2005.

[47] Jonathon A. Sedlacek, Arne Schwettmann, Harald Kübler, Robert Löw, Tilman Pfau, and James P. Shaffer. Microwave electrometry with Rydberg atoms in a vapour cell using bright atomic resonances. *Nature Physics*, 8(11):819–824, 2012. doi: 10.1038/nphys2423.

[48] T. A. Johnson, E. Urban, T. Henage, L. Isenhower, D. D. Yavuz, T. G. Walker, and M. Saffman. Rabi oscillations between ground and Rydberg states with dipole-dipole atomic interactions. *Phys. Rev. Lett.*, 100:113003, 2008. doi: 10.1103/PhysRevLett.100.113003. URL `https://link.aps.org/doi/10.1103/PhysRevLett.100.113003`.

[49] Henning Labuhn, Daniel Barredo, Sylvain Ravets, Sylvain de Léséleuc, Tommaso Macrì, Thierry Lahaye, and Antoine Browaeys. Tunable two-dimensional arrays of single Rydberg atoms for realizing quantum Ising models. *Nature*, 534(7609), 2016. ISSN 1476-4687. doi: 10.1038/nature18274. URL `http://dx.doi.org/10.1038/nature18274`.

[50] J de Hond, Nataly Cisternas, R J C Spreeuw, H B van Linden van den Heuvell, and N J van Druten. Interplay between Van der Waals and dipole-dipole interactions. we perform experiments that exhibit black-body-induced dipole-dipole interaction. we also point out some prospects for quantum simulation. *IOP*, 53(8):084007, 2020. doi: 10.1088/1361-6455/ab752b. URL `https://dx.doi.org/10.1088/1361-6455/ab752b`.

[51] Zeki Zeybek, Rick Mukherjee, and Peter Schmelcher. Quantum phases from competing Van der Waals and Dipole-Dipole interactions of Rydberg atoms. *Phys. Rev. Lett.*, 131:203003, 2023. doi: 10.1103/PhysRevLett.131.203003. URL `https://link.aps.org/doi/10.1103/PhysRevLett.131.203003`.

[52] Emily Altiere, Donald P. Fahey, Michael W. Noel, Rachel J. Smith, and Thomas J. Carroll. Dipole-dipole interaction between rubidium rydberg atoms. *Phys. Rev. A*, 84:053431, Nov 2011. doi: 10.1103/PhysRevA.84.053431. URL `https://link.aps.org/doi/10.1103/PhysRevA.84.053431`.

[53] Sylvain Ravets, Henning Labuhn, Daniel Barredo, Lucas Béguin, Thierry Lahaye, and Antoine Browaeys. Coherent dipole–dipole coupling between two single Rydberg atoms at an electrically-tuned förster resonance. *Nature Physics*, 10(12):914–917, 2014. doi: 10.1038/nphys3119. URL `https://doi.org/10.1038/nphys3119`.

[54] M. Reetz-Lamour, T. Amthor, J. Deiglmayr, and M. Weidemüller. Rabi oscillations and excitation trapping in the coherent excitation of a mesoscopic frozen Rydberg gas. *Physical Review Letters*, 100:253001, 2008. doi: 10.1103/PhysRevLett.100.253001.

[55] Daniel Barredo, Henning Labuhn, Sylvain Ravets, Thierry Lahaye, Antoine Browaeys, and Charles S. Adams. Coherent excitation transfer in a spin chain of three Rydberg atoms. *Phys. Rev. Lett.*, 114:113002, 2015. doi: 10.1103/PhysRevLett.114.113002. URL `https://link.aps.org/doi/10.1103/PhysRevLett.114.113002`.

[56] C S Adams, J D Pritchard, and J P Shaffer. Rydberg atom quantum technologies. *Journal of Physics B: Atomic, Molecular and Optical Physics*, 53(1):012002, 2019. doi: 10.1088/1361-6455/ab52ef. URL `https://dx.doi.org/10.1088/1361-6455/ab52ef`.

[57] D Jaksch, J I Cirac, P Zoller, S. L. Rolston, R. Côté, and M. D. Lukin. Fast quantum gates for neutral atoms. *Phys. Rev. Lett.*, 85(10):2208, 2000. ISSN 00319007. doi: 10.1103/PhysRevLett.85.2208.

[58] M. Saffman. Quantum computing with atomic qubits and Rydberg interactions: Progress and challenges. *J. Phys. B*, 49(20), 2016. ISSN 13616455. doi: 10.1088/0953-4075/49/20/202001.

[59] Peter Schauß, Johannes Zeiher, Takeshi Fukuhara, Stefan Hild, Marc Cheneau, Tommaso Macrì, Thomas Pohl, Immanuel Bloch, and Christian Gross. Crystallization in Ising quantum magnets. *Science*, 347(6229): 1455–1458, 2015. ISSN 0036-8075. doi: 10.1126/science.1258351. URL `https://doi.org/10.1126/science.1258351`.

[60] Antoine Browaeys and Thierry Lahaye. Many-body physics with individually controlled Rydberg atoms. *Nature Physics*, 16(2):132–142, 2020. ISSN 1745-2481. doi: 10.1038/s41567-019-0733-z. URL `https://doi.org/10.1038/s41567-019-0733-z`.

[61] Johannes Zeiher, Jae-yoon Choi, Antonio Rubio-Abadal, Thomas Pohl, Rick van Bijnen, Immanuel Bloch, and Christian Gross. Coherent many-body spin dynamics in a long-range interacting ising chain. *Phys. Rev. X*, 7:041063, Dec 2017. doi: 10.1103/PhysRevX.7.041063. URL `https://link.aps.org/doi/10.1103/PhysRevX.7.041063`.

[62] Dolev Bluvstein, Harry Levine, Giulia Semeghini, Tout T. Wang, Sepehr Ebadi, Marcin Kalinowski, Alexander Keesling, Nishad Maskara, Hannes Pichler, Markus Greiner, Vladan Vuletić, and Mikhail D. Lukin. A quantum processor based on coherent transport of entangled atom arrays. *Nature*, 604 (7906):451–456, 2022. ISSN 1476-4687. doi: 10.1038/s41586-022-04592-6. URL `http://dx.doi.org/10.1038/s41586-022-04592-6`.

[63] Simon J. Evered, Dolev Bluvstein, Marcin Kalinowski, Sepehr Ebadi, Tom Manovitz, Hengyun Zhou, Sophie H. Li, Alexandra A. Geim, Tout T. Wang, Nishad Maskara, Harry Levine, Giulia Semeghini, Markus Greiner, Vladan

Vuletić, and Mikhail D. Lukin. High-fidelity parallel entangling gates on a neutral-atom quantum computer. *Nature*, 622(7982):268–272, 2023. ISSN 1476-4687. doi: 10.1038/s41586-023-06481-y. URL `http://dx.doi.org/10.1038/s41586-023-06481-y`.

[64] Kevin Marshall, Raphael Pooser, George Siopsis, and Christian Weedbrook. Quantum simulation of quantum field theory using continuous variables. *Phys. Rev. A*, 92:063825, 2015. doi: 10.1103/PhysRevA.92.063825. URL `https://link.aps.org/doi/10.1103/PhysRevA.92.063825`.

[65] Adam M Kaufman, Brian J Lester, and Cindy A Regal. Cooling a single atom in an optical tweezer to its quantum ground state. *Phys. Rev. X*, 2(4): 041014, 2012.

[66] D. Barredo, V. Lienhard, P. Scholl, S. de Léséleuc, T. Boulier, A. Browaeys, and T. Lahaye. Three-dimensional trapping of individual Rydberg atoms in ponderomotive bottle beam traps. *Phys. Rev. Lett.*, 124:023201, 2020. doi: 10.1103/PhysRevLett.124.023201. URL `https://link.aps.org/doi/10.1103/PhysRevLett.124.023201`.

[67] J. Lampen, H. Nguyen, L. Li, P. R. Berman, and A. Kuzmich. Long-lived coherence between ground and Rydberg levels in a magic-wavelength lattice. *Phys. Rev. A*, 98:033411, 2018. doi: 10.1103/PhysRevA.98.033411. URL `https://link.aps.org/doi/10.1103/PhysRevA.98.033411`.

[68] Lukas Ahlheit, Chris Nill, Daniil Svirskiy, Jan de Haan, Simon Schroers, Wolfgang Alt, Nina Stiesdal, Igor Lesanovsky, and Sebastian Hofferberth. Magic running- and standing-wave optical traps for Rydberg atoms. *Phys. Rev. A*, 111:013115, 2025. doi: 10.1103/PhysRevA.111.013115. URL `https://link.aps.org/doi/10.1103/PhysRevA.111.013115`.

[69] C. Hölzl, A. Götzelmann, E. Pultinevicius, M. Wirth, and F. Meinert. Long-lived circular Rydberg qubits of alkaline-earth atoms in optical tweezers. *Phys. Rev. X*, 14:021024, 2024. doi: 10.1103/PhysRevX.14.021024. URL `https://link.aps.org/doi/10.1103/PhysRevX.14.021024`.

[70] Yevhen Miroshnychenko, Wolfgang Alt, Igor Dotsenko, Leonid Förster, Mkrtych Khudaverdyan, Dieter Meschede, Dominik Schrader, and Arno Rauschenbeutel. An atom-sorting machine. *Nature*, 442(7099):151, 2006. doi: 10.1038/442151a. URL `https://doi.org/10.1038/442151a`.

[71] Daniel Barredo, Vincent Lienhard, Sylvain de Léséleuc, Thierry Lahaye, and Antoine Browaeys. Synthetic three-dimensional atomic structures assembled atom by atom. *Nature*, 561(7721):79, 2018. ISSN 14764687. doi: 10.1038/s41586-018-0450-2. URL `http://dx.doi.org/10.1038/s41586-018-0450-2`.

[72] Weikun Tian, Wen Jun Wee, An Qu, Billy Jun Ming Lim, Prithvi Raj Datla, Vanessa Pei Wen Koh, and Huanqian Loh. Parallel assembly of arbitrary defect-free atom arrays with a multitweezer algorithm. *Phys. Rev. Appl.*, 19:034048, 2023. doi: 10.1103/PhysRevApplied.19.034048. URL `https://link.aps.org/doi/10.1103/PhysRevApplied.19.034048`.

[73] Alice Pagano, Daniel Jaschke, Werner Weiss, and Simone Montangero. Optimal control transport of neutral atoms in optical tweezers at finite temperature. *Phys. Rev. Res.*, 6:033282, 2024. doi: 10.1103/PhysRevResearch.6.033282. URL `https://link.aps.org/doi/10.1103/PhysRevResearch.6.033282`.

[74] Luheng Zhao, Michael Dao Kang Lee, Mohammad Mujahid Aliyu, and Huanqian Loh. Floquet-tailored Rydberg interactions. *Nature Communications*, 14(1):7128, 2023. doi: 10.1038/s41467-023-42899-8. URL `https://doi.org/10.1038/s41467-023-42899-8`.

[75] Haoquan Fan, Santosh Kumar, Jonathon Sedlacek, Harald Kübler, Shaya Karimkashi, and James P Shaffer. Atom based rf electric field sensing. *Journal of Physics B: Atomic, Molecular and Optical Physics*, 48 (20):202001, 2015. doi: 10.1088/0953-4075/48/20/202001. URL `https://dx.doi.org/10.1088/0953-4075/48/20/202001`.

[76] C S Adams, J D Pritchard, and J P Shaffer. Rydberg atom quantum technologies, 2020. ISSN 13616455.

[77] M. Martinez-Dorantes, W. Alt, J. Gallego, S. Ghosh, L. Ratschbacher, Y. Völzke, and D. Meschede. Fast nondestructive parallel readout of neutral atom registers in optical potentials. *Phys. Rev. Lett.*, 119:180503, 2017. doi: 10.1103/PhysRevLett.119.180503. URL `https://link.aps.org/doi/10.1103/PhysRevLett.119.180503`.

[78] Matthew N. H. Chow, Bethany J. Little, and Yuan-Yu Jau. High-fidelity low-loss state detection of alkali-metal atoms in optical tweezer traps. *Phys.*

Rev. A, 108:032407, 2023. doi: 10.1103/PhysRevA.108.032407. URL `https://link.aps.org/doi/10.1103/PhysRevA.108.032407`.

[79] Loïc Anderegg, Lawrence W. Cheuk, Yicheng Bao, Sean Burchesky, Wolfgang Ketterle, Kang-Kuen Ni, and John M. Doyle. An optical tweezer array of ultracold molecules. *Science*, 365(6458):1156–1158, 2019. doi: 10.1126/science.aax1265. URL `https://www.science.org/doi/abs/10.1126/science.aax1265`.

[80] Alexandre Cooper, Jacob P. Covey, Ivaylo S. Madjarov, Sergey G. Porsev, Marianna S. Safronova, and Manuel Endres. Alkaline-earth atoms in optical tweezers. *Phys. Rev. X*, 8:041055, Dec 2018. doi: 10.1103/PhysRevX.8.041055. URL `https://link.aps.org/doi/10.1103/PhysRevX.8.041055`.

[81] M. A. Norcia, A. W. Young, and A. M. Kaufman. Microscopic control and detection of ultracold strontium in optical-tweezer arrays. *Phys. Rev. X*, 8:041054, Dec 2018. doi: 10.1103/PhysRevX.8.041054. URL `https://link.aps.org/doi/10.1103/PhysRevX.8.041054`.

[82] D. Bluvstein, A. Omran, H. Levine, A. Keesling, G. Semeghini, S. Ebadi, T. T. Wang, A. A. Michailidis, N. Maskara, W. W. Ho, S. Choi, M. Serbyn, M. Greiner, V. Vuletić, and M. D. Lukin. Controlling quantum many-body dynamics in driven Rydberg atom arrays. *Science*, 371(6536):1355–1359, 2021. ISSN 1095-9203. doi: 10.1126/science.abg2530. URL `http://dx.doi.org/10.1126/science.abg2530`.

[83] Pascal Scholl, Michael Schuler, Hannah J. Williams, Alexander A. Eberharter, Daniel Barredo, Kai-Niklas Schymik, Vincent Lienhard, Louis-Paul Henry, Thomas C. Lang, Thierry Lahaye, Andreas M. Läuchli, and Antoine Browaeys. Quantum simulation of 2D antiferromagnets with hundreds of Rydberg atoms. *Nature*, 595(7866):233–238, 2021. doi: 10.1038/s41586-021-03585-1. URL `https://doi.org/10.1038/s41586-021-03585-1`.

[84] B. Nikolov, E. Diamond-Hitchcock, J. Bass, N. L. R. Spong, and J. D. Pritchard. Randomized benchmarking using nondestructive readout in a two-dimensional atom array. *Phys. Rev. Lett.*, 131:030602, 2023. doi: 10.1103/PhysRevLett.131.030602. URL `https://link.aps.org/doi/10.1103/PhysRevLett.131.030602`.

[85] Sepehr Ebadi, Tout T. Wang, Harry Levine, Alexander Keesling, Giulia Semeghini, Ahmed Omran, Dolev Bluvstein, Rhine Samajdar, Hannes Pichler, Wen Wei Ho, Soonwon Choi, Subir Sachdev, Markus Greiner, Vladan Vuletić, and Mikhail D. Lukin. Quantum phases of matter on a 256-atom programmable quantum simulator. *Nature*, 595(7866):227–232, 2021. ISSN 1476-4687. doi: 10.1038/s41586-021-03582-4. URL `https://doi.org/10.1038/s41586-021-03582-4`.

[86] L. Isenhower, E. Urban, X. L. Zhang, A. T. Gill, T. Henage, T. A. Johnson, T. G. Walker, and M. Saffman. Demonstration of a neutral atom controlled-not quantum gate. *Phys. Rev. Lett.*, 104:010503, 2010. doi: 10.1103/PhysRevLett.104.010503.

[87] K. M. Maller, M. T. Lichtman, T. Xia, Y. Sun, M. J. Piotrowicz, A. W. Carr, L. Isenhower, and M. Saffman. Rydberg-blockade controlled-not gate and entanglement in a two-dimensional array of neutral-atom qubits. *Phys. Rev. A*, 92:022336, 2015. doi: 10.1103/PhysRevA.92.022336.

[88] Y. Zeng, P. Xu, X. He, Y. Liu, M. Liu, J. Wang, D. J. Papoular, G. V. Shlyapnikov, and M. Zhan. Entangling two individual atoms of different isotopes via Rydberg blockade. *Phys. Rev. Lett.*, 119:160502, 2017. doi: 10.1103/PhysRevLett.119.160502.

[89] Harry Levine, Alexander Keesling, Giulia Semeghini, Ahmed Omran, Tout T. Wang, Sepehr Ebadi, Hannes Bernien, Markus Greiner, Vladan Vuletić, Hannes Pichler, and Mikhail D. Lukin. Parallel Implementation of High-Fidelity Multiqubit Gates with Neutral Atoms. *Phys. Rev. Lett.*, 123 (17):1, 2019. ISSN 10797114. doi: 10.1103/PhysRevLett.123.170503.

[90] T. M. Graham, M. Kwon, B. Grinkemeyer, Z. Marra, X. Jiang, M. T. Lichtman, Y. Sun, M. Ebert, and M. Saffman. Rydberg-mediated entanglement in a two-dimensional neutral atom qubit array. *Phys. Rev. Lett.*, 123:230501, 2019. doi: 10.1103/PhysRevLett.123.230501.

[91] Z. Fu, P. Xu, Y. Sun, Y. Liu, X. He, X. Li, M. Liu, R. Li, J. Wang, L. Liu, and M. Zhan. High-fidelity Rydberg quantum gate via a two-photon adiabatic passage. *Phys. Rev. Lett.*, 129:250501, 2022. doi: 10.1103/PhysRevLett.129.250501.

[92] T. M. Graham, Y. Song, J. Scott, C. Poole, L. Phuttitarn, K. Jooya, P. Eichler, X. Jiang, A. Marra, B. Grinkemeyer, M. Kwon, M. Ebert, J. Cherek, M. T. Lichtman, M. Gillette, J. Gilbert, D. Bowman, T. Ballance, C. Campbell, E. D. Dahl, O. Crawford, N. S. Blunt, B. Rogers, T. Noel, and M. Saffman. Multi-qubit entanglement and algorithms on a neutral-atom quantum computer. *Nature*, 604(7906):457–462, 2022. doi: 10.1038/s41586-022-04603-6. URL `https://doi.org/10.1038/s41586-022-04603-6`.

[93] Pascal Scholl, Adam L. Shaw, Richard Bing-Shiun Tsai, Ran Finkelstein, Joonhee Choi, and Manuel Endres. Erasure conversion in a high-fidelity Rydberg quantum simulator. *Nature*, 622(7982):273–278, 2023. doi: 10.1038/s41586-023-06516-4. URL `https://doi.org/10.1038/s41586-023-06516-4`.

[94] Iris Cong, Harry Levine, Alexander Keesling, Dolev Bluvstein, Sheng-Tao Wang, and Mikhail D. Lukin. Hardware-efficient, fault-tolerant quantum computation with Rydberg atoms. *Phys. Rev. X*, 12:021049, 2022. doi: 10.1103/PhysRevX.12.021049. URL `https://link.aps.org/doi/10.1103/PhysRevX.12.021049`.

[95] V. Negîrneac, H. Ali, N. Muthusubramanian, F. Battistel, R. Sagastizabal, M. S. Moreira, J. F. Marques, W. J. Vlothuizen, M. Beekman, C. Zachariadis, N. Haider, A. Bruno, and L. DiCarlo. High-fidelity controlled-z gate with maximal intermediate leakage operating at the speed limit in a superconducting quantum processor. *Phys. Rev. Lett.*, 126:220502, 2021. doi: 10.1103/PhysRevLett.126.220502. URL `https://link.aps.org/doi/10.1103/PhysRevLett.126.220502`.

[96] V. Borish, O. Marković, J. A. Hines, S. V. Rajagopal, and M. Schleier-Smith. Transverse-field Ising dynamics in a Rydberg-dressed atomic gas. *Phys. Rev. Lett.*, 124:063601, 2020. doi: 10.1103/PhysRevLett.124.063601. URL `https://link.aps.org/doi/10.1103/PhysRevLett.124.063601`.

[97] P. Scholl, H. J. Williams, G. Bornet, F. Wallner, D. Barredo, L. Henriet, A. Signoles, C. Hainaut, T. Franz, S. Geier, A. Tebben, A. Salzinger, G. Zürn, T. Lahaye, M. Weidemüller, and A. Browaeys. Microwave engineering of programmable XXZ Hamiltonians in arrays of Rydberg atoms.

PRX Quantum, 3:020303, 2022. doi: 10.1103/PRXQuantum.3.020303. URL `https://link.aps.org/doi/10.1103/PRXQuantum.3.020303`.

[98] Cheng Chen, Guillaume Bornet, Marcus Bintz, Gabriel Emperauger, Lucas Leclerc, Vincent S. Liu, Pascal Scholl, Daniel Barredo, Johannes Hauschild, Shubhayu Chatterjee, Michael Schuler, Andreas M. Läuchli, Michael P. Zaletel, Thierry Lahaye, Norman Y. Yao, and Antoine Browaeys. Continuous symmetry breaking in a two-dimensional rydberg array. *Nature*, 616(7958): 691–695, Apr 2023. ISSN 1476-4687. doi: 10.1038/s41586-023-05859-2. URL `https://doi.org/10.1038/s41586-023-05859-2`.

[99] Vincent Lienhard, Sylvain de Léséleuc, Daniel Barredo, Thierry Lahaye, Antoine Browaeys, Michael Schuler, Louis-Paul Henry, and Andreas M. Läuchli. Observing the space- and time-dependent growth of correlations in dynamically tuned synthetic Ising models with antiferromagnetic interactions. *Physical Review X*, 8(2), 2018. ISSN 2160-3308. doi: 10.1103/physrevx.8.021070. URL `http://dx.doi.org/10.1103/PhysRevX.8.021070`.

[100] Sylvain de Léséleuc, Vincent Lienhard, Pascal Scholl, Daniel Barredo, Sebastian Weber, Nicolai Lang, Hans Peter Büchler, Thierry Lahaye, and Antoine Browaeys. Observation of a symmetry-protected topological phase of interacting bosons with Rydberg atoms. *Science*, 365(6455):775–780, 2019. ISSN 1095-9203. doi: 10.1126/science.aav9105. URL `http://dx.doi.org/10.1126/science.aav9105`.

[101] Sebastian Weber, Christoph Tresp, Henri Menke, Alban Urvoy, Ofer Firstenberg, Hans Peter Büchler, and Sebastian Hofferberth. Calculation of Rydberg interaction potentials. *J. Phys. B*, 50(13), 2017. ISSN 13616455. doi: 10.1088/1361-6455/aa743a.

[102] G. Semeghini, H. Levine, A. Keesling, S. Ebadi, T. T. Wang, D. Bluvstein, R. Verresen, H. Pichler, M. Kalinowski, R. Samajdar, A. Omran, S. Sachdev, A. Vishwanath, M. Greiner, V. Vuletić, and M. D. Lukin. Probing topological spin liquids on a programmable quantum simulator. *Science*, 374(6572): 1242–1247, 2021. ISSN 1095-9203. doi: 10.1126/science.abi8794. URL `http://dx.doi.org/10.1126/science.abi8794`.

[103] Giuliano Giudici, Mikhail D. Lukin, and Hannes Pichler. Dynamical preparation of quantum spin liquids in Rydberg atom arrays. *Phys. Rev. Lett.*,

129:090401, 2022. doi: 10.1103/PhysRevLett.129.090401. URL `https://link.aps.org/doi/10.1103/PhysRevLett.129.090401`.

[104] Milan Kornjača, Rhine Samajdar, Tommaso Macrì, Nathan Gemelke, Sheng-Tao Wang, and Fangli Liu. Trimer quantum spin liquid in a honeycomb array of Rydberg atoms. *Communications Physics*, 6(1), 2023. ISSN 2399-3650. doi: 10.1038/s42005-023-01470-z. URL `http://dx.doi.org/10.1038/s42005-023-01470-z`.

[105] Tomohiro Hashizume, Gregory S. Bentsen, Sebastian Weber, and Andrew J. Daley. Deterministic fast scrambling with neutral atom arrays. *Physical Review Letters*, 126(20), 2021. ISSN 1079-7114. doi: 10.1103/physrevlett.126.200603. URL `http://dx.doi.org/10.1103/PhysRevLett.126.200603`.

[106] Xinhui Liang, Zongpei Yue, Yu-Xin Chao, Zhen-Xing Hua, Yige Lin, Meng Khoon Tey, and Li You. Observation of anomalous information scrambling in a Rydberg atom array, 2024. URL `https://arxiv.org/abs/2410.16174`.

[107] A. G. de Oliveira, E. Diamond-Hitchcock, D. M. Walker, M. T. Wells-Pestell, G. Pelegrí, C. J. Picken, G. P. A. Malcolm, A. J. Daley, J. Bass, and J. D. Pritchard. Demonstration of weighted-graph optimization on a Rydberg-atom array using local light shifts. *PRX Quantum*, 6:010301, 2025. doi: 10.1103/PRXQuantum.6.010301. URL `https://link.aps.org/doi/10.1103/PRXQuantum.6.010301`.

[108] Luca D'Alessio and Marcos Rigol. Dynamical preparation of Floquet-Chern insulators. *Nature Communications*, 6(1), 2015. ISSN 2041-1723. doi: 10.1038/ncomms9336. URL `http://dx.doi.org/10.1038/ncomms9336`.

[109] Tadashi Kadowaki and Hidetoshi Nishimori. Quantum annealing in the transverse Ising model. *Physical Review E*, 58(5):5355–5363, 1998. ISSN 1095-3787. doi: 10.1103/physreve.58.5355. URL `http://dx.doi.org/10.1103/PhysRevE.58.5355`.

[110] Hannes Pichler, Sheng-Tao Wang, Leo Zhou, Soonwon Choi, and Mikhail D. Lukin. Quantum optimization for maximum independent set using Rydberg atom arrays, 2018. URL `https://arxiv.org/abs/1808.10816`.

[111] A. W. Glaetzle, R. M. W. van Bijnen, P. Zoller, and W. Lechner. A coherent quantum annealer with Rydberg atoms. *Nature Communications*, 8(1), 2017.

ISSN 2041-1723. doi: 10.1038/ncomms15813. URL `http://dx.doi.org/10.1038/ncomms15813`.

[112] Conor Mc Keever and Michael Lubasch. Towards adiabatic quantum computing using compressed quantum circuits. *PRX Quantum*, 5:020362, 2024. doi: 10.1103/PRXQuantum.5.020362. URL `https://link.aps.org/doi/10.1103/PRXQuantum.5.020362`.

[113] Subir Sachdev, K. Sengupta, and S. M. Girvin. Mott insulators in strong electric fields. *Phys. Rev. B*, 66:075128, 2002. doi: 10.1103/PhysRevB.66.075128. URL `https://link.aps.org/doi/10.1103/PhysRevB.66.075128`.

[114] J Schachenmayer, I Lesanovsky, A Micheli, and A J Daley. Dynamical crystal creation with polar molecules or Rydberg atoms in optical lattices. *New Journal of Physics*, 12(10):103044, 2010. doi: 10.1088/1367-2630/12/10/103044. URL `https://dx.doi.org/10.1088/1367-2630/12/10/103044`.

[115] Rui Li, Jing Qian, and Weiping Zhang. Proposal for practical Rydberg quantum gates using a native two-photon excitation. *Quantum Science and Technology*, 8(3):035032, 2023. doi: 10.1088/2058-9565/ace0d5.

[116] Harry Levine, Alexander Keesling, Ahmed Omran, Hannes Bernien, Sylvain Schwartz, Alexander S. Zibrov, Manuel Endres, Markus Greiner, Vladan Vuletić, and Mikhail D. Lukin. High-fidelity control and entanglement of Rydberg-atom qubits. *Phys. Rev. Lett.*, 121:123603, 2018. doi: 10.1103/PhysRevLett.121.123603. URL `https://link.aps.org/doi/10.1103/PhysRevLett.121.123603`.

[117] Tomas Kozlej, Gerard Pelegri, Jonathan D. Pritchard, and Andrew J. Daley. Adiabatic state preparation and thermalization of simulated phase noise in a Rydberg spin Hamiltonian, 2025. URL `https://arxiv.org/abs/2505.04595`.

[118] Matthew L. Day, Pei Jiang Low, Brendan White, Rajibul Islam, and Crystal Senko. Limits on atomic qubit control from laser noise, 2022. ISSN 2056-6387. URL `https://doi.org/10.1038/s41534-022-00586-4`.

[119] X. Jiang, J. Scott, Mark Friesen, and M. Saffman. Sensitivity of quantum gate fidelity to laser phase and intensity noise. *Phys. Rev. A*, 107:042611, 2023. doi: 10.1103/PhysRevA.107.042611. URL `https://link.aps.org/doi/10.1103/PhysRevA.107.042611`.

[120] J. Timmer and M. König. On generating power law noise. *Astronomy & Astrophysics*, 300:707, 1995. URL `https://ui.adsabs.harvard.edu/abs/1995A&A...300..707T`.

[121] Donald P. Fahey and Michael W. Noel. Excitation of Rydberg states in rubidium with near infrared diode lasers. *Opt. Express*, 19(18):17002–17012, 2011. doi: 10.1364/OE.19.017002. URL `https://opg.optica.org/oe/abstract.cfm?URI=oe-19-18-17002`.

[122] Mohsen Darman and Kiazand Fasihi. A new compact circuit-level model of semiconductor lasers: investigation of relative intensity noise and frequency noise spectra. *Journal of Modern Optics*, 64(18):1839–1845, 2017. doi: 10.1080/09500340.2017.1321152. URL `https://doi.org/10.1080/09500340.2017.1321152`.

[123] Huadong Lu, Jing Su, Changde Xie, and Kunchi Peng. Experimental investigation about influences of longitudinal-mode structure of pumping source on a ti:sapphire laser. *Opt. Express*, 19(2):1344–1353, 2011. doi: 10.1364/OE.19.001344. URL `https://opg.optica.org/oe/abstract.cfm?URI=oe-19-2-1344`.

[124] Gianluca Galzerano, Paolo Laporta, L. Bonelli, Alessandra Toncelli, and Mauro Tonelli. Single-frequency diode-pumped yb:kyf(4) laser around 1030 nm. *Optics express*, 15 6:3257–64, 2007. URL `https://api.semanticscholar.org/CorpusID:42009928`.

[125] Rüdiger Paschotta. Noise in laser technology. *Optik & Photonik*, 4(2):48–50, 2009. doi: https://doi.org/10.1002/opph.201190028. URL `https://onlinelibrary.wiley.com/doi/abs/10.1002/opph.201190028`.

[126] A. D. Ludlow, X. Huang, M. Notcutt, T. Zanon-Willette, S. M. Foreman, M. M. Boyd, S. Blatt, and J. Ye. Compact, thermal-noise-limited optical cavity for diode laser stabilization at 1×10−15. *Opt. Lett.*, 32(6):641–643, 2007. doi: 10.1364/OL.32.000641. URL `https://opg.optica.org/ol/abstract.cfm?URI=ol-32-6-641`.

[127] V. Lovic, D.G. Marangon, M. Lucamarini, Z. Yuan, and A.J. Shields. Characterizing phase noise in a gain-switched laser diode for quantum random-number generation. *Phys. Rev. Appl.*, 16:054012, 2021. doi: 10.1103/

PhysRevApplied.16.054012. URL `https://link.aps.org/doi/10.1103/PhysRevApplied.16.054012`.

[128] Yu-Xin Chao, Zhen-Xing Hua, Xin-Hui Liang, Zong-Pei Yue, Chen Jia, Li You, and Meng Khoon Tey. Robust suppression of high-frequency laser phase noise by adaptive Pound-Drever-Hall feedforward. *Phys. Rev. Appl.*, 23:L011005, 2025. doi: 10.1103/PhysRevApplied.23.L011005. URL `https://link.aps.org/doi/10.1103/PhysRevApplied.23.L011005`.

[129] Zhen-Xing Hua, Yu-Xin Chao, Chen Jia, Xin-Hui Liang, Zong-Pei Yue, and Meng Khoon Tey. Feedforward cancellation of high-frequency phase noise in frequency-doubled lasers, 2025. URL `https://arxiv.org/abs/2501.07381`.

[130] A. Park, J. Trautmann, Neven Šantić, V. Klüsener, A. Heinz, Immanuel Bloch, and Sebastian Blatt. Cavity-enhanced optical lattices for scaling neutral atom quantum technologies to higher qubit numbers. *PRX Quantum*, 3, 2022. doi: 10.1103/PRXQuantum.3.030314.

[131] A. Heinz. *Ultracold strontium in state-dependent optical lattices*. Ph.d. thesis, Ludwig-Maximilians-Universität München, Department of Physics, 2020.

[132] André Heinz, Jan Trautmann, Neven Šantić, Annie Jihyun Park, Immanuel Bloch, and Sebastian Blatt. Crossed optical cavities with large mode diameters. *Opt. Lett.*, 46(2):250–253, 2021. doi: 10.1364/OL.414076. URL `https://opg.optica.org/ol/abstract.cfm?URI=ol-46-2-250`.

[133] Holger Müller, Sheng-Wey Chiow, Quan Long, and Steven Chu. Phase-locked, low-noise, frequency agile titanium: sapphire lasers for simultaneous atom interferometers. *Optics letters*, 31:202–4, 01 2006. doi: 10.1364/OL.31.000202.

[134] A Börzsönyi, R S Nagymihály, and K Osvay. Drift and noise of the carrier–envelope phase in a ti:sapphire amplifier. *Laser Physics Letters*, 13(1):015301, 2015. doi: 10.1088/1612-2011/13/1/015301. URL `https://dx.doi.org/10.1088/1612-2011/13/1/015301`.

[135] Dobrow. *A Gentle Introduction to Stochastic Calculus**, chapter 9, pages 372–399. John Wiley & Sons, Ltd, 2016. ISBN 9781118740712. doi: https://doi.org/10.1002/9781118740712.ch9. URL `https://onlinelibrary.wiley.com/doi/abs/10.1002/9781118740712.ch9`.

[136] Pece Trajanovski, Petar Jolakoski, Kiril Zelenkovski, Alexander Iomin, Ljupco Kocarev, and Trifce Sandev. Ornstein-Uhlenbeck process and generalizations: Particle dynamics under comb constraints and stochastic resetting. *Physical Review E*, 107(5), 2023. ISSN 2470-0053. doi: 10.1103/physreve.107.054129. URL `http://dx.doi.org/10.1103/PhysRevE.107.054129`.

[137] A. Khintchine. Korrelationstheorie der stationären stochastischen prozesse. *Mathematische Annalen*, 109:604–615, 1934. URL `http://eudml.org/doc/159698`.

[138] D. A. Dickey and. The analysis of time series: An introduction (4th ed.). *Technometrics*, 33(3):363–364, 1991. doi: 10.1080/00401706.1991.10484848. URL `https://doi.org/10.1080/00401706.1991.10484848`.

[139] N. Wiener and P. Masani. *Norbert Wiener - Collected Works: Mathematical Philosophy and Foundations - Potential Theory - Brownian Movement, Wiener Integrals, Ergodic and Chaos Theories, Turbulence and Statistical Mechanics*. Collected works. MIT Press, 1976. ISBN 9780262230704. URL `https://books.google.co.uk/books?id=UmGNzgEACAAJ`.

[140] Daniel T. Gillespie. Exact numerical simulation of the Ornstein-Uhlenbeck process and its integral. *Phys. Rev. E*, 54:2084–2091, 1996. doi: 10.1103/PhysRevE.54.2084. URL `https://link.aps.org/doi/10.1103/PhysRevE.54.2084`.

[141] E. Paladino, Y. M. Galperin, G. Falci, and B. L. Altshuler. frequency noise: Implications for solid-state quantum information. *Rev. Mod. Phys.*, 86:361–418, 2014. doi: 10.1103/RevModPhys.86.361. URL `https://link.aps.org/doi/10.1103/RevModPhys.86.361`.

[142] N. Jeremy Kasdin. Discrete simulation of colored noise and stochastic processes and $1/f\alpha$ power law noise generation. *Proceedings of the IEEE*, 83 (5):802–827, 1995. ISSN 0018-9219. doi: 10.1109/5.381848.

[143] George E. P. Box, Gwilym M. Jenkins, Gregory C. Reinsel, and Greta M. Ljung. *Time Series Analysis: Forecasting and Control*. John Wiley & Sons, Hoboken, New Jersey, 5th edition, 2015. ISBN 978-1-118-67502-1.

[144] Chang Xu. An easy algorithm to generate colored noise sequences. *The Astronomical Journal*, 157(3):127, 2019. doi: 10.3847/1538-3881/ab037c. URL `https://dx.doi.org/10.3847/1538-3881/ab037c`.

[145] F. Reihle. *Laser Frequency Standards*, chapter 9, pages 255–313. John Wiley & Sons, Ltd, 2003. ISBN 9783527605996. doi: https://doi.org/10.1002/3527605991.ch9. URL `https://onlinelibrary.wiley.com/doi/abs/10.1002/3527605991.ch9`.

[146] Fabian Schmid, Johannes Weitenberg, Theodor W. Hänsch, Thomas Udem, and Akira Ozawa. Simple phase noise measurement scheme for cavity-stabilized laser systems. *Optics Letters*, 44(11):2709, 2019. ISSN 1539-4794. doi: 10.1364/ol.44.002709. URL `http://dx.doi.org/10.1364/OL.44.002709`.

[147] Ian Affleck, Tom Kennedy, Elliott H. Lieb, and Hal Tasaki. Rigorous results on valence-bond ground states in antiferromagnets. *Phys. Rev. Lett.*, 59:799–802, Aug 1987. doi: 10.1103/PhysRevLett.59.799. URL `https://link.aps.org/doi/10.1103/PhysRevLett.59.799`.

[148] M. Fannes, B. Nachtergaele, and R. F. Werner. Finitely correlated states on quantum spin chains. *Communications in Mathematical Physics*, 144 (3):443–490, Mar 1992. ISSN 1432-0916. doi: 10.1007/BF02099178. URL `https://doi.org/10.1007/BF02099178`.

[149] Steven R. White. Density matrix formulation for quantum renormalization groups. *Phys. Rev. Lett.*, 69:2863–2866, 1992. doi: 10.1103/PhysRevLett.69.2863. URL `https://link.aps.org/doi/10.1103/PhysRevLett.69.2863`.

[150] Stellan Östlund and Stefan Rommer. Thermodynamic limit of density matrix renormalization. *Phys. Rev. Lett.*, 75:3537–3540, Nov 1995. doi: 10.1103/PhysRevLett.75.3537. URL `https://link.aps.org/doi/10.1103/PhysRevLett.75.3537`.

[151] U. Schollwöck. The density-matrix renormalization group. *Reviews of Modern Physics*, 77(1):259–315, 2005. ISSN 1539-0756. doi: 10.1103/revmodphys.77.259. URL `http://dx.doi.org/10.1103/RevModPhys.77.259`.

[152] Ulrich Schollwöck. The density-matrix renormalization group in the age of matrix product states. *Annals of Physics*, 326(1):96–192, 2011. ISSN 0003-4916. doi: 10.1016/j.aop.2010.09.012. URL `http://dx.doi.org/10.1016/j.aop.2010.09.012`.

[153] F. Verstraete, V. Murg, and J.I. Cirac. Matrix product states, projected entangled pair states, and variational renormalization group methods for quantum spin systems. *Advances in Physics*, 57(2):143–224, 2008. ISSN 1460-6976. doi: 10.1080/14789940801912366. URL `http://dx.doi.org/10.1080/14789940801912366`.

[154] Sebastian Paeckel, Thomas Köhler, Andreas Swoboda, Salvatore R. Manmana, Ulrich Schollwöck, and Claudius Hubig. Time-evolution methods for matrix-product states. *Annals of Physics*, 411:167998, 2019. ISSN 0003-4916. doi: 10.1016/j.aop.2019.167998. URL `http://dx.doi.org/10.1016/j.aop.2019.167998`.

[155] Thomas Barthel. One-dimensional quantum systems at finite temperatures can be simulated efficiently on classical computers, 2017. URL `https://arxiv.org/abs/1708.09349`.

[156] Stefan Wolff, Ameneh Sheikhan, and Corinna Kollath. Numerical evaluation of two-time correlation functions in open quantum systems with matrix product state methods: a comparison, 2020. URL `https://arxiv.org/abs/2004.01133`.

[157] Sambuddha Chattopadhyay, Hannes Pichler, Mikhail D. Lukin, and Wen Wei Ho. Quantum many-body scars from virtual entangled pairs. *Physical Review B*, 101(17), 2020. ISSN 2469-9969. doi: 10.1103/physrevb.101.174308. URL `http://dx.doi.org/10.1103/PhysRevB.101.174308`.

[158] Wen-Yuan Liu, Yi-Zhen Huang, Shou-Shu Gong, and Zheng-Cheng Gu. Accurate simulation for finite projected entangled pair states in two dimensions. *Physical Review B*, 103(23), 2021. ISSN 2469-9969. doi: 10.1103/physrevb.103.235155. URL `http://dx.doi.org/10.1103/PhysRevB.103.235155`.

[159] J. Eisert, M. Cramer, and M. B. Plenio. Colloquium: Area laws for the entanglement entropy. *Rev. Mod. Phys.*, 82:277–306, 2010. doi: 10.1103/RevModPhys.82.277. URL `https://link.aps.org/doi/10.1103/RevModPhys.82.277`.

[160] Saeed S. Jahromi and Román Orús. Thermal bosons in 3D optical lattices via tensor networks. *Scientific Reports*, 10(1), 2020. ISSN 2045-2322. doi: 10.1038/s41598-020-75548-x. URL `http://dx.doi.org/10.1038/s41598-020-75548-x`.

[161] Guifré Vidal. Efficient classical simulation of slightly entangled quantum computations. *Physical Review Letters*, 91(14), 2003. ISSN 1079-7114. doi: 10.1103/physrevlett.91.147902. URL `http://dx.doi.org/10.1103/PhysRevLett.91.147902`.

[162] Jutho Haegeman, J. Ignacio Cirac, Tobias J. Osborne, Iztok Pižorn, Henri Verschelde, and Frank Verstraete. Time-dependent variational principle for quantum lattices. *Phys. Rev. Lett.*, 107:070601, 2011. doi: 10.1103/PhysRevLett.107.070601. URL `https://link.aps.org/doi/10.1103/PhysRevLett.107.070601`.

[163] Benedikt Kloss, Yevgeny Bar Lev, and David Reichman. Time-dependent variational principle in matrix-product state manifolds: Pitfalls and potential. *Phys. Rev. B*, 97:024307, 2018. doi: 10.1103/PhysRevB.97.024307. URL `https://link.aps.org/doi/10.1103/PhysRevB.97.024307`.

[164] F. Verstraete and J. I. Cirac. Renormalization algorithms for quantum-many body systems in two and higher dimensions, 2004. URL `https://arxiv.org/abs/cond-mat/0407066`.

[165] Lloyd N. Trefethen and David Bau. *Numerical Linear, Algebra Twenty-fifth Anniversary Edition, part V: Eigenvalues.* Cambridge University Press, 2022. doi: 10.1137/1.9781611977165.ch5. URL `https://api.semanticscholar.org/CorpusID:259580462`.

[166] William H. Press, Saul A. Teukolsky, William T. Vetterling, and Brian P. Flannery. *Numerical Recipes 3rd Edition: The Art of Scientific Computing.* Cambridge University Press, USA, 3 edition, 2007. ISBN 0521880688.

[167] G. Vidal. Classical simulation of infinite-size quantum lattice systems in one spatial dimension. *Physical Review Letters*, 98(7), 2007. ISSN 1079-7114. doi: 10.1103/physrevlett.98.070201. URL `http://dx.doi.org/10.1103/PhysRevLett.98.070201`.

[168] J M Zhang and R X Dong. Exact diagonalization: the Bose-Hubbard model to illustrate exact diagonalization techniques in a pedagogical way. *European*

Journal of Physics, Volume 31, Number 3, 31(3):591, 2010. doi: 10.1088/0143-0807/31/3/016. URL `https://dx.doi.org/10.1088/0143-0807/31/3/016`.

[169] Kazutaka Takahashi and Adolfo del Campo. Krylov subspace methods for quantum dynamics with time-dependent generators. *Physical Review Letters*, 134(3), 2025. ISSN 1079-7114. doi: 10.1103/physrevlett.134.030401. URL `http://dx.doi.org/10.1103/PhysRevLett.134.030401`.

[170] Guifré Vidal. Efficient simulation of one-dimensional quantum many-body systems. *Physical Review Letters*, 93(4), 2004. ISSN 1079-7114. doi: 10.1103/physrevlett.93.040502. URL `http://dx.doi.org/10.1103/PhysRevLett.93.040502`.

[171] Masuo Suzuki. Generalized Trotter's formula and systematic approximants of exponential operators and inner derivations with applications to many-body problems. *Communications in Mathematical Physics*, 51(2):183–190, 1976. doi: 10.1007/BF01609348.

[172] Tilock Sadhukhan. Suzuki–Trotter decomposition: A step-by-step theoretical proof of the formulae. *C-DAC Banglore*, 01 2025.

[173] Steven R. White and Adrian E. Feiguin. Real-time evolution using the density matrix renormalization group. *Phys. Rev. Lett.*, 93:076401, 2004. doi: 10.1103/PhysRevLett.93.076401. URL `https://link.aps.org/doi/10.1103/PhysRevLett.93.076401`.

[174] A. J. Daley, C. Kollath, U. Schollwöck, and G. Vidal. Time-dependent density-matrix renormalization-group using adaptive effective Hilbert spaces. *Journal of Statistical Mechanics: Theory and Experiment*, 2004(04):P04005, 2004. ISSN 1742-5468. doi: 10.1088/1742-5468/2004/04/p04005. URL `http://dx.doi.org/10.1088/1742-5468/2004/04/P04005`.

[175] Jutho Haegeman, Christian Lubich, Ivan Oseledets, Bart Vandereycken, and Frank Verstraete. Unifying time evolution and optimization with matrix product states. *Physical Review B*, 94(16), 2016. ISSN 2469-9969. doi: 10.1103/physrevb.94.165116. URL `http://dx.doi.org/10.1103/PhysRevB.94.165116`.

[176] Xiao Yuan, Suguru Endo, Qi Zhao, Ying Li, and Simon C. Benjamin. Theory of variational quantum simulation. *Quantum*, 3:191, 2019. ISSN

2521-327X. doi: 10.22331/q-2019-10-07-191. URL `http://dx.doi.org/10.22331/q-2019-10-07-191`.

[177] M. Hochbruck and C. Lubich. On Krylov subspace approximations to the matrix exponential operator. *SIAM Journal on Numerical Analysis*, 34(5): 1911–1925, 1997. doi: 10.1137/S0036142995280572. URL `http://dx.doi.org/10.1137/S0036142995280572`.

[178] Joey Li, Giuliano Giudici, and Hannes Pichler. Variational manifolds for ground states and scarred dynamics of blockade-constrained spin models on two- and three-dimensional lattices. *Physical Review Research*, 6(2), 2024. ISSN 2643-1564. doi: 10.1103/physrevresearch.6.023146. URL `http://dx.doi.org/10.1103/PhysRevResearch.6.023146`.

[179] Christian Lubich, Ivan V. Oseledets, and Bart Vandereycken. Time integration of tensor trains. *SIAM Journal on Numerical Analysis*, 53(2): 917–941, 2015. ISSN 1095-7170. doi: 10.1137/140976546. URL `http://dx.doi.org/10.1137/140976546`.

[180] F. Verstraete, J. J. García-Ripoll, and J. I. Cirac. Matrix product density operators: Simulation of finite-temperature and dissipative systems. *Phys. Rev. Lett.*, 93:207204, 2004. doi: 10.1103/PhysRevLett.93.207204. URL `https://link.aps.org/doi/10.1103/PhysRevLett.93.207204`.

[181] David Jansen, Janez Bonča, and Fabian Heidrich-Meisner. Finite-temperature optical conductivity with density-matrix renormalization group methods for the holstein polaron and bipolaron with dispersive phonons. *Phys. Rev. B*, 106:155129, 2022. doi: 10.1103/PhysRevB.106.155129. URL `https://link.aps.org/doi/10.1103/PhysRevB.106.155129`.

[182] David Petrosyan, Felix Motzoi, Mark Saffman, and Klaus Mølmer. High-fidelity Rydberg quantum gate via a two-atom dark state. *Phys. Rev. A*, 96:042306, 2017. doi: 10.1103/PhysRevA.96.042306. URL `https://link.aps.org/doi/10.1103/PhysRevA.96.042306`.

[183] A. Tzortzakakis, David Petrosyan, Michael Fleischhauer, and K. Mølmer. Quasi-adiabatic preparation of ordered many-body states of Rydberg excitations of atoms in a lattice via steering the system through an extended gapless phase, 2021. URL `https://ui.adsabs.harvard.edu/abs/2022APS..DMPZ05002T`.

[184] Immanuel Bloch, Jean Dalibard, and Sylvain Nascimbène. Quantum simulations with ultracold quantum gases. *Nature Physics*, 8(4):267–276, 2012. doi: 10.1038/nphys2259. URL `https://hal.science/hal-03740937`.

[185] Ceren B. Dag, Hanzhen Ma, P. Myles Eugenio, Fang Fang, and Susanne F. Yelin. Emergent disorder and sub-ballistic dynamics in quantum simulations of the Ising model using Rydberg atom arrays, 2024. URL `https://arxiv.org/abs/2411.13643`.

[186] C. Ates, A. Eisfeld, and J. M. Rost. Motion of Rydberg atoms induced by resonant dipole–dipole interactions. *New Journal of Physics*, 10(4):045030, apr 2008. doi: 10.1088/1367-2630/10/4/045030. URL `https://doi.org/10.1088/1367-2630/10/4/045030`.

[187] Antoine Browaeys, Daniel Barredo, and Thierry Lahaye. Experimental investigations of dipole–dipole interactions between a few Rydberg atoms. *Journal of Physics B: Atomic, Molecular and Optical Physics*, 49(15):152001, 2016. doi: 10.1088/0953-4075/49/15/152001. URL `https://dx.doi.org/10.1088/0953-4075/49/15/152001`.

[188] Sylvain de Léséleuc, Daniel Barredo, Vincent Lienhard, Antoine Browaeys, and Thierry Lahaye. Optical control of the resonant dipole-dipole interaction between Rydberg atoms. *Phys. Rev. Lett.*, 119:053202, 2017. doi: 10.1103/PhysRevLett.119.053202. URL `https://link.aps.org/doi/10.1103/PhysRevLett.119.053202`.

[189] I. I. Beterov and M. Saffman. Rydberg blockade, förster resonances, and quantum state measurements with different atomic species. *Phys. Rev. A*, 92:042710, Oct 2015. doi: 10.1103/PhysRevA.92.042710. URL `https://link.aps.org/doi/10.1103/PhysRevA.92.042710`.

[190] Karen Wadenpfuhl and C. Stuart Adams. Unraveling the structures in the van der waals interactions of alkali-metal rydberg atoms. *Phys. Rev. A*, 111:062803, Jun 2025. doi: 10.1103/PhysRevA.111.062803. URL `https://link.aps.org/doi/10.1103/PhysRevA.111.062803`.

[191] Lukas Homeier, Simon Hollerith, Sebastian Geier, Neng-Chun Chiu, Antoine Browaeys, and Lode Pollet. Supersolidity in rydberg tweezer arrays. *Phys. Rev. A*, 111:L011305, Jan 2025. doi: 10.1103/PhysRevA.111.L011305. URL `https://link.aps.org/doi/10.1103/PhysRevA.111.L011305`.

[192] Claudio Cazorla and Jordi Boronat. Simulation and understanding of atomic and molecular quantum crystals. *Reviews of Modern Physics*, 89(3), 2017. ISSN 1539-0756. doi: 10.1103/revmodphys.89.035003. URL `http://dx.doi.org/10.1103/RevModPhys.89.035003`.

[193] Ieva Čepaitė, Anatoli Polkovnikov, Andrew J. Daley, and Callum W. Duncan. Counterdiabatic optimized local driving. *PRX Quantum*, 4(1), 2023. ISSN 2691-3399. doi: 10.1103/prxquantum.4.010312. URL `http://dx.doi.org/10.1103/PRXQuantum.4.010312`.

[194] Sven Jandura and Guido Pupillo. Time-optimal two- and three-qubit gates for Rydberg atoms. *Quantum*, 6:712, 2022. ISSN 2521-327X. doi: 10.22331/q-2022-05-13-712. URL `http://dx.doi.org/10.22331/q-2022-05-13-712`.

[195] Charles Fromonteil, Roberto Tricarico, Francesco Cesa, and Hannes Pichler. Hamilton-Jacobi-Bellman equations for Rydberg-blockade processes. *Physical Review Research*, 6(3), 2024. ISSN 2643-1564. doi: 10.1103/physrevresearch.6.033333. URL `http://dx.doi.org/10.1103/PhysRevResearch.6.033333`.

[196] Jae Dong Noh. Operator growth in the transverse-field Ising spin chain with integrability-breaking longitudinal field. *Physical Review E*, 104(3), 2021. ISSN 2470-0053. doi: 10.1103/physreve.104.034112. URL `http://dx.doi.org/10.1103/PhysRevE.104.034112`.

[197] Joshua M Deutsch. Eigenstate thermalization hypothesis. *Reports on Progress in Physics*, 81(8):082001, 2018. doi: 10.1088/1361-6633/aac9f1. URL `https://dx.doi.org/10.1088/1361-6633/aac9f1`.

[198] R.Jancel. Chapter i - the ergodic theory in classical statistical mechanics. In *Foundations of Classical and Quantum Statistical Mechanics*, volume 19 of *International Series in Natural Philosophy*, pages 3–40. Elsevier, 2013. doi: https://doi.org/10.1016/B978-0-08-012823-8.50007-9. URL `https://www.sciencedirect.com/science/article/pii/B9780080128238500079`.

[199] Giovanni Gallavotti. *Statistical Mechanics: A Short Treatise.* Springer, Berlin, 1999.

[200] Mark Srednicki. Chaos and quantum thermalization. *Physical Review E*, 50(2):888–901, 1994. ISSN 1095-3787. doi: 10.1103/physreve.50.888. URL `http://dx.doi.org/10.1103/PhysRevE.50.888`.

[201] K. Sengupta, Stephen Powell, and Subir Sachdev. Quench dynamics across quantum critical points. *Physical Review A*, 69(5), 2004. ISSN 1094-1622. doi: 10.1103/physreva.69.053616. URL `http://dx.doi.org/10.1103/PhysRevA.69.053616`.

[202] Mihai Horoi, Vladimir Zelevinsky, and B. Alex Brown. Chaos vs thermalization in the nuclear shell model. *Phys. Rev. Lett.*, 74:5194–5197, 1995. doi: 10.1103/PhysRevLett.74.5194. URL `https://link.aps.org/doi/10.1103/PhysRevLett.74.5194`.

[203] Hyosub Kim, YeJe Park, Kyungtae Kim, H.-S. Sim, and Jaewook Ahn. Detailed balance of thermalization dynamics in Rydberg-atom quantum simulators. *Physical Review Letters*, 120(18), 2018. ISSN 1079-7114. doi: 10.1103/physrevlett.120.180502. URL `http://dx.doi.org/10.1103/PhysRevLett.120.180502`.

[204] Ehsan Khatami, Guido Pupillo, Mark Srednicki, and Marcos Rigol. Fluctuation-dissipation theorem in an isolated system of quantum dipolar bosons after a quench. *Physical Review Letters*, 111(5), 2013. ISSN 1079-7114. doi: 10.1103/physrevlett.111.050403. URL `http://dx.doi.org/10.1103/PhysRevLett.111.050403`.

[205] Luheng Zhao, Prithvi Raj Datla, Weikun Tian, Mohammad Mujahid Aliyu, and Huanqian Loh. Observation of quantum thermalization restricted to Hilbert space fragments and F_{2k} scars. *Phys. Rev. X*, 15:011035, 2025. doi: 10.1103/PhysRevX.15.011035. URL `https://link.aps.org/doi/10.1103/PhysRevX.15.011035`.

[206] Marcos Rigol, Vanja Dunjko, Vladimir Yurovsky, and Maxim Olshanii. Relaxation in a completely integrable many-body quantum system: Anab initiostudy of the dynamics of the highly excited states of 1d lattice hard-core bosons. *Physical Review Letters*, 98(5), 2007. ISSN 1079-7114. doi: 10.1103/physrevlett.98.050405. URL `http://dx.doi.org/10.1103/PhysRevLett.98.050405`.

[207] Toshiya Kinoshita, Trevor Wenger, and David S. Weiss. A quantum newton's cradle. *Nature*, 440:900–903, 2006. URL `https://api.semanticscholar.org/CorpusID:20114248`.

[208] S. R. Manmana, S. Wessel, R. M. Noack, and A. Muramatsu. Strongly correlated fermions after a quantum quench. *Phys. Rev. Lett.*, 98:210405, 2007. doi: 10.1103/PhysRevLett.98.210405. URL `https://link.aps.org/doi/10.1103/PhysRevLett.98.210405`.

[209] Amy C. Cassidy, Charles W. Clark, and Marcos Rigol. Generalized thermalization in an integrable lattice system. *Physical Review Letters*, 106 (14), 2011. ISSN 1079-7114. doi: 10.1103/physrevlett.106.140405. URL `http://dx.doi.org/10.1103/PhysRevLett.106.140405`.

[210] Marcus Kollar, F. Alexander Wolf, and Martin Eckstein. Generalized gibbs ensemble prediction of prethermalization plateaus and their relation to nonthermal steady states in integrable systems. *Physical Review B*, 84(5), 2011. ISSN 1550-235X. doi: 10.1103/physrevb.84.054304. URL `http://dx.doi.org/10.1103/PhysRevB.84.054304`.

[211] T Lahaye, C Menotti, L Santos, M Lewenstein, and T Pfau. The physics of dipolar bosonic quantum gases. *Reports on Progress in Physics*, 72(12): 126401, 2009. doi: 10.1088/0034-4885/72/12/126401. URL `https://dx.doi.org/10.1088/0034-4885/72/12/126401`.

[212] Yi Zhou, Kazushi Kanoda, and Tai-Kai Ng. Quantum spin liquid states. *Rev. Mod. Phys.*, 89:025003, 2017. doi: 10.1103/RevModPhys.89.025003. URL `https://link.aps.org/doi/10.1103/RevModPhys.89.025003`.

[213] J.G. Martínez-Herrera, O.A. Rodríguez-López, and M.A. Solís. Critical temperature of one-dimensional Ising model with long-range interaction revisited. *Physica A: Statistical Mechanics and its Applications*, 596: 127136, 2022. ISSN 0378-4371. doi: https://doi.org/10.1016/j.physa.2022.127136. URL `https://www.sciencedirect.com/science/article/pii/S0378437122001534`.

[214] J. M. Deutsch. Quantum statistical mechanics in a closed system. *Phys. Rev. A*, 43:2046–2049, 1991. doi: 10.1103/PhysRevA.43.2046. URL `https://link.aps.org/doi/10.1103/PhysRevA.43.2046`.

[215] Marcos Rigol, Vanja Dunjko, and Maxim Olshanii. Thermalization and its mechanism for generic isolated quantum systems. *Nature*, 452(7189): 854–858, 2008. ISSN 1476-4687. doi: 10.1038/nature06838. URL `http://dx.doi.org/10.1038/nature06838`.

[216] Fabien Alet and Nicolas Laflorencie. Many-body localization: An introduction and selected topics. *Comptes Rendus. Physique*, 19(6):498–525, 2018. ISSN 1878-1535. doi: 10.1016/j.crhy.2018.03.003. URL `http://dx.doi.org/10.1016/j.crhy.2018.03.003`.

[217] Scott D. Geraedts, Rahul Nandkishore, and Nicolas Regnault. Many-body localization and thermalization: Insights from the entanglement spectrum. *Phys. Rev. B*, 93:174202, 2016.

[218] Marcos Rigol. Breakdown of thermalization in finite one-dimensional systems. *Physical Review Letters*, 103(10), 2009. ISSN 1079-7114. doi: 10.1103/physrevlett.103.100403. URL `http://dx.doi.org/10.1103/PhysRevLett.103.100403`.

[219] Chi Zhang, Fabian Pokorny, Weibin Li, Gerard Higgins, Andreas Pöschl, Igor Lesanovsky, and Markus Hennrich. Submicrosecond entangling gate between trapped ions via Rydberg interaction. *Nature*, 580(7803):345–349, 2020. ISSN 1476-4687. doi: 10.1038/s41586-020-2152-9. URL `http://dx.doi.org/10.1038/s41586-020-2152-9`.

[220] A. G. de Oliveira, E. Diamond-Hitchcock, D. M. Walker, M. T. Wells-Pestell, G. Pelegrí, C. J. Picken, G. P. A. Malcolm, A. J. Daley, J. Bass, and J. D. Pritchard. Demonstration of weighted-graph optimization on a Rydberg-atom array using local light shifts. *PRX Quantum*, 6(1), 2025. ISSN 2691-3399. doi: 10.1103/prxquantum.6.010301. URL `http://dx.doi.org/10.1103/PRXQuantum.6.010301`.